Bachelor's thesis

NTNU
Norwegian University of Science and Technology
Faculty of Engineering
Department of Mechanical and Industrial Engineering

Max Sandberg Samset

Optimization and Experimental Validation of Variable-Angle Tow Composites for Enhanced Structural Performance

Bachelor's thesis in Mechanical Engineering
Supervisor: Anna Olsen
January 2024

NTNU
Norwegian University of
Science and Technology

Max Sandberg Samset

Optimization and Experimental Validation of Variable-Angle Tow Composites for Enhanced Structural Performance

Bachelor's thesis in Mechanical Engineering
Supervisor: Anna Olsen
January 2024

Norwegian University of Science and Technology
Faculty of Engineering
Department of Mechanical and Industrial Engineering

NTNU
Norwegian University of
Science and Technology

NTNU

REPORT BACHELOR THESIS

Title

Optimization and Experimental Validation of Variable-Angle Tow Composites for Enhanced Structural Performance

Numerisk of Eksperimentell Testing av Kompositttstrukturer med Kurvilineære Fiberbaner for Økt Strukturell Ytelse

Project number

MTP-K-2023-18

Author(s)

Max Sandberg Samset

Company (external)

Supervisor NTNU

Anna Olsen

Report is OPEN/CLOSED

OPEN

Date

12.01.2024

A design study is conducted in which the relative structural performance of fiber-steered and conventional composite laminates is quantified both numerically and experimentally. The aim of the investigation is to evaluate the potential of fiber-steering in reducing the weight of composite aircraft structures.

En designstudie gjennomføres der den strukturelle ytelsen til kompositttlaminater med kurvilineært- og lineært fiberformat kvantifiseres både numerisk og eksperimentellt. Målet med undersøkelsen er å vurdere potensialet til "fiber-steering" i å redusere vekten av kompositttstrukturer i flybransjen.

Stikkord: Fiberkompositter, Optimalisering, FEA, AFP, CFRP	Keywords: Fiber composites, Optimization, FEA, AFP, CFRP

ABSTRACT

In the continual need to improve efficiency within the aviation industry, composite materials currently play a pivotal role in reducing aircraft structural weight. This thesis investigates the benefit of a promising new class of composites, where fibers are steered in curvilinear paths to enhance structural efficiency. A design study is conducted in which performance is quantified both numerically and experimentally for a panel representing a lower wing skin section near a circular cutout. Quasi-isotropic, variable stiffness, and variable-angle tow laminates are compared.

The stiffness-optimal design for each design case was obtained through finite element-based numerical optimization, representative of state-of-the-art methods in the literature. This combined composite topology optimization with an approach for obtaining optimal fiber paths, while considering the design constraints related to composite wing design and manufacturing. The structures were manufactured from a carbon/epoxy prepreg material and tested in pure tension. The stiffness, failure loads, and failure modes of the panels were compared.

Numerical results reveal a notable improvement of 11% in specific stiffness and 27% in specific strength when utilizing curvilinear compared to linear fiber formats. Experimental results show good correspondence with predictions for stiffness but highlight larger discrepancies in strength. Based on an analysis of these results, potential improvements to the structural analysis and the optimization problem formulation are identified.

This design study signifies the potential of tow-steered composites in the context of composite wing design. Meanwhile, it sheds light on limitations within contemporary design optimization approaches, prompting further exploration and refinement in the pursuit of variable-angle tow structures for aeronautical applications.

SAMMENDRAG

I målet om å forbedre energieffektivitet innen luftfartindustrien spiller kompositt-materialer en sentral rolle i å redusere strukturell vekt. Oppgaven undersøker fordelen av en fremvoksende type kompositttstuktur, der fiber «styres» i kurvilineære baner for å effektivisere materialbruk. En designstudie gjennomføres der strukturell ytelse kvantifiseres både numerisk og eksperimentellt, for et panel som representerer nedre vingeoverflate i nærheten av et sirkulært adkomsthull. Tre ulike laminattyper sammenlignes: ett med krumlinjede fiber, ett med lineære fiber, og ett med uniform kvasi-isotrop fiberfordeling.

Det optimale designet for hvert tilfelle bestemmes ved bruk av elementbasert strukturell optimalisering, representativt for «state-of-the-art» innen fagfeltet. Topologioptimalisering kombineres med en metode for å beregne optimale fiberbaner, samtidig som at designbegrensningene knyttet til vingestrukturer hensyntas. Designene produseres deretter av et karbon/epoksy prepreg-materiale, og karakteriseres gjennom strekktesting. Stivhet, bruddlast, bruddform, og vekt sammenlignes.

De numeriske resultatene viser en betydelig forbedring på 11% i spesifikk stivhet of 27% i spesifikk styrke for kurvilinært sammenlignet med lineært fiberformat. Eksperimentelle resultater viser godt samsvar men hensyn på stivhet, men fremhever større avvik for styrke. I analysen av disse resultatene identifiseres potensielle forbedringer i den strukturelle analysen og i formuleringen av optimaliseringsproblemet.

Denne undersøkelsen viser tydelig potensiale for kurvilineært fiberformat innen vingekonstruksjoner. Samtidig belyses begrensninger av nåværende tilnærminger for strukturell optimalisering, og bidrar dermed med et utgangspunkt for videreutvikling i målet om å dra nytte av denne fordelen i fremtidige flystrukturer.

PREFACE

During my studies, design optimization captured my interest as a fascinating paradigm within mechanical engineering. As the recent proliferation of artificial intelligence has demonstrated on a broader scale, computation has the potential to far surpass human capabilities in problem-solving; in this case, in the development of lighter, more efficient, and more sustainable products. This thesis was inspired by the desire to explore this paradigm in depth and to understand its significance from a larger perspective.

I want to thank my employers at UBIQ Aerospace and the Department of Mechanical and Industrial Engineering at NTNU for providing the facilities that have enabled this work. I also want to thank Anna Olsen for supervising the project. Finally, I want to express my gratitude to my colleagues at UBIQ for their support, and to everyone at the institute who has found the time to answer my questions throughout this project.

Trondheim, 11.01.2024

Max Sandberg Samset

CONTENTS

LIST OF FIGURES

LIST OF TABLES

ABBREVIATIONS

AFP	Automated Fiber Placement
BC	Boundary Condition
CAD	Computer-Aided Design
CLT	Classical Lamination Theory
CFRP	Carbon Fiber Reinforced Polymers
DIC	Digital Image Correlation
DOF	Degree of Freedom
DV	Design Variable
ESL	Equivalent Single Layer
FE	Finite Element
FEA	Finite Element Analysis
FEM	Finite Element Method
FSDT	First-Order Shear Deformation Theory
LSF	Level Set Function
MCL	Minimum Cut Length
NURBS	Non-Uniform Rational Basis Spline
OOA	Out-of-Autoclave
VS	Variable Stiffness
UD	Unidirectional
VAT	Variable Angle Tow
QI	Quasi-Isotropic

CHAPTER

ONE

INTRODUCTION

1.1 Motivation

The design of optimal lightweight structures is a fundamental research topic in design engineering, and is a very active area within the aeronautics and aerospace industries. In particular, it has become paramount in improving the sustainability and energy efficiency of the commercial aviation industry, where weight is pivotal for the fuel consumption of an aircraft.

This development is driven by a combination of factors, including the increasing cost of fossil fuels, a broader commitment to sustainability, and environmental regulations aimed at reducing the aviation industry's emissions, which currently comprise 2% of the global total [1]. One of the most significant regulations was introduced by the International Civil Aviation Organization (ICAO), the global authority for commercial aviation, setting the goal of net zero for international flights by 2050. To achieve this scenario, technological and operational improvements must account for an average annual fuel burn reduction of 2% [2], a substantial increase over the historical average of 1.3% [3]. In response to these factors, aircraft manufacturers are actively exploring new design techniques for the lightweight structures of their next-generation aircraft.

In this regard, one of the most significant technological breakthroughs has been the adoption of composite materials in aircraft primary structures. Composites now comprise more than 50% of the total weight in prevalent commercial aircraft, such as the Airbus A350 and the Boeing 787 Dreamliner [4]. This transition can be attributed to several compelling advantages compared with metallic materials, such as high stiffness and strength relative to weight, as well as excellent corrosion and fatigue resistance [5]. Another considerable advantage is that stiffness and strength inherently depend on the local fiber direction. Engineers can customize the orientation of reinforcing fibers to align with anticipated load paths, enabling the tailoring of material properties to respond optimally to the local loading conditions. This targeted reinforcement allows for structural efficiencies that would otherwise be unattainable using isotropic materials.

However, engineers have yet to take full advantage of these anisotropic properties. Currently, modern aircraft structures are manufactured from an integer number of uniaxial plies, oriented at a limited set of fiber angles (Fig. 1.1.1). Composites are often used as a so-called "black metal," orienting fibers in an equal

Figure 1.1.1: Manufacturing of a composite fuselage section (Airbus A350) with fibers being placed on the mandrel in linear paths [7].

proportion of directions to produce a laminate with quasi-isotropic (QI) properties. Performance can be improved by optimizing the topology (i.e., local stacking sequence) of the plies, thereby tailoring the thickness and directional properties of the laminate. These structures are typically referred to as variable stiffness (VS) composites [6]. Even so, the degree to which the fibers can be aligned with the local loading direction is limited, given that most engineering structures exhibit load paths that change direction continuously throughout. Thus, while this set of restrictions eases the process of manufacturing and design, they simultaneously limit the attainable performance.

Given these drawbacks of contemporary design approaches, variable-angle tow (VAT) laminates have garnered growing attention as a promising new class of composite structures. In VAT laminates, the fiber orientation varies continuously over the structural domain within each ply (Fig. 1.1.2). This way, the point-wise directional properties of the laminate can be tailored to an even greater extent. The practical realization of such a structure is facilitated by advances in automated fiber placement (AFP) technology, enabling the automatic placement of fiber tows in precise curvilinear paths [8]. This process is known as composite tow steering.

Figure 1.1.2: Tow-steered wing structure manufactured by researchers at Aurora Flight Sciences [9].

Despite presenting great potential, VAT composites have yet to be used in a ma-

jor airframe structural component. Firstly, this is due to the limited amount of work quantifying the benefits of the technology relative to conventional structural design techniques, making it challenging to justify their adoption. Secondly, the methods for their design, analysis, and certification are currently less well defined and understood than for more conventional composites, due to the increase in design freedom and associated complexity [9]. These two challenges are closely linked, as studying the benefit of the technology relies on design optimization to quantify the maximum attainable performance for a given application. Consequently, demand has emerged for studies exploring the optimal design of VAT structures and applying these methods to solve practical design problems.

1.2 Prior Work

The research field studying the design of VAT structures has witnessed rapid growth over the past twenty years, with the number of publications increasing tenfold within this time period. Extensive reviews of these works are provided by Sobhani Aragh et al. [10] and Lozano et al. [11].

1.2.1 Current State of Research

The field of research consists of three main areas: analysis, optimization, and manufacturing. The majority of studies have focused on structural analysis and optimization, with several techniques for design having been developed. Optimization techniques are typically studied by applying them to components with basic geometries that are subjected to single load conditions. When dealing with complex structures, researchers often simplify the geometry to enable analysis and design using academic software tools [11].

A fundamental challenge is that the design and manufacturing of composite structures are highly interdependent. A number of papers are dedicated to characterizing the constraints associated with the manufacture of VAT structures, which represent crucial limiting factors for design. Several authors have noted that an accurate analysis of the potential of tow-steering greatly depends on the integration of these factors into the optimization framework [10]. To date, this integration remains an area of ongoing research. Approximately half of the studies on optimization consider some of the manufacturing constraints imposed by the AFP process [11]. The study of manufacturing parameters (e.g., cycle time, part quality, and cost) remains independent of structural optimization.

1.2.2 The Notched Plate Structure Problem

A recurring design problem in the literature is the optimization of plate structures with cutouts. In aerospace engineering, cutouts are a standard design element found on almost all structures. These vary in size and are essential for various purposes, including loading and unloading passengers or cargo, providing access for maintenance and inspection, or as windows and vents. The structural discontinuities introduced by these features result in the redistribution of stresses (Fig. 1.2.1), remarkably deteriorating both strength and stiffness, and thus neces-

sitating substantial additional reinforcement. Effectively mitigating these losses in structural performance may therefore lead to significant savings in weight.

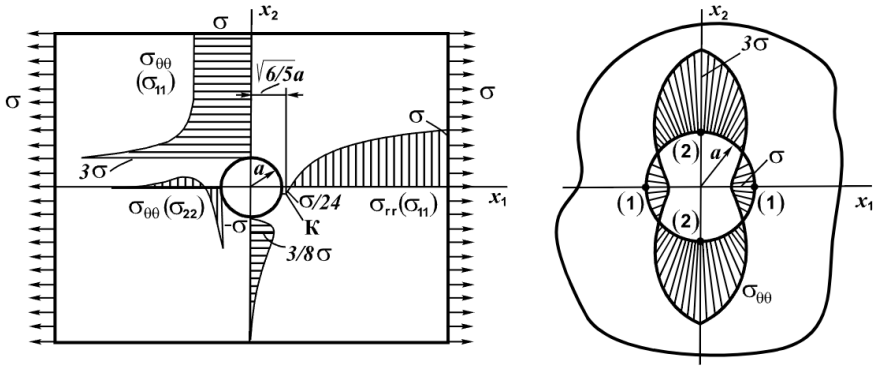

Figure 1.2.1: Stress concentrations resulting from a circular cutout in an isotropic plate under tension [12].

Hyer and Charette [13] were the first to investigate the steering of fibers around a circular cutout, proposing to align the fibers with the direction of principal stress. This study demonstrated that considerable improvements in performance were possible using this fiber format. Hyer and Lee [14] later introduced design optimization as a technique for determining the optimal fiber orientations. Nagendra et al. [15] used a similar design approach while integrating some of the manufacturing constraints, and demonstrated comparable increases in performance.

Building on these early studies, several combinations of objectives and boundary conditions have since been investigated. One topic has been the improvement of buckling load under compressive forces [16]. The ability of tow-steering mitigate stress concentrations has been another area of interest [17–20]. Others have investigated the elastic response under tensile loads [21, 22], optimizing for maximal stiffness.

1.2.3 Research Methodologies

Most papers studying the performance of VAT laminates are focused on purely theoretical analysis. Papers validating the theoretical results through design, manufacturing, and testing are scarce, accounting for less than 25% of the published papers [11].

Of these studies, many report notable discrepancies between theoretical and experimental results. Jegley et al. [23] conducted compression and shear tests on tow-steered panels with central holes. Simulation was used to predict buckling loads, with results that were significantly lower than experimental findings. Khani et al. [24] experimentally studied the stiffness and strength of flat panels with cutouts for conventional and VAT laminates under pure tension. The results confirmed the performance advantage of the VAT laminate, but showed considerable differences compared to the simulated behavior. In a similar study, Matsuzaki et al. [25] experimentally studied the tensile strength of VAT panels with cutouts under pure tension, and discovered a correlation between simulation discrepancy and average fiber curvature. Thus, closing this gap between simulation and real-life behavior remains an essential obstacle in determining the actual performance of VAT structures.

1.3 Scope

The aim of this thesis is defined as follows:

Verify the performance benefit of VAT for aerostructures with cutouts by experimentally validating the predictions of prevalent numerical approaches in the literature.

To accomplish this, a design study is conducted in which structural performance is quantified both numerically and experimentally. Three design cases are compared: VAT, VS, and QI (Table 1.3.1). To derive a realistic set of boundary conditions and constraints, the design study is based on a lower wing skin panel near a large access hole (Fig. 1.3.2). Modern transport-category aircraft wings use a semi-monocoque construction, where the outer skin is integral to the load-carrying structure. The loading conditions are dominated by bending forces caused by aerodynamic lift, which translate into tensile forces in the lower skin. For this panel, maximizing axial stiffness is one of the major design objectives [9]. These conditions are represented by considering the stiffness-optimal design of a two-dimensional plate with a circular cutout under pure tension (Fig. 1.3.1). Performance is evaluated on the grounds of stiffness and strength relative to mass.

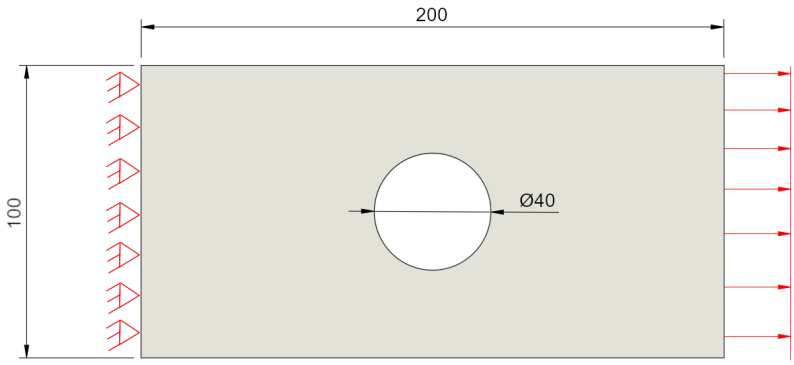

Figure 1.3.1: Plate geometry and boundary conditions.

Design case	Description
VAT	Laminate produced using tow-steering technology. Fiber orientation and layup configuration may vary throughout the structure.
VS	This represents the maximum attainable performance for a conventional composite structure. Fiber directions are linear, while the layup configuration may vary freely throughout the structure.
QI	Laminate with uniform thickness over the entire structure and an even distribution of fiber angles. Since this configuration represents the most common type used in practical applications [26], it is used as a datum.

Table 1.3.1: Summary of the design optimization cases.

Figure 1.3.2: Composite lower wing skin panel (Airbus A350) with access holes distributed along the spanwise direction [27].

To ensure the relevance of the results, an important delimitation is that the numerical solution should reflect the methods commonly used in the literature. Consequently, the focus is on developing an approach based on this literature, rather than on finding new ways to solve the optimization problem.

1.4 Objectives

The objectives of this thesis are defined as:

1. Define a realistic set of design constraints relating to composite wing design and manufacturing.
2. Establish state-of-the-art within the analysis and optimization of tow-steered composite structures.
3. Implement an optimization procedure capable of determining the optimal structural layout for each design case.
4. Manufacture and experimentally characterize the performance of the optimal designs.
5. Evaluate the design methodology and performance predictions using the experimental results.

1.5 Thesis Outline

The path followed to achieve the above objectives is reflected in the layout of this thesis.

Chapter 2 defines the design problem to be solved. This involves outlining the structural characteristics of the materials under study, how they can be modeled for the purposes of this thesis, and how they are incorporated into a composite wing manufacturing process. This also takes into account design standards that exist within the aviation industry.

Chapter 3 provides the necessary resources for solving the design problem defined previously. This review encompasses the mathematical parameterization of the structures, the integration of constraints into the formulation, and the techniques for solving of the optimization problem.

Chapter 4 presents the numerical solution of the design study. Informed by the findings of the preceding chapters, an optimization problem is formulated, and the methods for its solution are implemented. The outcome of this chapter is an optimal layup configuration and the predicted performance for each design case.

Chapter 5 describes the methodology used in validating the numerical results. This involves an approach for manufacturing, testing, and data acquisition. The outcome of these tests is subsequently presented and contextualized with the numerical results.

Chapter 6 discusses the implications of the results with regard to the aim of the thesis. The focus of this discussion is on identifying the root causes of errors in the numerical predictions, and using the available body of knowledge to propose improvements to the analysis.

Chapter 7 presents significant conclusions drawn from the results, and outlines possible avenues for future work.

CHAPTER

TWO

DESIGN PROBLEM DEFINITION

2.1 Structural Analysis

The model for structural analysis plays a central role in the design study solution, as the optimization process is built solely on the responses produced by this model. Aligning this with the relevant literature is a crucial first step in fulfilling the thesis objective.

2.1.1 Constituents of Advanced Composites

A composite material is defined as a combination of two or more constituent materials, typically resulting in better properties than when the individual components are used separately. The term "advanced composites" is often used when referring to the high-performance fiber-reinforced materials used in aerospace structures.

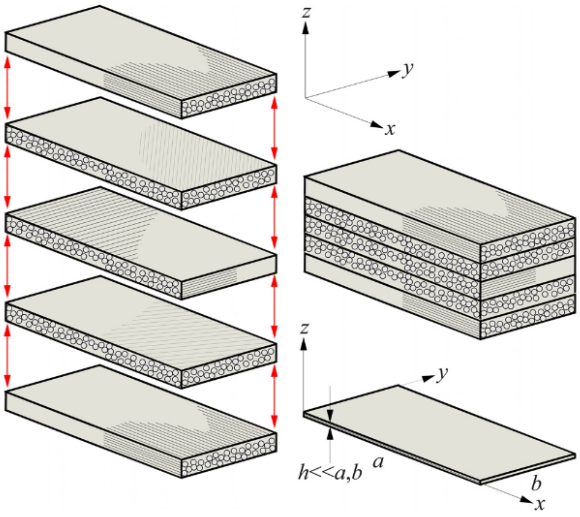

Figure 2.1.1: Composite laminate with unidirectional fibers [28].

The constituents of a fiber-reinforced composite are a fiber and a matrix. Fibers are arranged in plies (or laminae), which form the basic building block of a composite structure. The primary structures of commercial aircraft predominantly

consist of unidirectional (UD) plies, meaning the fibers within the ply are all aligned in a single direction. These are used to construct a laminate, which is a bonded stack of plies with various orientations (Fig. 2.1.1).

The fibers are the principal load-carrying agent of the structure. Typical fibers used for aerospace applications include carbon, boron, E- or S-glass, quartz, silicon, and aramid [29]. Carbon fibers are the most prevalent type due to their extremely high specific strength and stiffness, as well as being elastic to failure at normal temperatures, creep resistant, chemically inert, and having excellent damping and fatigue characteristics [30].

The primary function of the matrix is to provide a means of transmitting load between the fibers. Polymeric matrices are classified as either thermosets or thermoplastics. *Thermoset* resins are low-viscosity monomers that are converted into cross-linked polymers during a curing stage. This polymerization is driven by heat, generated either by the exothermic cross-linking reaction itself or by an external supply. In contrast, *thermoplastics* are not chemically cross-linked and instead use temperature to control the material's aggregation state. Thermoset resins remain the more prevalent matrix material for aerospace composites. Of these, epoxies are the predominant resins for low and moderate-temperature applications, owing to their excellent mechanical properties [31].

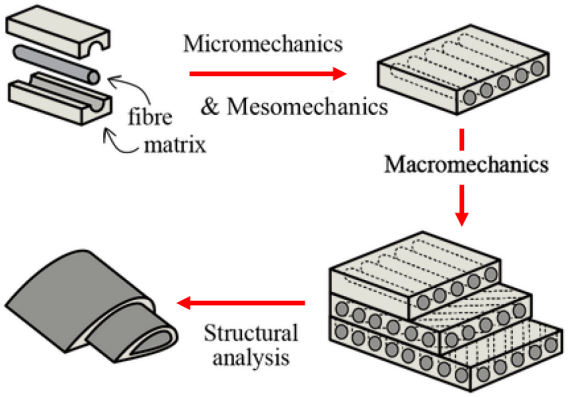

Figure 2.1.2: Levels of analysis for composite structures.

Due to their heterogeneous nature, the mechanical analysis of composite materials spans multiple size scales (Fig. 2.1.2). The detailed analysis of mechanical behavior at the fiber level is the subject of *micromechanics*. In this thesis, the structure is modeled using *macromechanics*, where the material is presumed to be homogeneous, with the effects of the constituents only detected as averaged macroscopic properties of the material. This is the predominant form of analysis where a "global" structural response is the aim of the computations [32].

2.1.2 Ply Elastic Behavior

Fiber-reinforced composite materials are normally treated as linear elastic, since the linear elastic fibers provide the majority of the stiffness. A UD composite ply exhibits three mutually orthogonal planes of symmetry, that define three principal axes of material properties: the material coordinate system 1, 2, and 3 axes. These define the fiber direction, transverse matrix direction, and the through-thickness

direction of the ply, respectively. The fiber orientation is defined relative to the global x-axis using the right-hand rule, and is denoted by θ (Fig. 2.1.3).

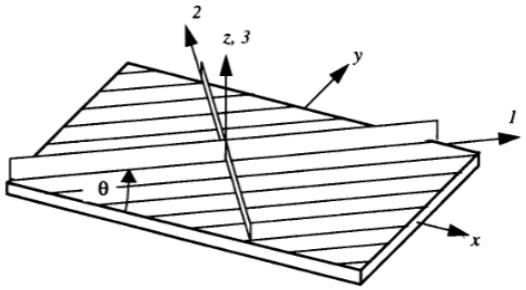

Figure 2.1.3: Planes of material symmetry for a unidirectional lamina [29].

Because of this symmetry, the ply is said to define an *orthotropic* material. The generalized Hooke's law for orthotropic materials is written as [32]:

$$\boldsymbol{\sigma}_i = \mathbf{Q}_{ij}\boldsymbol{\varepsilon}_j \qquad\qquad i, j \;=\; 1,\;\; \ldots\;,\; 6$$

Where $\boldsymbol{\sigma}_i$ are the stress components, $\boldsymbol{Q}_{ij}$ is the stiffness matrix, and $\boldsymbol{\varepsilon}_j$ are the strain components. For laminates where the thickness is small compared to the other characteristic dimensions of the structure, the plies are often assumed to be in a state of plane stress. This assumption is generally valid, as carrying in-plane stresses is the fundamental capability of the ply. In such a case, the out-of-plane stress components σ_z, τ_{yz}, and τ_{xz} are negligible compared to the in-plane stresses:

$$\sigma_z \approx \tau_{yz} \approx \tau_{xz} \approx 0 \tag{2.1}$$

For orthotropic materials, imposing a state of plane stress simplifies the stress-strain relations from a 6-by-6 to the 3-by-3 system:

$$\begin{bmatrix}\sigma_1\\ \sigma_2\\ \tau_{12}\end{bmatrix} = \begin{bmatrix}Q_{11} & Q_{12} & 0\\ Q_{12} & Q_{22} & 0\\ 0 & 0 & Q_{66}\end{bmatrix}\begin{bmatrix}\varepsilon_1\\ \varepsilon_2\\ \gamma_{12}\end{bmatrix} \tag{2.2}$$

Where $\mathbf{Q}$ is referred to as the *reduced material stiffness matrix*, describing the elastic behavior along the two principal axes of the ply. This matrix can be characterized with only four independent material constants: E_1, E_2, v_{12}, and G_{12}.

When the principal axes of orthotropy are oriented at an angle θ relative to the global coordinate system (an *off-axis* ply), the stiffness properties are obtained from $\mathbf{Q}$ through standard tensor transformations. For this case, the material stiffness matrix will have the characteristics of an anisotropic material, as a coupling is introduced between extension and shear deformation. Off-axis orthotropic plies are referred to as *generally orthotropic*.

2.1.3 Laminate Elastic Behavior

A laminate consisting of n plies (Fig. 2.1.4) is denoted by its stacking sequence (or layup), where θ_k is the angle of the k^{th} ply starting from the tooling-side of the laminate:

$$[\theta_1/\theta_2/\theta_3.../\theta_k]$$

The behavior of multilayered structures can be modeled using either three-dimensional elasticity theory or equivalent-single-layer (ESL) theories [33]. ESL theories simplify the analysis by representing the laminate only in terms of its mid-surface plane, and are derived from 3D elasticity theory by making assumptions about the kinematics of deformation or stress state within the structure. According to the literature survey by Sobhani Aragh et al. [10], the overwhelming majority of papers on the design of tow-steered structures have utilized ESL theories, most commonly classical lamination theory (CLT) and first-order shear deformation theory (FSDT).

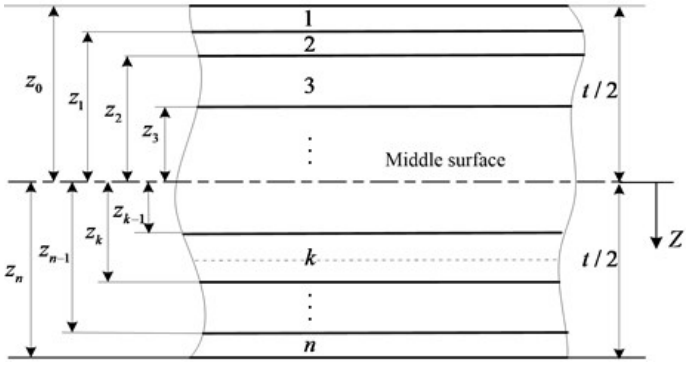

Figure 2.1.4: Geometry of an n-layered laminate [29].

For this work, the analysis will be based on CLT, the prevalence of which can be attributed mainly to its simplicity. The assumptions made by CLT result in a relatively low number of variables and equations, which reduces computational effort compared to other laminate theories. Consequently, CLT has a limited area of validity, which however coincides well with the characteristics of the structures under study. This can be observed from its assumptions, which are summarized as follows [32]:

1. Plies are homogeneous and in a state of plane stress.
2. Adjacent plies are perfectly bonded with an infinitesimally thin bond line.
3. The laminate deforms according to the Kirchoff-Love plate theory, where the plate is inextensible in the transverse direction ($\varepsilon_{zz} = 0$) and transverse shear deformations are negligible ($\gamma_{xz} = 0$, $\gamma_{yz} = 0$).

These simplifications are generally valid when considering *thin* plates and shells. In this case, the laminate in-plane forces $\mathbf{N}$ and out-of-plane moments $\mathbf{M}$ can be related to the deformation $\boldsymbol{\varepsilon}^0$ and the curvature $\boldsymbol{\kappa}$ of the laminate by the following expression:

$$\begin{Bmatrix} N_x \\ N_y \\ N_{xy} \end{Bmatrix} = \begin{bmatrix} A_{11} & A_{12} & A_{16} \\ & A_{22} & A_{26} \\ sym. & & A_{66} \end{bmatrix} \begin{Bmatrix} \varepsilon_x^0 \\ \varepsilon_y^0 \\ \gamma_{xy}^0 \end{Bmatrix} + \begin{bmatrix} B_{11} & B_{12} & B_{16} \\ & B_{22} & B_{26} \\ sym. & & B_{66} \end{bmatrix} \begin{Bmatrix} \kappa_x \\ \kappa_y \\ 2\kappa_{xy} \end{Bmatrix} \tag{2.3}$$

$$\begin{Bmatrix} M_x \\ M_y \\ M_{xy} \end{Bmatrix} = \begin{bmatrix} B_{11} & B_{12} & B_{16} \\ & B_{22} & B_{26} \\ sym. & & B_{66} \end{bmatrix} \begin{Bmatrix} \varepsilon_x^0 \\ \varepsilon_y^0 \\ \gamma_{xy}^0 \end{Bmatrix} + \begin{bmatrix} D_{11} & D_{12} & D_{16} \\ & D_{22} & D_{26} \\ sym. & & D_{66} \end{bmatrix} \begin{Bmatrix} \kappa_x \\ \kappa_y \\ 2\kappa_{xy} \end{Bmatrix} \tag{2.4}$$

Where **A**, **B**, and **D** are called the extensional, coupling, and bending stiffness matrices, respectively. The components of these three stiffness matrices are calculated from the material stiffness matrix **Q**, laminate midplane distance z, and thickness t of the individual plies.

As can be observed from Eq. 2.3, lamination leads to a material with a total of 18 elastic constants. Due to the anisotropic behavior of a laminate (caused by the non-aligned orthotropy of the plies), effects such as bending-extension coupling, bend-twist coupling, and shear-extension coupling arise when stresses are applied. Laminates are often categorized based on the presence of such effects. One of the design cases in this thesis is the *quasi-isotropic* (QI) laminate, which produces an isotropic **A** matrix. This means that stiffness is independent of material orientation and that extension and shear are uncoupled, making the elastic behavior analogous to that of a metal. Other notable laminate types include *balanced* and *symmetric* laminates, for which the A_{16} and A_{26} coefficients (extension-shear coupling) and coupling matrix **B** (bending-extension coupling) become zero, respectively.

2.1.4 Failure Prediction

As a result of their composition, composite materials display a multitude of failure mechanisms, with an accordingly large number of failure criteria existing for their prediction. These can be categorized based on several factors, such as whether they are based on strength or fracture mechanics theories, predict general failure or are targeted toward a specific failure mode, and focus on in-plane or interlaminar failure [34]. The analysis in this thesis will be limited to the prediction of in-plane failure using ply-based failure criteria, which is the predominant method used in the relevant literature.

Similarly as for stiffness, the strength of unidirectional plies at the macroscopic level is direction-dependent. The strength in the fiber direction is generally high, whereas the matrix material controls the strength in the perpendicular direction, meaning it is usually an order of magnitude lower. Five basic failure modes exist for a ply under plane stress: longitudinal tensile or compressive, transverse tensile or compressive, or shear (Fig. 2.1.5). As established previously, elastic behavior often demonstrates coupling between shear- and normal deformations. The stresses induced by these coupling effects often make it challenging to predict whether the failure is controlled by fiber strength, matrix normal strength, matrix shearing strength, or a combination of these [33].

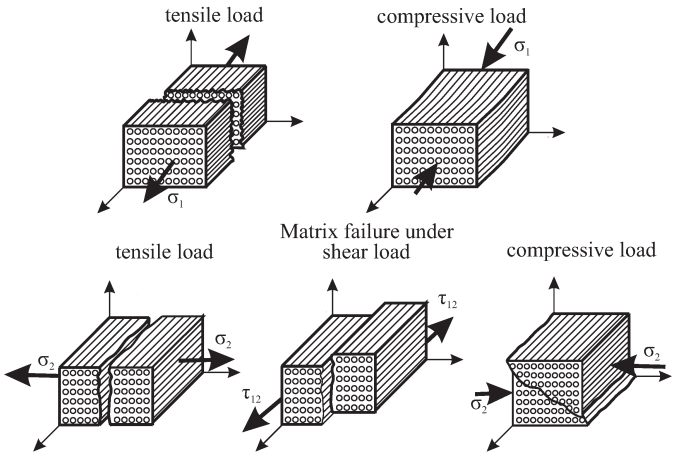

Figure 2.1.5: In-plane failure modes of a composite ply [35].

For *ply-based* failure criteria, the laminate strain tensor (such as the one obtained in Eq. 2.3) is used to derive the strain at each ply, which in turn is used to predict whether the ply is failed. Ply-based criteria are usually grouped into two classes: *limit criteria* and *interactive criteria* [29].

The simplest of these, *limit criteria*, predict failure when the ultimate strength along or transverse the fiber directions is exceeded, either as maximum stress or maximum strain criteria. On the other hand, *interactive criteria* account for the interactions between different stress components in failure mechanisms, which have been observed to affect strength for fiber-reinforced materials [36]. Several interactive failure criteria of varying complexity have been developed, their validity often being confined to a well-defined set of stress states. This is the approach predominantly taken in comparable studies on tow-steered laminates with cutouts, where strength analysis has been performed primarily using Tsai-Wu [21, 24, 37], Tsai-Hill [38, 39], or other ply-based interactive criteria [25].

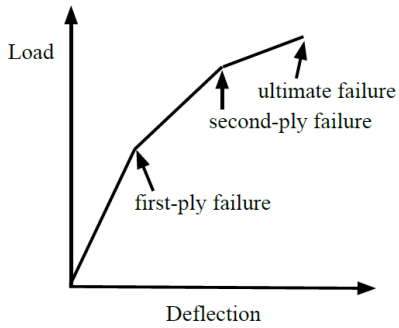

Figure 2.1.6: Progressive failure of a composite laminate.

Another challenge in evaluating in-plane failure is caused by through-the-thickness variation of stress within the laminate. Since the stiffness and strength in a particular direction may differ between layers, it's possible for some of the plies to reach their limiting strength before others. In some cases, failure of any layer is unacceptable since it degrades the structural properties of the laminate. This is referred to as the *first-ply failure* criterion. Alternatively, the laminate may be considered to be unfailed as long as it sustains the applied load without unstable

failure of the remaining plies. In such a case, as the load is increased, failure progresses from one layer to the next, leading to what is called *progressive failure* (Fig. 2.1.6).

2.1.5 Finite Element Analysis

The *finite element method* (FEM) is a numerical method for solving partial differential equations, which serves as the foundation for most structural analysis within engineering. This method is based on the principle of discretizing complex systems as a collection of simple elements (Fig. 2.1.7). The practical application of FEM is known as *finite element analysis* (FEA).

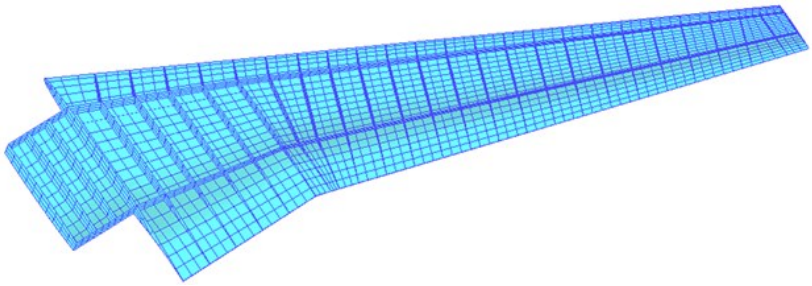

Figure 2.1.7: Wing structure subdivided into finite elements [40].

Due to the geometry and boundary conditions of the notched plate, studies in the relevant literature tend to employ *linear static* analysis [10]. *Linear* implies proportionality between load and deformation, which is generally valid as long as deformations are sufficiently small. *Static* refers to the application of static loads without considering time-dependent effects. The final formulation is the linear system:

$$\mathbf{Ka} = \mathbf{f}$$

Where $\mathbf{K} = \{K_{ij}\}$ is the *stiffness matrix* and $\mathbf{f} = \{f_j\}$ is the *load vector*. The solution of this linear system leads to the discrete solution $\mathbf{a} = \{a_i\}$ for all $i = 1 \ldots n$ nodes inside the modeling domain. For static analysis, $\mathbf{a}$ represents the displacement of the nodes (called the *nodal displacement vector*), from which reaction forces, strains, and stresses are calculated.

There are several ways to model a laminated composite structure using finite elements. In practice, it is common to employ plate or shell elements, which are two-dimensional elements representing the laminate mid-surface plane, typically used in conjunction with ESL theories [41]. Provided that the assumptions for the constitutive equations are satisfied (e.g., Kirchoff or Mindlin plate theories), these elements can be employed to accurately model three-dimensional laminated structures. Alternatively, two-dimensional solid elements are widely used if only the in-plane behavior is to be studied. Both of these element types can occur as quadrilaterals or triangles.

FEA is, by nature, an approximate solution, as it does not satisfy equilibrium over any smaller volume than an element. The displacement assumption used in forming the stiffness matrix means that FE structures will generally be overstiff, an inaccuracy that is mitigated either by using a finer mesh or higher-order

elements [41]. The *order* of an element refers to the complexity of the shape functions used to approximate the behavior of the underlying physical system: higher-order elements use more complex shape functions, often cubic or higher-order polynomials, as opposed to the linear or quadratic functions of lower order elements. Furthermore, a finer mesh results in a more accurate description of stress variation within a structure, particularly when large stress gradients or concentrations are present. Both these parameters provide an improved structural response at the cost of reduced computational efficiency. Thus, the successful use of FEA depends on constructing a model that delivers an acceptable accuracy without becoming prohibitively expensive to solve.

2.2 Boundary Conditions for Design

To define the constraints that apply to the design problem, it is necessary to consider how it relates to the larger picture of aircraft design and manufacturing. Two key aspects are identified as having a significant impact on design:

- The first set of constraints are the restrictions imposed by manufacturing. These result from the AFP process, which is the current key technology for manufacturing tow-steered composites.
- The second set of constraints are the regulations and standards within the industry regarding laminate design. This includes safety and airworthiness standards imposed by aviation authorities such as the FAA and EASA, and design guidelines formulated by aircraft manufacturers.

2.2.1 Automated Fiber Placement

AFP is an automated method for the layup of continuous-fiber composite tows (Fig. 2.2.1). AFP was developed at several places independently, including Boeing, Cincinnati Machine, and Hercules in the early 1980s [42]. Currently, AFP is crucial to the manufacturing of complex aerospace components such as wings, fuselages, and empennages, as well as engine components such as fan blades and nacelles [29].

In AFP, narrow composite tapes, called tows, are fed into a tow-placement head which laminates them onto the tooling surface. Here, the tows are combined into a single continuous band of material, known as a tow course. The tow-placement head moves in seven degrees of freedom: three positional axes, three rotational axes, and one axis to rotate the tooling. A typical tow-placement head can accommodate 32 tows, each with a usual width of 3.2 mm. This results in a tow course up to 10.24 cm wide [43]. The machine can cut or restart individual tows within a course during placement, allowing the width of the course to be increased or decreased as needed. The rate at which each tow is dispensed is controlled individually, allowing each of them to independently conform to the part's surface. This differential payout system is what enables the steering of tow courses in curvilinear paths.

Figure 2.2.1: Layup of a composite wing skin using AFP (Airbus A350) [44].

The prevalence of this process in modern aerospace manufacturing is attributed to its precision, efficiency, and versatility. The complete automation of the layup process accelerates production and reduces labor costs, especially for large parts [42]. Furthermore, AFP enables the production of complex geometries and layups that would be impossible to fabricate using other automated methods, such as filament winding or automated tape laying (ATL).

2.2.2 Prepreg Manufacturing Process

Prepreg, short for "pre-impregnated" composite material, is the most prevalent product form for producing high-quality laminates within the aerospace industry [31].

Thermoset prepregs usually consist of a single layer of fibers embedded in a precisely controlled amount of B-staged (partially cured) resin (Fig. 2.2.2). Because an optimal ratio of resin to fibers is maintained, this results in superior strength-to-weight ratios and lower variability compared to other processes. The resin at this stage is semi-solid with negligible strength and stiffness, allowing the ply to conform to the shape of the tool. The tackiness of the B-staged resin also allows it to adhere to itself and tooling details during the layup operation.

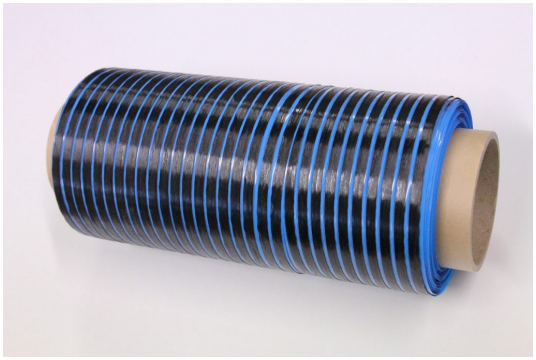

Figure 2.2.2: Unidirectional carbon-epoxy prepreg tow used for AFP [45].

At the curing stage, the plies are compressed under elevated temperature to form the final laminate. For this step, autoclave curing is the most widely used method

[31]. The laminate is sealed within an airtight vacuum bag and placed into the autoclave, which simultaneously heats and pressurizes the part according to a specified curing cycle. When subjected to elevated temperatures, the resin viscosity drops dramatically, allowing it to flow and distribute itself within the laminate. The high positive pressure (typically 3-12 bar) consolidates the reinforcement layers and removes trapped air or volatiles while minimizing outgassing from the resin as it polymerizes. The result is a laminate with minimal porosity (<1%) and highly consistent and uniform mechanical properties.

Figure 2.2.3: Autoclave cure of a composite wing skin (Airbus 777X) [46].

An alternative processing technique that major aerospace manufacturers have increasingly adopted since the mid-2000s is out-of-autoclave (OOA) prepreg. These can be cured at atmospheric pressures and significantly lower temperatures, reducing energy consumption, cycle times, and production costs. Although excessive porosity has historically been an inhibitor for wider adoption, modern materials allow for porosity levels similar to that of autoclave-processed parts [29]. For practical reasons, the experimental testing in this thesis will be conducted using an OOA prepreg material.

2.2.3 Tow Path Constraints

Due to the mechanics of placing tow courses using AFP, several constraints arise that limit the permitted distribution of fiber angles within a ply.

When the tows are steered, the fibers experience compressive and tensile forces, due to the inner radius of the tow being smaller than the outer radius. The minimum turning radius $r_{\min}$ represents the smallest radius of fiber curvature that can be placed without risk of defects, such as the tow twisting over itself or wrinkling (Fig. 2.2.4). Smaller values of $r_{\min}$ are possible by placing courses with narrower tows, with the drawback of increased manufacturing time and cost. Values of 508 - 635 mm have been documented for AFP machines [10].

Furthermore, gaps and overlaps may appear whenever adjacent courses are not laid in parallel. These areas may cause inaccuracies in the predicted properties of the design, if not accounted for in the structural analysis. Furthermore, gaps form resin-rich pockets within the laminate, which become initiation points for

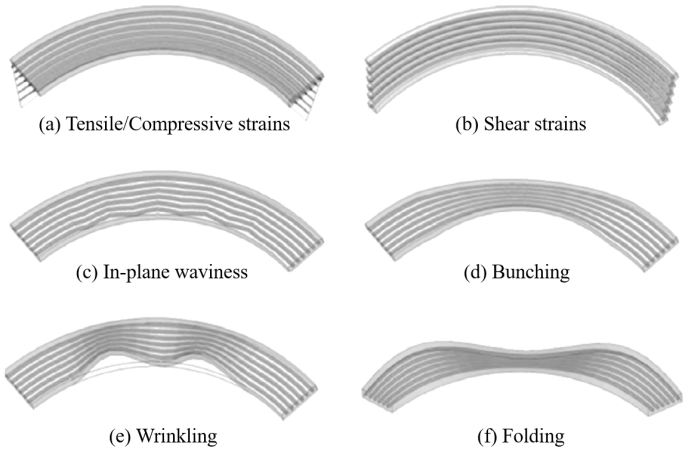

Figure 2.2.4: Tow deformation mechanisms for differential length absorption due to steering [47].

damage and failure. Several studies have investigated the detrimental impact of overlap/gap presence for various structural characteristics, including buckling resistance, stiffness, strength, and fundamental frequency [4].

The final set of limitations relates to the cutting mechanism of the machine. The minimum cut length (MCL) represents the distance between the cutting mechanism and the compaction roller, and constitutes the shortest length over which a tow can be placed. An MCL of 80 mm was defined by Lozano et al. [48]. Moreover, since tows are cut perpendicular to the layup direction, jagged or saw-tooth edges will appear at course boundaries if they do not align with this direction.

2.2.4 Ply Construction Methods

To construct a ply that covers the whole mandrel surface, the AFP machine must lay a number of adjacent courses. The literature proposes three methods for this arrangement when designing with steered tow courses: the tow-overlap, parallel, and tow-drop methods.

- **Tow-overlap** - In the most straightforward technique, initially proposed by Tatting and Gürdal [49], intersecting tows are permitted to overlap each other, resulting in local buildups in thickness. A challenge is that the accuracy of the structural analysis depends on the prediction of these thickness variations, as will be discussed in Section 3.2.3.

- **Parallel courses** - According to the parallel method, each fiber course is laid parallel to the adjacent courses. This method results in a ply of uniform thickness, free of gaps or overlaps between tows. However, the constraint of parallel courses severely restricts design freedom, resulting in a performance deficit compared to other methods.

- **Tow-drop** - By utilizing the cut-restart capability of the AFP machine, the tow-drop method prevents overlaps by cutting the tows when they intersect (Fig. 2.2.5). A so-called coverage parameter assesses where tows should be cut and reinitiated, thereby constructing a constant thickness ply containing small wedge-shape gaps or overlaps [50].

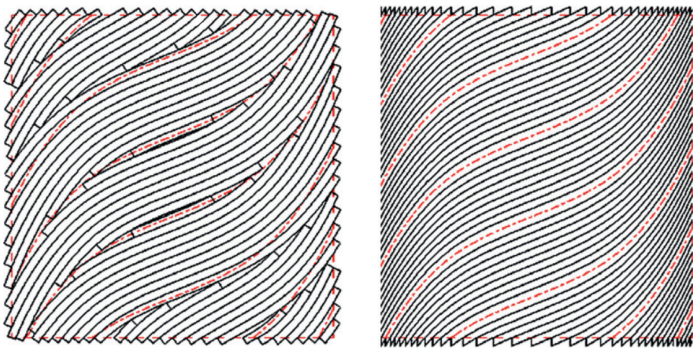

Figure 2.2.5: Tow-steered ply using (a) tow-drop technique (b) overlap technique [42].

2.2.5 Certification Requirements

By regulation, aircraft structures are required to undergo physical testing in order to verify their behavior [51]. This follows a *building block approach*, comprising tests at the coupon, element, detail, sub-component, and component levels (Fig. 2.2.6). The main purpose of employing the building-block approach is to meet all technical and regulatory requirements while requiring as few of the expensive full-scale articles as possible for testing [52].

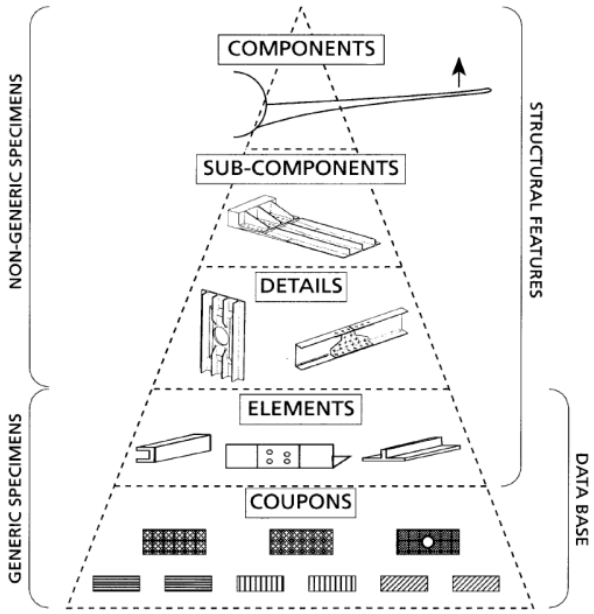

Figure 2.2.6: Building block approach to aircraft structure certification [52].

At the lowest level, small specimens are used to characterize basic unnotched static material properties. For a VS laminate, such coupon tests must be used to quantify the strength allowables for each laminate family in the structure. These

are calculated using statistical methods and are referred to as *A-basis* and *B-basis* allowables, denoting the first and tenth percentile of measurements, respectively [53].

Because of this empirical process, certification is typically associated with tremendous investments by aircraft manufacturers. Thus, limiting the number of laminate families comprising the structure becomes an important design consideration. This is a major reason why, to date, laminate design within commercial transport aircraft is restricted to the four principal orientations 0°, ±45°, and 90°. It also represents an important limiting factor for the design of tow-steered structures. Theoretically, every ply within such a structure could have its own independent set of two courses, which, however, would lead to an unworkable number of laminate coupons to be tested. For this reason, it is common to instead define a single "main" orientation, and to align all plies at fixed angles relative to this [54]. In this manner, a VAT structure is obtained that maintains a "core laminate" whose relative orientations are constant at any given point, resulting in a finite number of laminate families.

2.2.6 Laminate Design Rules

Laminate design rules are guidelines developed by aircraft manufacturers to mitigate the risk of premature component failure. This primarily regards complex failure modes that may occur due to the inherent weaknesses of laminated composites, such as their low interlaminar tensile strength. Many of these guidelines have evolved as lessons learned from prototype development programs and industrial experience, rather than being derived from first principles [55]. An in-depth review of design rules for UD carbon fiber aircraft structures is provided by Bailie et al. [56]. Their implications for laminate design are summarized as follows:

- Laminates should be designed to be symmetric and balanced, as was introduced in Section 2.1.3.
- A minimum fraction of material should be present in each fiber direction, as per the so-called *10% rule*.
- For laminates with varying thickness, the permitted frequency and location of ply drop-offs (i.e., the termination of a ply within the laminate) is constrained.
- Finally, a number of rules govern stacking sequence, such as constraints on the contiguity of equally oriented plies and the coverage of ply drop-offs.

CHAPTER

THREE

OPTIMIZATION OF TOW-STEERED STRUCTURES: STATE-OF-THE-ART

3.1 Structural Optimization

Within the set of boundary conditions outlined in the previous chapter, a multitude of possible designs exist, the collection of which is referred to as the *design space*. *Optimization* can be seen as the process of locating the extremum point in this space with regard to some measure of performance (Fig. 3.1.1).

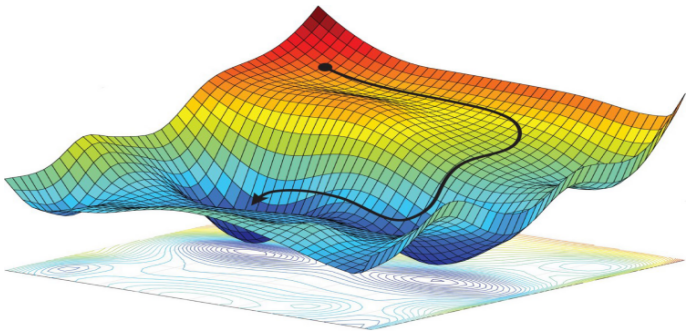

Figure 3.1.1: Design optimization visualized as a minimization problem [57].

Design optimization is a vastly researched topic and has emerged as an indispensable tool for modern engineering design. This development has been enabled by the exponential improvement of computing over the past four decades, combined with increasingly accurate methods for numerical simulation. Structural optimization will likely continue to gain importance within the field of mechanical engineering, being instrumental in confronting the increasingly complex engineering challenges and stringent performance requirements of the future.

3.1.1 General Optimization Problem

A structural optimization problem consists of the following features [58]:

- **Design Variable (x)** - The parameters of the design that can be changed during the optimization to achieve different responses from the system.
- **State variable (y)** - A measurement of an output characteristic (response) of the system. For a mechanical structure, examples of responses are displacement, stress, strain, volume, mass, or stiffness.
- **Objective function (f)** - A function indicating a designs achievement with respect to the goal of the optimization. This function can be constructed from one or several state variables.
- **Constraint** - A numerical limit applied to a design or state variable. Three types of constraints are possible: (1) *Behavioral constraints* are constraints on the state variable y. (2) *Design constraints* are similar, but involve the design variable x. (3) For the present case, the *equilibrium constraint* is the matrix equilibrium equation for the finite element solution. The subset of the design space which satisfies all the constraints is called the *feasible region*.

The structural optimization problem then takes the form:

$$(\mathbb{SO}) \quad \begin{cases} \text{minimize } f(x,y) \text{ with respect to } x \text{ and } y \\ \text{subject to} \begin{cases} \text{behavioral constraints on } y \\ \text{design constraints on } x \\ \text{equilibrium constraint.} \end{cases} \end{cases}$$

3.1.2 Parameterization of Structures

When applying the general mathematical formulation above to a structure, x will represent some geometrical feature. The optimization problem is typically classified based on which geometrical feature is parameterized. These basic concepts serve as the foundation for the composite optimization techniques discussed in this thesis.

Size optimization (Fig. 3.1.2) - In finite elements, the behavior of structural elements, such as shells and truss members, are defined by input parameters, such as shell thickness and cross-sectional area. In size optimization, these input parameters are used as design variables (DVs). A typical sizing problem for a composite structure would be determining the optimal thickness of a ply (or group of plies).

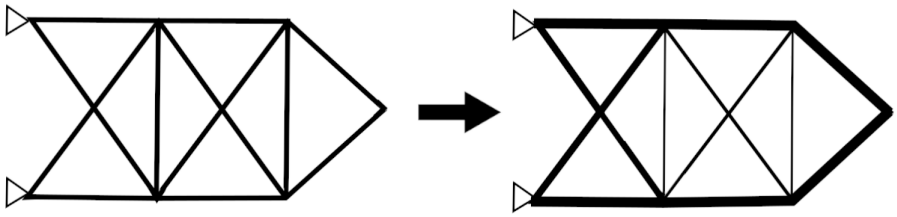

Figure 3.1.2: Size optimization.

Topology optimization (Fig. 3.1.3) - Topology optimization is concerned with the material distribution over a domain Ω, i.e., which points in space should be material and which should remain void (no material). Structures are typically parameterized by assigning an "equivalent density" $\boldsymbol{\rho}$ to each element, where 1 and 0 are equivalent to 100% and 0% material, respectively. Penalization techniques for intermediate densities are formulated to incentivize solutions containing discrete density values, i.e., either 1 or 0. Topology optimization can be two- or three-dimensional, and is currently widely used at the concept stage of structural design.

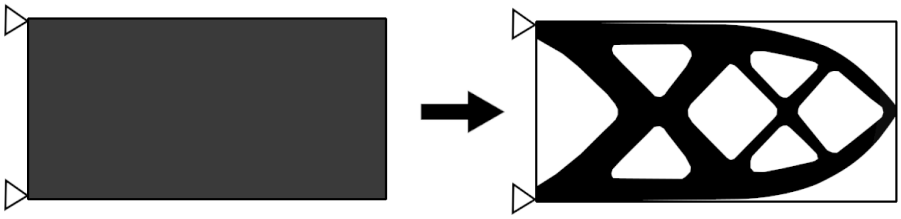

Figure 3.1.3: Topology optimization.

Free-size optimization (Fig. 3.1.4) - Whereas topology optimization aims to generate structures with discrete properties (solid or void), free-size optimization deals with design parameters that may vary continuously. Here, x represents the same geometrical features as for size optimization, except that DVs are assigned to each element separately instead of a group of elements. The resulting continuous distribution of material makes it well-suited for the design of variable-thickness shell structures, such as VS composite laminates.

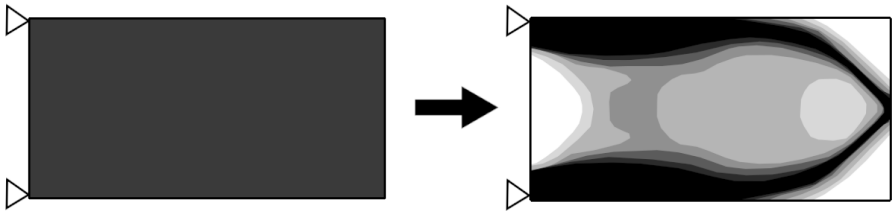

Figure 3.1.4: Free-size optimization.

3.1.3 Mathematical Programming

When solving optimization problems, structural solvers typically utilize nonlinear numerical optimization, formally known as mathematical programming. These methods can be categorized into two classes: *gradient-based* and *gradient-free* (also called *direct search*) [59].

Gradient-based algorithms utilize the gradient of the objective and constraint functions to find the direction towards the optimal solution. This approach guarantees rapid convergence to a constrained minimum. However, this minimum does not guarantee global optimality if the design problem features multiple local minima (the objective function is non-convex). Gradient-based methods also require the objective and constraints to be differentiated. This is an often pain-staking process, especially because most practical design problems do not have objectives and constraints for which closed–form expressions exist [60].

In contrast, *direct search* methods do not require any gradient information. Instead, they explore the design space by probing different points, using a set of rules or heuristics to determine where to search next. This attribute is a significant advantage in cases where sensitivities of structural responses are difficult to calculate. It also enables the solution of problems where the objective function is non-smooth or discontinuous. Direct search methods are less sensitive to the choice of starting point and guarantee global optimality given an adequately long solution time. On the other hand, their convergence speed tends to be slower, requiring a much larger number of function evaluations to approach an optimum.

Computational cost is one of the most critical factors when selecting an optimization algorithm. For most practical design problems, gradient-free methods scale to about $\mathcal{O}(10)$ DVs before becoming prohibitively expensive. On the other hand, gradient-based methods can scale to over $\mathcal{O}(10^3)$ DVs without a significant increase in expense [61]. For this reason, considering the inherent advantages of direct-search methods, these are typically used when there are few DVs and many constraints, whereas gradient-based methods are applied for the opposite case [62].

3.2 Optimization of Curvilinear Tow Paths

3.2.1 Fiber Angle Parameterization

To date, a multitude of methods has been proposed in the literature for the parameterization of tow-steered plies. These approaches can be categorized into the *functional*, *level-set*, and *element-based* fiber angle definitions.

The *functional* method represents fiber orientations as a function of the structural domain, and was first proposed by Gürdal and Olmedo [22]. In this approach, nonlinear functions such as NURBS, Bezier curves, or Lagrangian polynomials have been used, where the functional coefficients are taken as DVs [25, 63, 64]. This function defines a main tow path, which is duplicated and shifted over the domain to construct a ply. While this simple definition makes manufacturing constraints easy to enforce, the design space is highly limited compared to other methods. Its application is generally limited to basic plates and shells.

The *level-set* approach defines tow courses as the iso-contours of a level set function (LSF), first introduced by Brampton et al. [65], and later explored by a number of researchers [66, 67]. This parametrization inherently produces designs that are easily manufacturable with tow-steering. Since the boundary of the LSF is continuous, it will, in turn, define continuous fiber paths. The properties of the LSF can also be used to guarantee that tow courses are equally spaced and parallel. A limitation is that, to date, the incorporation of structural topology in LSF-based VAT design has remained an open research question.

The *element-based* fiber angle definition introduced by Hyer and Lee [14] is the most common parameterization scheme in the literature. Independent fiber angles are assigned to the laminate at each element of the FE model, i.e., at discretized regions (Fig. 3.2.1). This parametrization does not produce defined tow courses, but rather a scalar field, referred to as $\theta(x, y)$, describing the fiber angle variation across the domain. As a consequence, the finite width of the course is not considered. Instead, each course is considered to have an infinitesimal width, resulting in areas of continuous divergence and convergence in place of discrete overlaps or gaps.

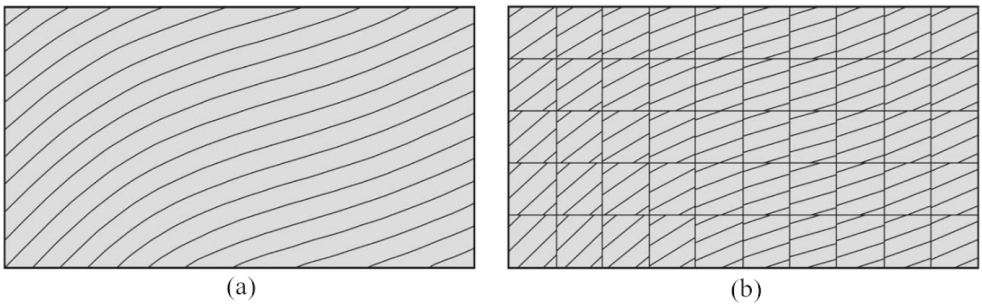

Figure 3.2.1: VAT ply representation (a) as a continuous fiber angle distribution (b) as discrete elements with constant fiber orientations [38].

Because of this, post-processing of the results is necessary to extract fiber paths, and manufacturing constraints are difficult to enforce. On the other hand, this scheme provides large design space and excellent versatility. In addition, it provides a straightforward means of combining fiber angle design with element-based topology optimization [68–71]. Because these factors are central to the design cases considered in this thesis, the element-based approach is selected as the parameterization scheme. This will be the focus of the remainder of the review in this chapter.

3.2.2 Path Continuity

When defining a set of discrete tow courses from the fiber angle scalar field $\theta(x, y)$, the typical method is to use streamlines, with each streamline representing the centerline of a tow [6]. A streamline is defined as a curve that runs parallel to the field direction, making this an intuitive approach. However, since the fiber direction is defined independently at each element, large changes in orientation between adjacent elements may occur, resulting in discontinuous fiber paths. Ensuring continuity is one of the main issues related to VAT design.

One approach to address this problem has been to use *lamination parameter design* [72–75]. This treats the laminated stiffness matrices as DVs instead of fiber angles. This has been found to improve the smoothness of the ply angle distribution, while also improving the speed and smoothness of optimization convergence.

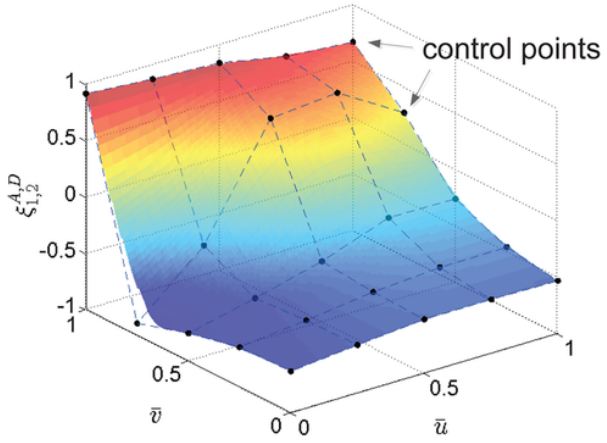

Figure 3.2.2: B-spline surface function used to parameterize fiber angles [76].

The second approach involves using a parameterization based on non-uniform rational basis splines (NURBS or B-splines) to ensure fiber continuity [9, 61, 77]. This employs B-splines as basis functions for the spatial variation of fiber orientation. A B-spline surface is defined by a set of control points (Fig. 3.2.2), which are used as DVs for optimization. The number and position of control points, the degree, and the knot vector of the spline functions can be altered to adjust design flexibility [76]. Since the fiber angle distribution takes on the properties of the B-spline surface, smoothness and high-order continuity are ensured. This also reduces the number of DVs compared to the discretized parameterization of fiber angles, improving the optimization's computational efficiency.

3.2.3 Implementation of Tow Path Constraints

The main challenge in enforcing the constraints from Section 2.2.3 is caused by the difficulty of formulating them as a constrainable state variable within the element-based parameterization scheme. Prior studies have primarily considered two manufacturing constraints: turning radius and gaps/overlaps.

Of these, minimum turning radius is the most commonly implemented [11]. This requires the curvature of the tows to be quantified. One approach evaluates this at a point-wise basis, computing the curvature at each element based on the angle at their adjacent elements [78]. Another method has been to derive the curvature from the fiber angle field $\theta(x, y)$ using the curl operator [6, 79]. This yields the directional derivative of the angle in the tangential direction, which is equivalent to the definition of curvature of a parametric curve.

Similarly, overlaps have been related using vector calculus differential operators (Fig. 3.2.3). Brooks et al. [6] introduced the quantity ψ, representing the flux per unit area passing through the boundary of an arbitrary control volume, obtained through the divergence operator. Using this definition, ψ can be used to predict the formation of gaps and overlaps. Blom et al. [80] used the streamlines of a 2D stream function, as found in fluid mechanics, to define the tow paths. This was used to derive an expression for the distance between streamlines, which could be constrained during optimization.

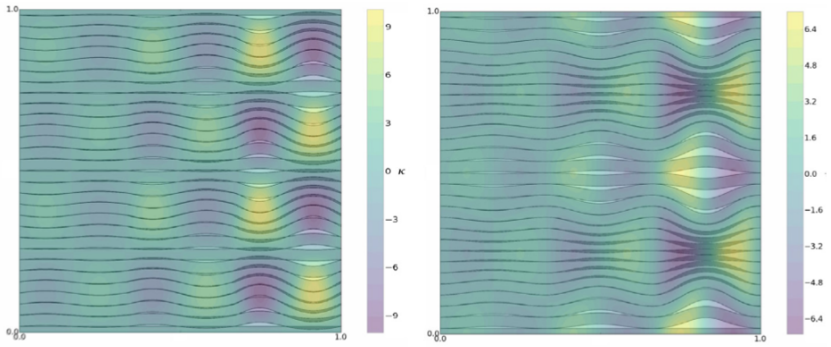

Figure 3.2.3: Quantification of (a) curvature using curl, κ, and (b) gaps/overlaps using divergence, ψ [6].

In addition to the development of constraints, methods for modeling the structural impact of gaps and overlaps using FEA have been the subject of several papers [4, 81]. A prevalent approach is the "smeared" thickness formulation introduced by Castro et al. [82], where discrete overlaps are approximated as a continuous scalar field representing local thickness buildup. This formulation was based on the tow width approximation by Blom et al. [83]. Tooren et al. [84] studied stiffness corrections using this approach, with tests showing the results to be consistent with the expected gap/overlap distributions.

3.3 Composite Topology Optimization

3.3.1 Formulation Requirements

A number of studies have considered the simultaneous optimization of tow paths and ply topology. Due to most not having an experimental component, these studies tend to simplify the analysis by defining ply thickness as a continuous function, disregarding the discrete layer-wise nature of real-life laminates. For instance, Parnas et al. [38] constructed a bi-cubic Bezier surface to define ply thickness while optimizing a flat panel with a circular cutout. Brooks et al. [26] used B-spline surfaces to represent the ply thicknesses of a wing structure. While this continuous representation of ply thickness may provide an adequate approximation for the purpose of simulation, it is insufficient for an experimental study where results must also be practically manufacturable.

Instead, a formulation is required that spatially defines the ply arrangement of the laminate at each point of the structure. This problem is generally defined by considering a stack of plies over a domain Ω, where each ply has its own shape $\Omega_i \subset \Omega$ (Fig. 3.3.1). The ply shapes are biphasic, consisting of either material or void. Although this has many similarities to the conventional topology optimization problem outlined in Section 3.1.2, formulating it as a mathematical programming problem introduces several additional complexities. This is mainly caused by the laminate-level constraints from Section 2.2, making the shapes of individual plies highly interdependent.

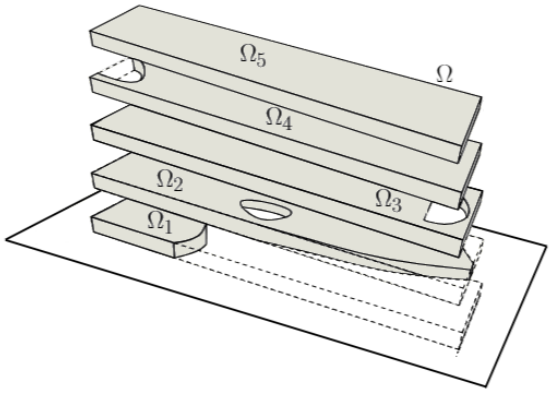

Figure 3.3.1: Illustration of the ply topology optimization problem.

3.3.2 Bi-Level Optimization Approach

Composite topology optimization is a research field of its own, and as such, a number of established techniques are found in the literature. An extensive overview of these techniques is provided by Ghiasi et al. [85].

Of these options, the natural extension of the aforementioned continuous-thickness formulations would be to use a so-called *bi-level* (or *decomposition*) scheme (Fig. 3.3.2). This involves dividing the laminate design problem into smaller sub-problems that correspond to different levels of analysis. At the system level (such as a fuselage or wing), a continuous representation of the composite material is used, often identical to those described previously. Meanwhile, at the subsystem level (laminate layup and stacking sequence), the material is treated as discrete. Thus, in the context of this thesis, this technique ensures that the overall design approach is consistent with previous work on VAT design, while meeting the manufacturing requirements of laminated composites.

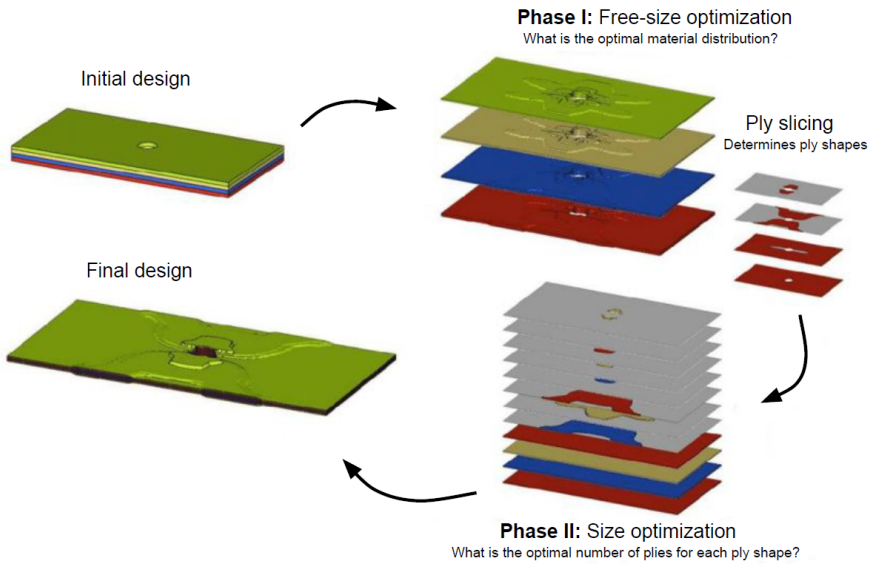

Figure 3.3.2: Typical bi-level ply topology optimization procedure [36].

CHAPTER
FOUR

NUMERICAL SOLUTION OF THE DESIGN STUDY

4.1 Solution Outline

Combining the concepts from the previous chapters to a solution of the design study involves selecting a set of design constraints and objectives, around which a suitable optimization framework can be constructed. The rationale behind this selection is summarized by reiterating the thesis objective into the following requirements:

1. Practical viability of the structure in the context of aircraft design, as defined in Section 2.2, is ensured.

2. The design approach is representative of current methods in literature, as presented in sections 3.2 and 3.3.

3. The degree of computational complexity allows for accurate solution using the mathematical programming techniques from Section 3.1.3.

4.1.1 Optimization Problem Statement

The design objective is to maximize stiffness for a given material amount. The elastic strain energy, known as the compliance of the structure, is used as the objective function. This is calculated as:

$$f_c = {}^1\!/_2 \mathbf{a}^T \mathbf{K} \mathbf{a} \tag{4.1}$$

Compliance is the most common objective function for stiffness maximization when performing structural size- and topology optimization [86]. There are a number of reasons why this is preferred over other functions (i.e., displacement). First, this function has favorable convergence properties, resulting in quicker and smoother convergence towards a solution [58]. Second, it generates results that are intuitive, tending to produce structures with a more even distribution of stress compared to displacement minimization [85].

The available fiber angles are restricted based on the discussion on certifiability in Section 2.2.5. For the QI and VS designs, the orientations are restricted to 0°, ±45°, and 90°. For the VAT design, a reference orientation field θ_0 sets the local tow direction for the main tow pattern. The remaining three tow patterns are

defined by offsetting this reference field by 45°, −45°, and 90°. Furthermore, for the VAT design, plies are constructed using the overlap method. Compared to the tow drop method, this arrangement is more straightforward to model accurately since all tows within a ply are continuous (do not contain cuts/restarts) and, therefore, have uniform macroscopic properties. Because of this fiber continuity, the overlap method also yields the highest performance compared to other methods. This was demonstrated by Tatting and Gürdal [39], who compared the tow-drop and overlap techniques for plate structures with cutouts.

Ensuring path continuity is fundamental to obtaining practically manufacturable designs; thus, a parameterization scheme that enforces this is chosen. Minimum turning radius is another fundamental constraint, which, however, is chosen not to be enforced during optimization. Given the results from prior studies on similar geometries, tow course curvatures are expected to stay within the limits presented in Section 2.2.3 without the need for constraint.

In order to limit the scope of this thesis, some of the constraints in Section 2.2 are not considered in the numerical solution, and are only used for evaluation of the results. Most notably, the topology optimization stage will not enforce laminate design rules. Furthermore, no constraint on gap/overlap propagation is applied. The motivation for this is the absence of established standards with regard to these constraints for VAT structures, and the overall low number of studies that implement these aspects in the literature.

Finally, a resource constraint is required to limit the amount of material available to the solver. This is expressed as an upper bound on global mass, with the mass response being calculated from the sum of element contributions:

$$m = \sum_{(e)} (\rho A^{(e)} \sum t_k^{(e)}) \leq m_{\max} \tag{4.2}$$

Where ρ is the material density, $A^{(e)}$ is the area of the element, and $t_k^{(e)}$ is the thickness of the k^{th} ply in the element.

4.1.2 Optimization Procedure

To ensure continuity and smoothness, the tow path parameterization is based on a B-spline approach that has been implemented by several authors, including Brooks et al. [9] and Wu et al. [76]. The method for topology optimization is an adaptation of a bi-level scheme, as previously described, developed by Zhou et al. [87–89]. This methodology was later integrated into Altair's Optistruct structural solver [90], which has been adopted by several aircraft OEMs such as Bombardier Aerospace [88] and Airbus [91]. This choice of approach reflects the aim of basing the design study on methods that are widely used and well-documented.

The optimization problem is solved using the method of steepest descent, which represents one of the most common gradient-based algorithms [59]. First, the design problem features a large number of DVs and few constraints. Second, the cost of computing gradient data is comparatively low compared to the cost of function evaluation, as will be demonstrated in Section 4.2.7. Both of these factors favor the use of gradient-based methods.

4.2 Implementation

Figure 4.2.1 illustrates the steps involved in mapping the DVs, represented by the vector $\mathbf{x} = \{x_j\}$, to the objective and constraint functions. These responses and sensitivities are passed back to the optimizer to inform the design modification for the successive iteration, forming the cycle that constitutes the optimization process.

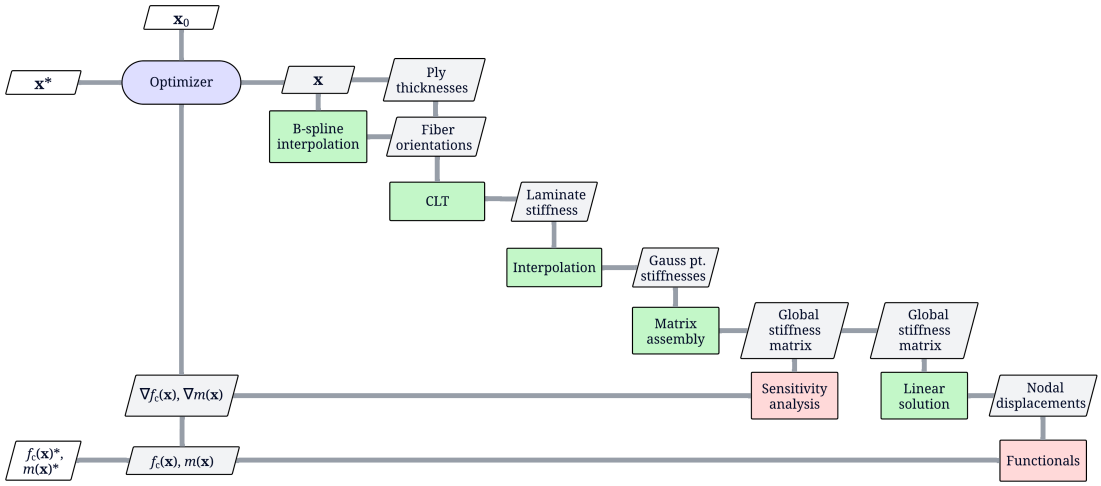

Figure 4.2.1: Extended design structure matrix (XDSM) of the solution. The program takes in the initial state $\mathbf{x}_0$, and returns the optimal solution $\mathbf{x}^*$ and the responses $f_c(\mathbf{x})^*$ and $m(\mathbf{x})^*$.

The implementation of these methods necessitates a significant degree of customization, as no commercial FEA solutions come pre-equipped these capabilities. The common approach in the literature is to obtain the structural responses using a commercial solver, typically MSC Nastran or Abaqus, while writing the program for the optimization procedure. For the present case, because of the relative simplicity of the linear static analysis, and to allow for greater flexibility, it is chosen to implement both these aspects using Python. This enhances the simplicity and readability of the solution, which is available in Appendix A.

4.2.1 Laminate Stiffness

First, the laminate stiffness within a given element must be expressed in terms of the design parameters, i.e., the thickness t and orientation θ of each ply defined in that element. Given the material constants of a ply, the reduced material stiffness matrix from Eq. 2.2 is written as [32]:

$$\mathbf{Q}' = \frac{1}{1 - v_{12}v_{21}} \begin{bmatrix} E_{11} & v_{21}E_{11} & 0 \\ v_{12}E_{22} & E_{22} & 0 \\ 0 & 0 & (1 - v_{12}v_{21})G_{12} \end{bmatrix} \tag{4.3}$$

Where:

$$\frac{1}{G_{12}} = \frac{1 + v_{21}}{E_{11}} + \frac{1 + v_{12}}{E_{22}} \tag{4.4}$$

Next, a transformation is required for when the principal orthotropy directions (1, 2) are rotated by the angle θ with respect to the global axes (x, y). The stress-strain relationship in the local axes is expressed as [41]:

$$\boldsymbol{\sigma}' = \mathbf{Q}'\boldsymbol{\varepsilon}' \tag{4.5}$$

Where $\mathbf{Q}'$ is given by Eq. 4.3. The strains in the local axes are expressed in terms of the global strains as:

$$\boldsymbol{\varepsilon}' = \mathbf{T}\boldsymbol{\varepsilon} \quad , \quad \boldsymbol{\varepsilon}' = \begin{bmatrix} \varepsilon_1 & \varepsilon_2 & \gamma_{12} \end{bmatrix} \tag{4.6}$$

Where $\mathbf{T}$ is the transformation matrix:

$$\mathbf{T} = \begin{bmatrix} \cos^2\theta & \sin^2\theta & \sin\theta\cos\theta \\ \sin^2\theta & \cos^2\theta & -\sin\theta\cos\theta \\ -2\sin\theta\cos\theta & 2\sin\theta\cos\theta & \cos^2\theta - \sin^2\theta \end{bmatrix} \tag{4.7}$$

The corresponding expression for stresses is obtained using virtual work equivalent in global and local axes:

$$\boldsymbol{\sigma} = \mathbf{T}^T\boldsymbol{\sigma}' \quad \text{and} \quad \boldsymbol{\sigma} = [\mathbf{T}^{-1}]^T\boldsymbol{\sigma} \tag{4.8}$$

Combining Eqs. 4.6, 4.8, and 4.5, the final expression for the transformation is obtained:

$$\mathbf{Q} = \mathbf{T}^T\mathbf{Q}'\mathbf{T} \tag{4.9}$$

Where $\mathbf{Q}$ is the material stiffness of the ply in the global reference system. Since the design problem is two-dimensional, out-of-plane moments $\mathbf{M}$ and curvatures $\boldsymbol{\kappa}$ have a value of zero, allowing the CLT equations (Eq. 2.3) to be rewritten as:

$$\begin{bmatrix} N_x \\ N_y \\ N_{xy} \end{bmatrix} = \begin{bmatrix} A_{11} & A_{12} & A_{16} \\ A_{12} & A_{22} & A_{26} \\ A_{13} & A_{26} & A_{66} \end{bmatrix} \begin{bmatrix} \varepsilon_x^0 \\ \varepsilon_y^0 \\ \gamma_{xy}^0 \end{bmatrix} \tag{4.10}$$

With the matrix entries given by:

$$A_{ij} = \sum_{k=1}^{N} (\bar{Q}_{ij})_k t_k; \quad i,j = 1,2,6 \tag{4.11}$$

Where $(\bar{Q}_{ij})_k$ are the coefficients of $\mathbf{Q}$ and t_k is the thickness of the k^{th} ply. This is divided by the total laminate thickness, resulting in the final expression for the laminate stiffness matrix $\mathbf{D} = \{D_{ij}\}$:

$$D_{ij} = \frac{\sum_{k=1}^{N} (\bar{Q}_{ij})_k t_k}{\sum_{k=1}^{N} t_k}; \quad i,j = 1,2,6 \tag{4.12}$$

4.2.2 Finite Element Model

The choice of element type should align with the specific needs of the analysis, considering the trade-off between computational efficiency and solution accuracy. For this model, the linear triangular element is chosen. This has a low computational cost, which is a particularly beneficial characteristic for a computationally intensive optimization problem such as the present case. Conversely, its accuracy is limited by its linear shape functions, yielding constant strain and stress fields within the element. This makes local mesh refinement in areas of high strain gradients critical to the accuracy of the model.

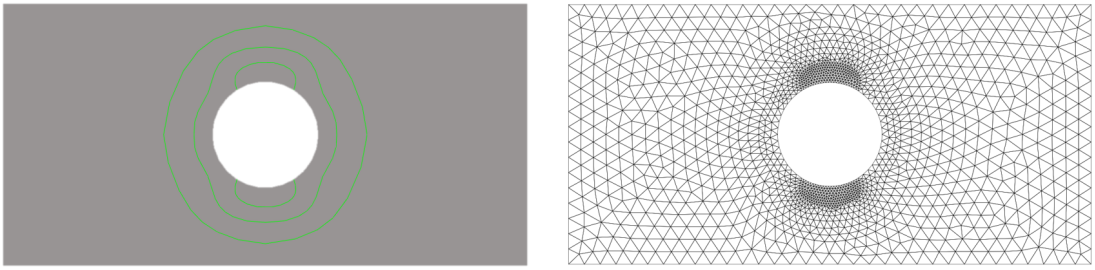

Figure 4.2.2: Left: subdivision of structure in CAD. Right: FE-mesh generated by pre-processor.

From the field of fracture mechanics, as well as from prior studies in the literature, it is well-known that axially loaded structures with holes will experience stress concentrations in the proximity of the hole boundary. Based on the anticipated stress gradients within the plate, the CAD model is subdivided into regions where mesh density is applied separately (Fig. 4.2.2). The CAD file is subsequently imported into the FE pre-processor (Altair HyperMesh), and used to generate a mesh containing a total of 2945 elements. This has an element size of 7 mm over most of the plate, decreasing to 1 mm at the anticipated stress concentration zones.

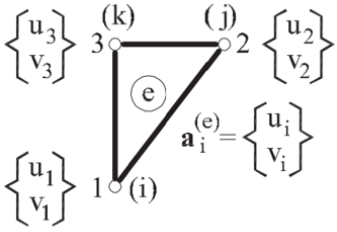

Figure 4.2.3: DOFs of a two-dimensional 3-noded element

The element stiffness matrix $\mathbf{K}^{(e)}$, relating the load vector to the nodal displacements u and v (Fig. 4.2.3), is derived for the linear 3-noded triangle in Appendix B. This is written as:

$$\mathbf{K}^{(e)} = \iint_{A^{(e)}} \begin{bmatrix} \mathbf{B}_1^T \\ \mathbf{B}_2^T \\ \mathbf{B}_3^T \end{bmatrix} \mathbf{D} \begin{bmatrix} \mathbf{B}_1 & \mathbf{B}_2 & \mathbf{B}_3 \end{bmatrix} t dA$$

$$= \iint_{A^{(e)}} \begin{bmatrix} \mathbf{B}_1^T\mathbf{D}\mathbf{B}_1 & \mathbf{B}_1^T\mathbf{D}\mathbf{B}_2 & \mathbf{B}_1^T\mathbf{D}\mathbf{B}_3 \\ \ddots & \mathbf{B}_2^T\mathbf{D}\mathbf{B}_2 & \mathbf{B}_2^T\mathbf{D}\mathbf{B}_3 \\ Symm. & \ddots & \mathbf{B}_3^T\mathbf{D}\mathbf{B}_3 \end{bmatrix} tdA \tag{4.13}$$

Where $\mathbf{B}_i$ are the strain-displacement matrices obtained from the shape functions of the element, and $\mathbf{D}$ is the laminate stiffness from Eq. 4.12. The element stiffness submatrix $\mathbf{K}_{ij}^{(e)}$ linking nodes i and j of the element is thereby expressed as:

$$\mathbf{K}_{ij}^{(e)} = \iint_{A^{(e)}} \mathbf{B}_i^T\mathbf{D}\mathbf{B}_j tdA \tag{4.14}$$

For a homogeneous material the integrand is constant, yielding the expression [41]:

$$\mathbf{K}_{ij}^{(e)} = \left(\frac{t}{4A}\right)^{(e)} \begin{bmatrix} b_i & 0 & c_i \\ 0 & c_i & b_i \end{bmatrix} \begin{bmatrix} D_{11} & D_{12} & D_{13} \\ D_{21} & D_{22} & D_{23} \\ D_{31} & D_{32} & D_{33} \end{bmatrix} \begin{bmatrix} b_j & 0 \\ 0 & c_j \\ c_j & b_j \end{bmatrix} \tag{4.15}$$

The resulting element stiffness matrix is written as:

$$\mathbf{K}^{(e)} = \begin{bmatrix} \mathbf{K}_{11}^{(e)} & \mathbf{K}_{12}^{(e)} & \mathbf{K}_{13}^{(e)} \\ \ddots & \mathbf{K}_{22}^{(e)} & \mathbf{K}_{23}^{(e)} \\ symm. & \ddots & \mathbf{K}_{33}^{(3)} \end{bmatrix} \tag{4.16}$$

Where each submatrix has the dimension 2-by-2 (each node having two DOFs). The equilibrium equations are obtained by establishing that the nodes are in equilibrium, meaning the sum of all the forces at each node j balances the externally applied point load $\mathbf{p}_j = \begin{bmatrix} P_{x_j} & P_{y_j} \end{bmatrix}^T$, such that:

$$\sum_e \mathbf{q}_i^{(e)} = \mathbf{p}_j \quad , \quad j = 1, N \tag{4.17}$$

Where the sum refers to the elements sharing the node j, and N is the total number of nodes in the mesh. The local matrix equilibrium equation is obtained as:

$$\mathbf{K}^{(e)}\mathbf{a}^{(e)} = \mathbf{q}^{(e)} \tag{4.18}$$

Where $\mathbf{a}^{(e)}$ and $\mathbf{q}^{(e)}$ represent the nodal displacements and point loads, respectively. The global stiffness matrix $\mathbf{K}$, as well as the global displacement and equivalent nodal force vectors $\mathbf{a}$ and $\mathbf{f}$ are assembled from these element contributions. This procedure places each contribution belonging to a local node according to its DOF in the global system, as represented here by i, j, and k.

Element	Node		Nodal variables	
	Local	Global	Local	Global
(e)	1	i	u_1 v_1	u_i v_i
	2	j	u_2 v_2	u_j v_j
	3	k	u_3 v_3	u_k v_k

Table 4.2.1: Correspondence between local and global DOFs.

A distributed load is applied along the right boundary of the plate. In FEA, boundary conditions may only be applied at the nodes of the model, meaning the distributed load must be subdivided into discrete point-loads. These are applied by means of Neumann boundary conditions, where the forces corresponding to the point loads are added to the entries of the load vector $\mathbf{f}$ associated with the respective DOFs.

Likewise, the constraint at the left plate boundary is applied on a nodal basis. This is done using Dirichlet boundary conditions, which prescribe a displacement, 0 in this case, to the selected nodes. This is implemented by setting the corresponding rows and columns of the stiffness matrix $\mathbf{K}$ to zero, eliminating the DOFs associated with the constrained nodes.

Finally, the global elastic response is obtained by solving the global matrix equilibrium equation:

$$\boxed{\mathbf{Ka} = \mathbf{f}} \tag{4.19}$$

4.2.3 Failure Prediction

The Tsai-Hill failure criterion is used to predict the first-ply failure of the laminate. This is chosen to ensure consistency with the approaches in prior studies, as described in Section 2.1.4.

Hill extended the von Mises yield criterion to anisotropic materials, and Tsai adapted Hill's criterion to composite materials by relating its coefficients to the longitudinal, transverse, and shear failure strengths, X_{11}, X_{22}, and S_{12}, respectively. This criterion is failure mode independent, as it does not predict the way in which the material fails. Additionally, it does not distinguish between tensile and compressive strength, which are often different for composite materials. This is not an issue in the present case, as the structures under study are primarily subjected to tensile stresses. According to this criterion, ply failure appears when [29]:

$$\left(\frac{\sigma_{11}}{X_{11}}\right)^2 - \left(\frac{\sigma_{11}\sigma_{22}}{X_{11}^2}\right) + \left(\frac{\sigma_{22}}{X_{22}}\right)^2 + \left(\frac{\tau_{12}}{S_{12}}\right)^2 \geq 1 \tag{4.20}$$

Where σ_{11}, σ_{22}, and τ_{12} are the stress components in the principal material directions. To obtain these stress components within an element, the element strain tensor is first found as:

$$\begin{bmatrix} \varepsilon_x \\ \varepsilon_y \\ \gamma_{xy} \end{bmatrix} = \begin{bmatrix} \frac{\partial N_1}{\partial x} & 0 & \frac{\partial N_2}{\partial x} & 0 & \frac{\partial N_3}{\partial x} & 0 \\ 0 & \frac{\partial N_1}{\partial y} & 0 & \frac{\partial N_2}{\partial y} & 0 & \frac{\partial N_3}{\partial y} \\ \frac{\partial N_1}{\partial y} & \frac{\partial N_1}{\partial x} & \frac{\partial N_2}{\partial y} & \frac{\partial N_2}{\partial x} & \frac{\partial N_3}{\partial y} & \frac{\partial N_3}{\partial x} \end{bmatrix} \begin{bmatrix} u_1 \\ v_1 \\ u_2 \\ v_2 \\ u_3 \\ v_3 \end{bmatrix} = \mathbf{B}\mathbf{a}^{(e)} \tag{4.21}$$

Where $\mathbf{B}$ is the strain-displacement matrix from Eq. 4.13 and $\mathbf{a}^{(e)}$ is derived from the displacement vector $\mathbf{a}$. The ply stresses are determined using Hooke's law:

$$\begin{bmatrix} \sigma_x \\ \sigma_y \\ \tau_{xy} \end{bmatrix} = \mathbf{Q} \begin{bmatrix} \varepsilon_x \\ \varepsilon_y \\ \gamma_{xy} \end{bmatrix} \tag{4.22}$$

Where $\mathbf{Q}$ is the elastic stiffness matrix of the ply, and the stress components σ_x, σ_y and τ_{xy} are expressed in terms of the global axes (x, y). To obtain the stresses referred to the principal material axes $(1, 2)$ required for the Tsai-Hill criterion, the following transformation is applied:

$$\begin{bmatrix} \sigma_{11} \\ \sigma_{22} \\ \tau_{12} \end{bmatrix} = \mathbf{T} \begin{bmatrix} \sigma_x \\ \sigma_y \\ \tau_{xy} \end{bmatrix} \tag{4.23}$$

Where $\mathbf{T}$ is the transformation matrix from Eq. 4.7.

4.2.4 Optimization Phase I

At this phase, the optimal material distribution is obtained through free-size optimization. Ply thicknesses are permitted to take any real number value, resulting in a continuous distribution of material (Fig. 4.2.4). The design variables control the total thicknesses of all contiguous plies of the same orientation, referred to as a "super-ply." The laminate consists of four super-plies, one for each possible ply orientation, both for the VS and VAT optimization cases. With each super-ply assigned a thickness variable at each element, the total number of free-size variables equals $4 \cdot n_e$:

$$\mathbf{t} = \begin{bmatrix} t_1 & t_2 & \dots & t_n \end{bmatrix} \tag{4.24}$$

A lower bound on the design variables, a so-called box constraint, is applied to control the ply thicknesses:

$$t_{min} \leq t_i \tag{4.25}$$

Where t_{min} is a small non-zero value, with the purpose of preventing the assembled stiffness matrix from becoming singular.

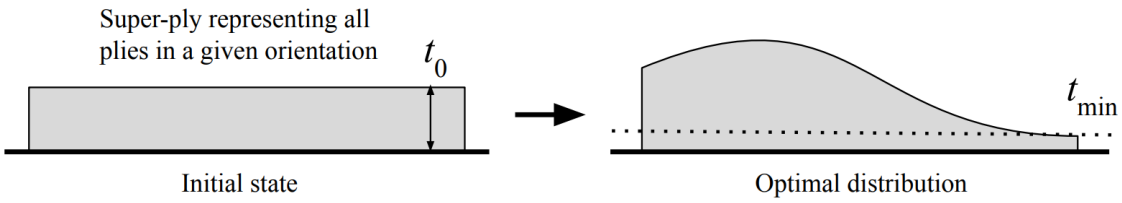

Figure 4.2.4: Optimization of a super-ply using the free-size concept, resulting in a continuous distribution of material.

At the same time, the optimal tow orientation field $\theta(x, y)$ is determined. This field is parameterized through a B-spline surface function, with the ply angle of each element obtained by evaluating this function at the centroid of the element. A B-spline surface is mathematically defined as [61]:

$$P\,(u, v) = \sum_{i=1}^{m} \sum_{j=1}^{n} B_i(u) B_j(v) C_i \tag{4.26}$$

Where $P(u, v)$ is the fiber angle at a parametric location (u, v), C_i are the control point values, and B_k are the piecewise-polynomial basis functions. In this case, the parametric coordinates $(u,\ v)$ are defined to be identical to the global axes $(x,\ y)$. The control points are distributed in a circular pattern (Fig. 4.2.5) to maintain an adequate resolution at the boundary of the cutout.

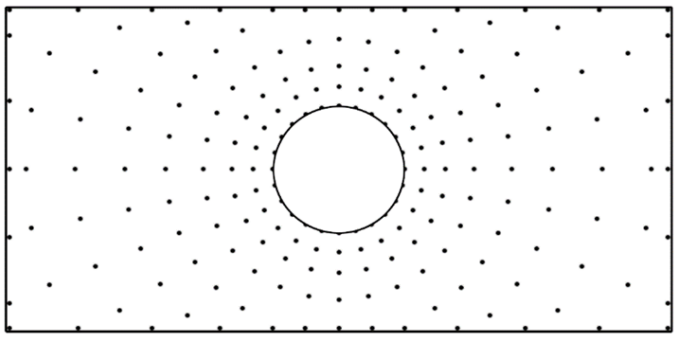

Figure 4.2.5: B-spline control point distribution.

The second design variable (main tow pattern) then consists of a set of control point values (C_i) and takes the form:

$$\mathbf{C} = \begin{bmatrix} C_1 & C_2 & \dots & C_n \end{bmatrix} \tag{4.27}$$

The optimization variables of Phase I amount to a total of 11916, and are grouped into the vector:

$$\mathbf{x} = \begin{bmatrix} C_1 & \dots & C_n & t_1 & \dots & t_n \end{bmatrix} \tag{4.28}$$

4.2.5 Optimization Phase II

In Phase II, ply shapes are defined using a discrete interpretation of the free-size results from Phase I by capturing different level-sets of the thickness field. The discrete ply shapes resulting from this procedure, referred to as ply-bundles, are

then subjected to size optimization to determine the optimal number of plies for each shape (Fig. 4.2.6).

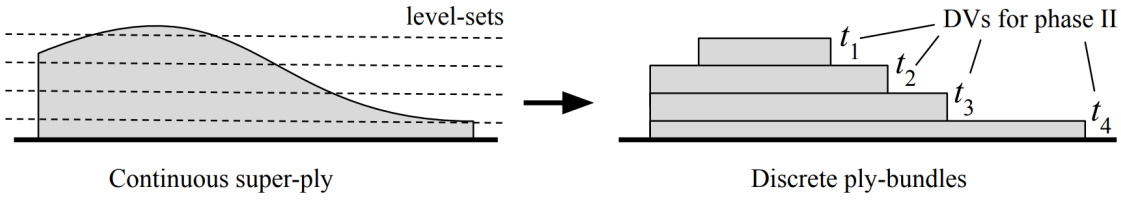

Figure 4.2.6: Discrete interpretation of the continuous material distribution using level-sets.

The number of ply-bundles must be determined as a tradeoff between true representation of the thickness field (better performance) and the complexity of the ply tailoring (higher manufacturing effort). A typical number is to define four ply-bundles per super-ply [36], in this case resulting in 16 size variables per design:

$$\mathbf{x} = \begin{bmatrix} t_1 & \dots & t_2 & \dots & t_{16} \end{bmatrix} \tag{4.29}$$

The level-set positions are determined by trial and error. These level-sets are also used as the initial state for the size variables. After solving the size optimization, the final designs are obtained by rounding all ply thicknesses to the nearest manufacturable value. A drawback of this method is that small discrepancies in terms of mass inevitably arise between the designs. For this reason, all measures of performance are normalized for mass (*specific* compliance, strength, and stiffness).

Before performing this optimization stage, it is necessary to determine the thickness variation within the plies of the VAT design resulting from tow overlaps. A smeared thickness approach, similar to the one presented by Tooren et al. [84] is applied, where the result is a continuous field approximating the local ply thickness.

This is based on the fact that, when using a vector field to define infinitesimally narrow tow paths, the degree of overlap (i.e., the relative thickness at a point in the ply) can be defined as being proportional to the density of the streamlines of this field. To obtain a scalar field describing streamline density, a fluid mechanics analogy is applied, whereby streamline density for incompressible fluids is proportional to fluid velocity. This quantity is computed by discretizing the domain into 0.5mm square cells. The flow velocity V is found by setting the flow direction at each cell equal to the fiber direction $\theta(x, y)$ at that point, and applying the continuity equation $\nabla V = 0$. This calculation requires a boundary condition, which is provided by assigning a constant value to V at the plate boundary, meaning tow paths are distributed equidistantly along this "starting point". Finally, local thickness is obtained by normalizing V by the nominal thickness of the ply.

4.2.6 Steepest Descent Algorithm

In the method of steepest descent, the step size is chosen such that the maximum decrease of the objective function is achieved at each individual step. This method is based on the observation that the objective function f decreases fastest at a

point $\mathbf{x}$ if one moves in the direction of the negative gradient of f at $\mathbf{x}$, such that [59]:

$$\mathbf{x}_{n+1} = \mathbf{x}_n - \gamma \nabla f(\mathbf{x}_n) \tag{4.30}$$

Where n denotes the iteration of the state variable $\mathbf{x}$. It follows that for a small enough step size γ, then $f(\mathbf{x}_{n+1}) \leq f(\mathbf{x}_n)$. Starting from an initial guess $\mathbf{x}_0$ and considering the sequence $\mathbf{x}_0$, $\mathbf{x}_1$, $\mathbf{x}_2$, ..., the result is a monotonic sequence which converges at a local minimum.

$$f(\mathbf{x}_0) \geq f(\mathbf{x}_1) \geq f(\mathbf{x}_2) \geq \cdots$$

The step size γ is determined by performing a line search in the gradient direction to locate a minimizer. A typical sequence resulting from this procedure is indicated, with each step being orthogonal to the previous iteration (Fig. 4.2.7).

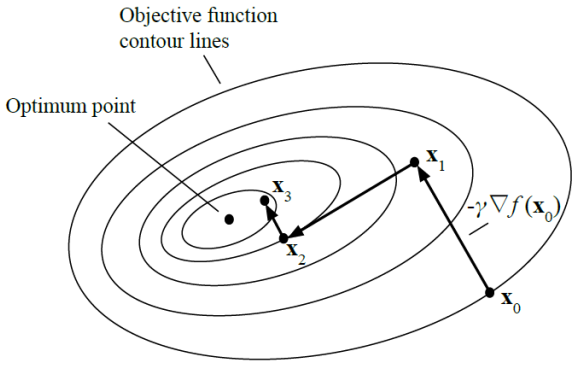

Figure 4.2.7: Solution convergence for the method of steepest descent.

The gradient tends towards zero as the minimizer is approached. In order to determine when the optimization should end, a convergence criterion in the form of an objective tolerance ε is introduced. This evaluates the change of the objective function (convergence) between iterations. When this change is lower than the objective tolerance for two consecutive iterations, the model is considered to have converged at a solution.

$$\frac{f(\mathbf{x}_n) - f(\mathbf{x}_{n+1})}{f(\mathbf{x}_n)} \leq \varepsilon \tag{4.31}$$

To impose constraints on the model, one of the many techniques for constrained optimization needs to be implemented. A simple modification typical for steepest descent involves the introduction of a *projection* [92]. This method changes the iterate to the following:

$$\mathbf{x}_{n+1} = p(\mathbf{x}_n - \gamma \nabla f(\mathbf{x}_n)) \tag{4.32}$$

Where $p(\mathbf{x})$ is a function that takes the unconstrained $\mathbf{x}$ to the nearest point inside the space of feasible solutions (Fig. 4.2.8). This projection is often complicated to compute, and may in many cases have to be computed numerically, which in itself entails solving a separate optimization algorithm. However, as the only behavioral constraint on the system is the resource constraint $m(\mathbf{x}) \leq m_{\max}$, the projection

becomes straightforward. Owing to $m(\mathbf{x})$ being a linear function, the shortest path to the constraint boundary will always be in the direction of the constraint's derivative. This yields the expression:

$$p(\mathbf{x}) = \mathbf{x} - \lambda \nabla m(\mathbf{x}) \tag{4.33}$$

Where the step size λ is determined as a function of γ to keep $\mathbf{x}$ as close to the constraint boundary as possible.

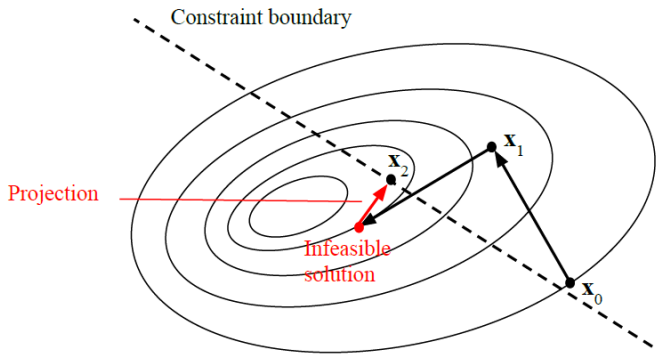

Figure 4.2.8: Constrained optimization using the projection method.

4.2.7 Sensitivity Analysis

Sensitivity analysis is the process of determining the gradient vector of the objectives and constraints. The choice of method is critical, as this is often the most computationally demanding operation of the solution process. Since the constraint gradient $\nabla m(\mathbf{x}_n)$ is constant with regard to $\mathbf{x}$, this section focuses only on the gradient of the objective function with respect to the DVs, expressed as:

$$\nabla f_c(\mathbf{x}_n) = \left[\frac{\partial f_c(\mathbf{x}_n)}{\partial x_1} \quad \frac{\partial f_c(\mathbf{x}_n)}{\partial x_2} \quad \dots \quad \frac{\partial f_c(\mathbf{x}_n)}{\partial x_j} \right] \tag{4.34}$$

The most straightforward approach is *finite-differencing*, wherein each DV x is perturbed by a small distance δ from the current iteration [92]. The gradient is approximated as the ratio of the function change to the DV perturbation:

$$\frac{\partial f_c(\mathbf{x}_n)}{\partial x_j} = \frac{f_c(x_j + \delta) - f_c(x_j)}{\delta} \tag{4.35}$$

This approach requires minimal changes to the code of the FE tool, making it straightforward to implement. A disadvantage is caused by the nature of digital computing, making the sensitivities subject to subtractive cancellation error. This limits the minimum step size δ and, therefore, the accuracy for nonlinear problems [61]. In addition, the computational cost is proportional to the number of DVs. This fact renders finite-differencing prohibitively expensive for the free-size optimization in Phase I, which has $\mathcal{O}(10^4)$ DVs, resulting in $\mathcal{O}(10^4)$ FEA solves per iteration. On the other hand, its simplicity makes it well-suited for the B-spline and size variables, which are mathematically more complex and fewer in number.

For the free-size variables, the *adjoint method* is an approach that addresses both scalability and accuracy. This method is based on the realization that the solution to any nonlinear problem can be written as follows [59]:

$$\boldsymbol{R}(x, y) = 0 \tag{4.36}$$

Where x are the design variables and y are the state variables. $\boldsymbol{R}$ is called the residual, a vector that equals zero when the governing equations of the physics problem are solved. The variable ψ, called the adjoint, is obtained by solving the linear equation:

$$\frac{\partial \boldsymbol{R}^T}{\partial y}\psi = \frac{\partial I^T}{\partial y} \tag{4.37}$$

For each objective or constraint function I. The sensitivities with respect to x are then obtained through:

$$\frac{dI}{dx} = \frac{\partial I}{\partial x} - \psi^T \frac{\partial \boldsymbol{R}}{\partial x} \tag{4.38}$$

In this expression, the partial derivative terms $-\frac{\partial \boldsymbol{R}}{\partial y}$, $\frac{\partial f}{\partial y}$, $\frac{\partial f}{\partial x}$, and $\frac{\partial \boldsymbol{R}}{\partial x}$ do not require the governing FE equations to be solved, and can thus be computed cheaply through finite-differencing. Meanwhile, the adjoint ψ is only solved once per iteration for each function of interest. This means that the cost of the adjoint method scales with the number of objectives and constraints rather than the number of DVs [59]. When using the compliance f_c as the objective function, the adjoint variable at iteration n is found by combining Eqs. 4.37 and 4.1 as:

$$\mathbf{K}(\mathbf{x}_n)\psi = \left(\frac{f_c(\mathbf{x}_n, \mathbf{a}(\mathbf{x}_n))}{\partial \mathbf{a}}\right)^T = \mathbf{f}(\mathbf{x}_n) \tag{4.39}$$

This system of equations is identical to the equilibrium equations. Thus, it can be concluded that $\psi = \mathbf{a}(\mathbf{x}_n)$. Insertion into Eq. 4.38 yields the final expression [58]:

$$\begin{aligned}\frac{\partial f_c(\mathbf{x}_n)}{\partial x_j} &= \frac{\partial \mathbf{f}(\mathbf{x}_n)^T}{\partial x_j}\mathbf{a}(\mathbf{x}_n) + \mathbf{a}(\mathbf{x}_n)^T\left(\frac{\partial \mathbf{f}(\mathbf{x}_n)}{\partial x_j} - \frac{\partial \mathbf{K}(\mathbf{x}_n)}{\partial x_j}\mathbf{a}(\mathbf{x}_n)\right) \\ &= 2\mathbf{a}(\mathbf{x}_n)^T\frac{\partial \mathbf{f}(\mathbf{x}_n)}{\partial x_j} - \mathbf{a}(\mathbf{x}_n)^T\frac{\partial \mathbf{K}(\mathbf{x}_n)}{\partial x_j}\mathbf{a}(\mathbf{x}_n)\end{aligned} \tag{4.40}$$

4.3 Optimization Results

In selecting the material for this study, it should be considered that carbon fibers are manufactured in a wide variety of grades, with mechanical properties tailored to meet specific engineering requirements. The chosen material is the 150 g XPREG XC130 UD prepreg carbon/epoxy reinforcement. This features an intermediate modulus, high tensile strength fiber, chosen to ensure similarity to the materials used in primary aircraft structures, such as the T800S fiber predominantly used in the Boeing 787 [93]. The mechanical properties of a cured ply are provided in Table 4.3.1.

Property	Symbol	Unit	Value
Modulus, longitudinal	E_{11}	GPa	130
Modulus, transverse	E_{22}	GPa	10
Modulus, shear	G_{12}	GPa	5
Poisson's ratio	v_{12}	-	0.3
Strength, longitudinal	X_{11}	MPa	645
Strength, transverse	X_{22}	MPa	60
Strength, shear	S_{12}	MPa	69
Density	ρ	g/cm^3	1.587
Thickness	t	mm	0.15

Table 4.3.1: Mechanical properties of 150 g XPREG XC130 UD [94].

4.3.1 Phase I

Free-size optimization is carried out using the benchmark QI design as the initial state of the DVs ($\mathbf{x}_0$). The mass of the QI design (11.90 g) is used as the resource constraint. The optimization is considered to have converged when the objective tolerance ε is below 0.5% for two consecutive iterations (Table 4.3.2).

Thickness constraint	Resource constraint	Objective tolerance
t_{min} [mm]	m_{max} [g]	ε [%]
0.001	11.90	0.5

Table 4.3.2: Phase I optimization parameters.

The VS design converged after 13 iterations (fig. 4.3.1), achieving a compliance of 5.708 Nmm (table 4.3.3). The optimized material distribution is shown in Fig. 4.3.2. The majority of the fibers (94.0% by weight) are aligned in the 0° direction, with concentrations of material around the upper and lower hole boundaries. The ply thickness for the 90° and ±45° fiber directions is negligible for most of the plate, apart from a few highly concentrated regions in proximity of the hole boundary.

Mass	Compliance	Convergence	Iteration no.
[g]	[Nmm]	[%]	[-]
11.90	5.708	0.488	13

Table 4.3.3: Free-size optimization result (VS).

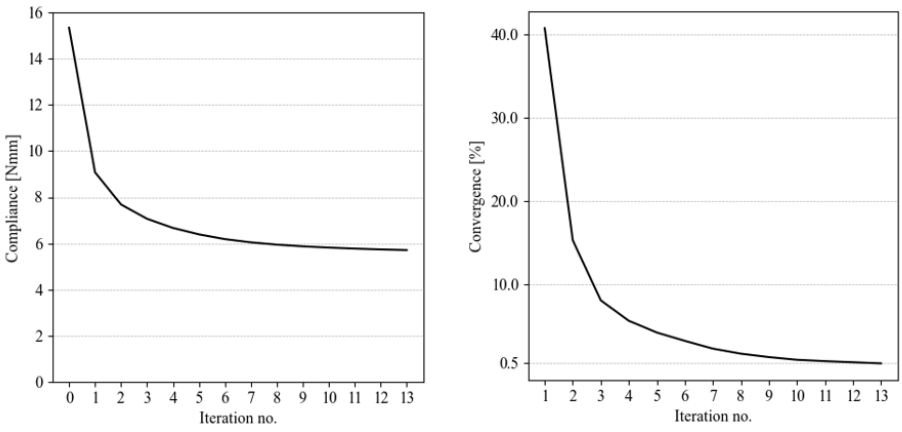

Figure 4.3.1: Iteration progress (VS). Left: compliance. Right: convergence.

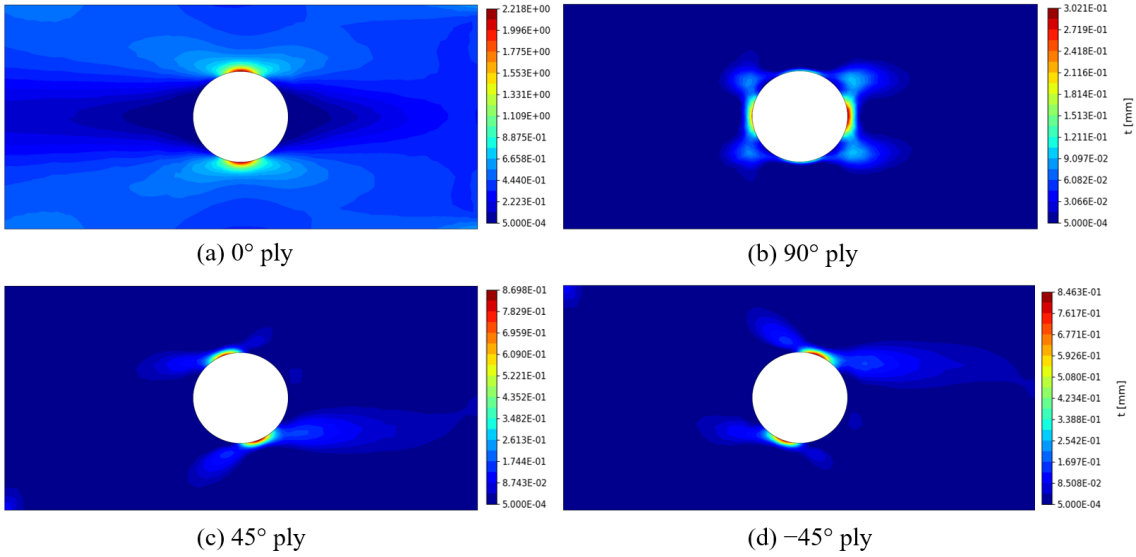

(a) 0° ply (b) 90° ply

(c) 45° ply (d) −45° ply

Figure 4.3.2: Ply thickness distribution (VS).

For the VAT design, convergence was reached after 12 iterations (fig. 4.3.3). The final compliance is 5.460 Nmm (table 4.3.4), representing a 4.3% improvement compared to VS at the free-size stage.

Mass	Compliance	Convergence	Iteration no.
[g]	[Nmm]	[%]	[-]
11.90	5.460	0.474	13

Table 4.3.4: Free-size optimization result (VAT).

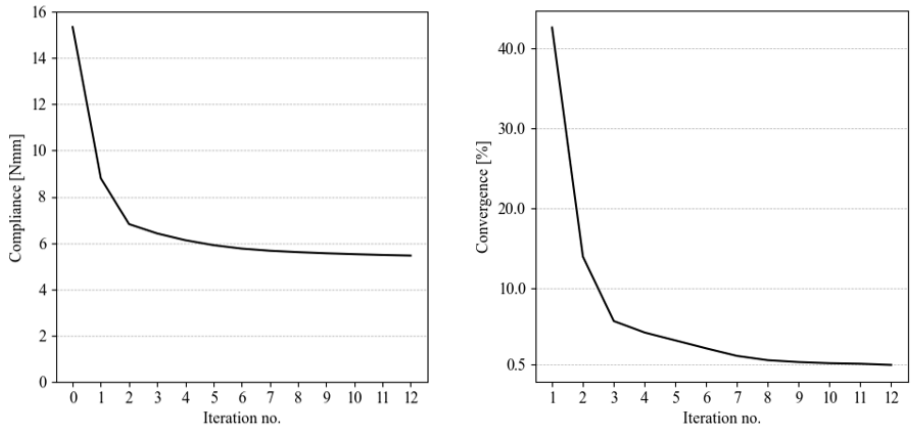

Figure 4.3.3: Iteration progress (VAT). Left: compliance. Right: convergence.

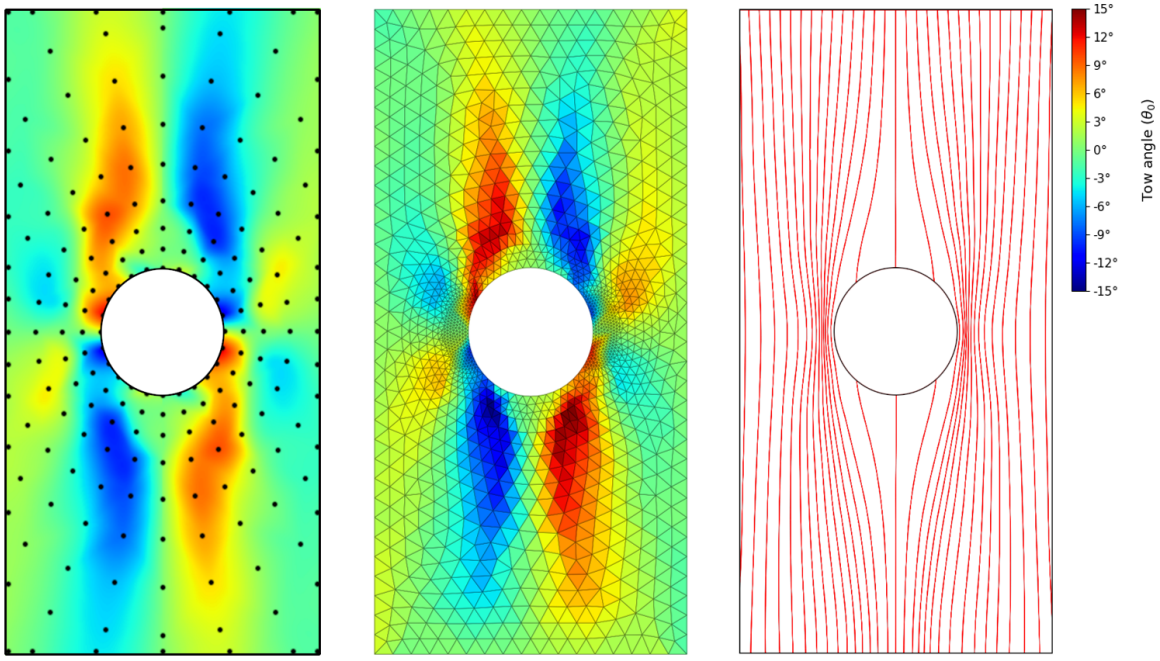

(a) B-spline surface (b) Element fiber angles (c) Tow paths

Figure 4.3.4: Optimization result for the reference orientation field θ_0.

The optimized tow angle distribution for the main tow pattern (θ_0) is depicted in Fig. 4.3.4. Several observations can be made: firstly, the fiber orientations at the boundary of the cutout align with the vertical axis, i.e., the primary loading direction. Secondly, tow courses near the central axis of the plate diverge outward. These results indicate that the loads are being transferred away from the cutout, towards the stiffer regions along the sides of the plate. Fig. 4.3.5 shows the three offset tow patterns.

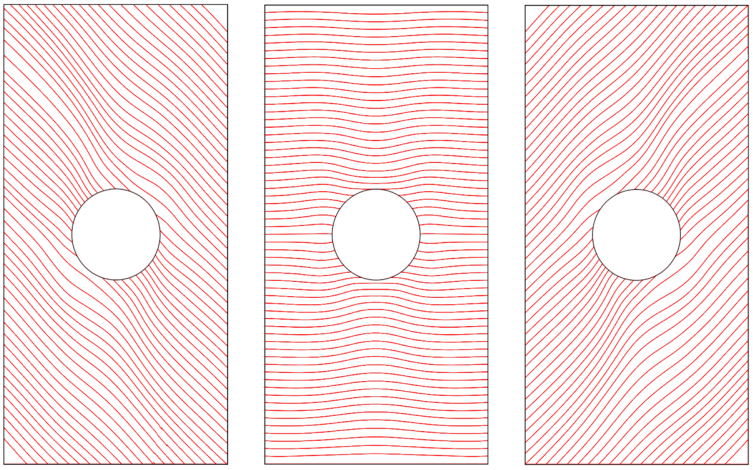

Figure 4.3.5: Tow paths for the $\theta_0 + 45°$, $\theta_0 + 90°$ and $\theta_0 - 45°$ plies.

The material distribution is shown in Fig. 4.3.6, showing similar characteristics to the VS design case. The main tow pattern θ_0 has taken on the role of the 0° ply, comprising the majority of the material. Compared to the VS design, this contains an even greater fraction of the total material (98.9%) and has a more even spatial distribution of thickness, as observed from the lower maximum values. This could be explained by the steered fibers in the θ_0 ply partially taking over the role of the ±45° plies, which are much less present in the VAT design.

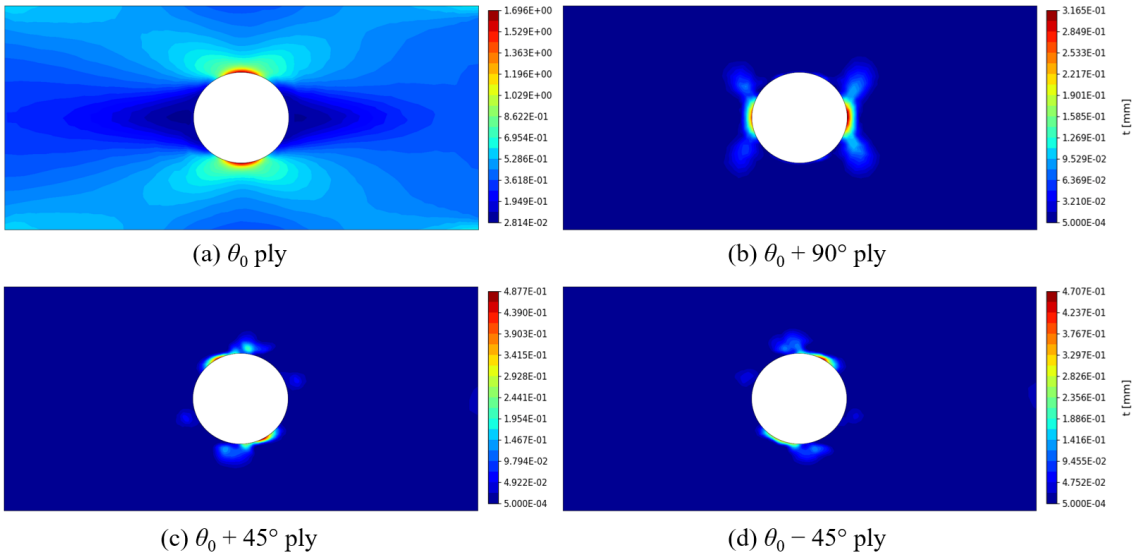

(a) θ_0 ply (b) $\theta_0 + 90°$ ply

(c) $\theta_0 + 45°$ ply (d) $\theta_0 - 45°$ ply

Figure 4.3.6: Ply thickness distribution (VAT).

4.3.2 Phase II

The thickness variation resulting from the varying streamline density is estimated using the finite volume method from Section 4.2.5. The thickness distribution is depicted in Fig. 4.3.7.

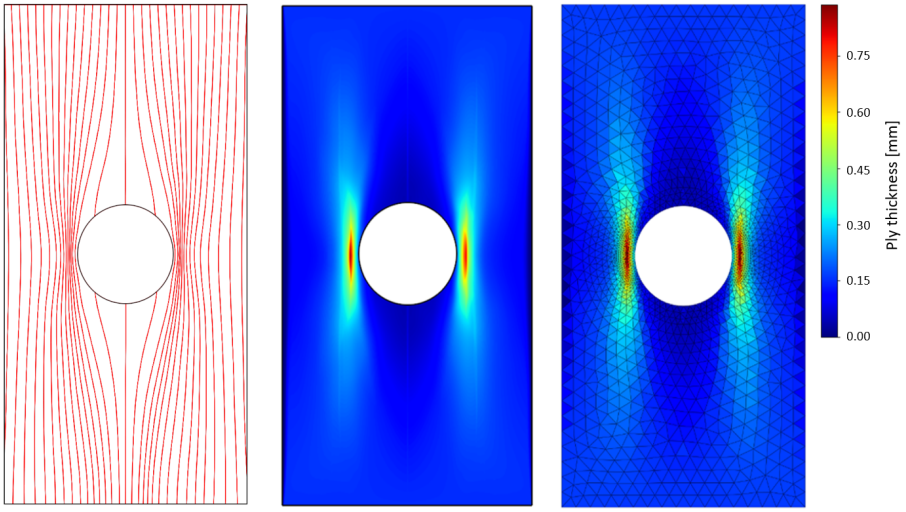

Figure 4.3.7: Thickness estimation for the θ_0 ply of the VAT design.

Defining the four level-sets at 2%, 10%, 20%, and 30% of the maximum thickness of each super-ply was found to yield ply shapes that are representative of the free-size material distribution. Some manual post-processing is done to improve manufacturability, such as removing disconnected patches and jagged edges resulting from the FE discretization. The ply shapes for the VS and VAT designs are shown in Fig. 4.3.9 and Fig. 4.3.10, respectively.

Due to size optimization being far less computationally intensive than the free-size stage, a lower objective tolerance (0.10%) is used. Fig. 4.3.8 shows the convergence for the size optimization step. The optimization results are presented in Table 4.3.5 for the VS design, and Table 4.3.6 for the VAT design, with the final designs in the rightmost column.

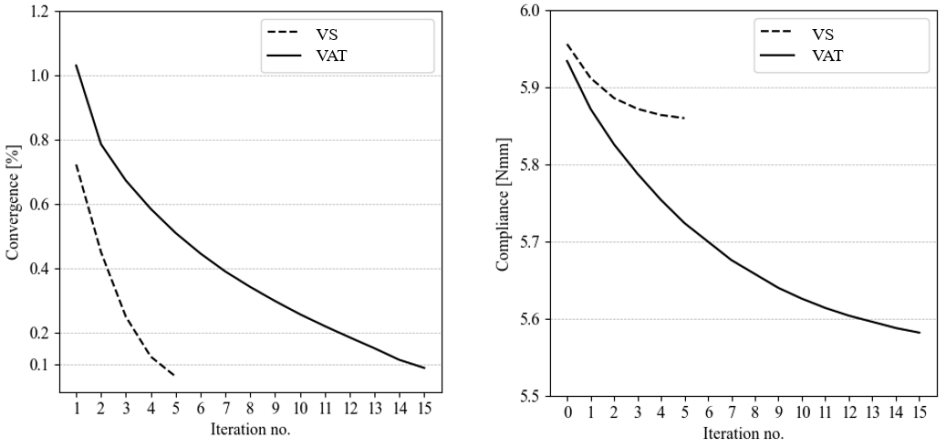

Figure 4.3.8: Phase II iteration progress. Left: convergence. Right: compliance.

After rounding the optimized ply thicknesses to the nearest manufacturable value, both designs experienced a small net increase in mass (8.01% for the VS design, 3.70% for VAT). Compared to the "ideal" material distributions defined in Phase I, the final manufacturable designs have a difference in specific compliance of +4.65% (VS) and +2.30% (VAT).

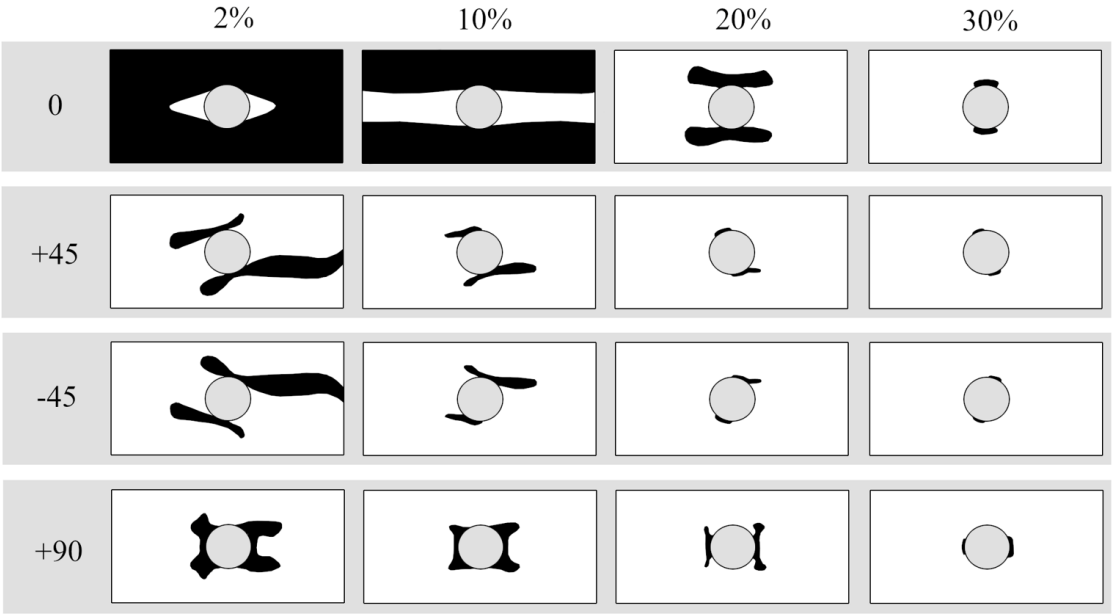

Figure 4.3.9: Ply shapes (VS).

Orientation	Ply level [%]	Thickness [mm] Initial	Optimized	Manufac.
0°	2	0.10	0.120	0.15
	10	0.20	0.280	0.30
	20	0.25	0.303	0.30
	30	0.25	0.384	0.45
45°	2	0.02	0.027	0
	10	0.08	0.085	0.15
	20	0.10	0.103	0.15
	30	0.10	0.126	0.15
−45°	2	0.02	0.031	0
	10	0.08	0.085	0.15
	20	0.10	0.950	0.15
	30	0.10	0.113	0.15
90°	2	0.01	0.006	0
	10	0.04	0.036	0
	20	0.05	0.062	0
	30	0.05	0.111	0.15
Compliance [Nmm]		9.134	5.860	5.532
Mass [g]		-	11.90	12.86

Table 4.3.5: Size optimization results (VS).

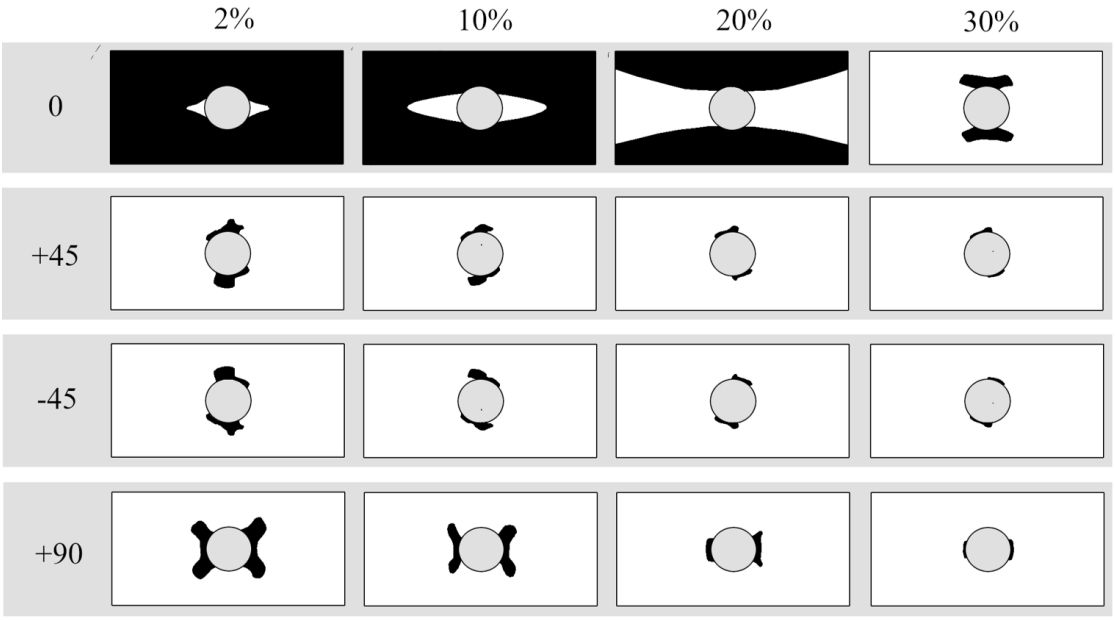

Figure 4.3.10: Ply shapes (VAT).

Orientation	Ply level [%]	Thickness [mm] Initial	Optimized	Manufac.
θ_0	2	0.05	0.095	0.15
	10	0.15	0.191	0.15
	20	0.20	0.145	0.15
	30	0.20	0.031	0
$\theta_0 + 45°$	2	0.01	0.001	0
	10	0.04	0.001	0
	20	0.05	0.001	0
	30	0.05	0.06	0
$\theta_0 - 45°$	2	0.01	0.001	0
	10	0.04	0.001	0
	20	0.05	0.001	0
	30	0.05	0.006	0
$\theta_0 + 90°$	2	0.01	0.001	0
	10	0.04	0.103	0.15
	20	0.05	0.042	0
	30	0.05	0.189	0.15
Compliance [Nmm]		6.384	5.582	5.386
Mass [g]		-	11.90	12.34

Table 4.3.6: Size optimization results (VAT).

4.3.3 Final Designs

The stiffness performance of the final designs is summarized in Table 5.2.1, calculated as the average displacement of the right-hand plate boundary. This predicts an improvement for VAT of 77.4% compared to QI and 10.9% compared to VS with regard to specific stiffness.

Case	Mass	Specific compliance	Specific stiffness	Improvement[1]	Improvement[2]
	[g]	[Nm·g]	[kN/mm·g]		
QI	11.90	2.171	0.736	-	-
VS	12.86	0.915	1.180	+60.0%	-
VAT	12.34	0.820	1.307	+77.4%	+10.9%

Table 4.3.7: Stiffness/weight performance of the final designs, [1]: Compared to QI laminate, [2]: Compared to VS laminate.

The impact of optimization on the elastic characteristics of the plate is illustrated in Fig. 4.3.11. The concentration of strain adjacent to the cutout has been alleviated for the VS and VAT designs, and replaced by a largely even distribution across the plate. These strain distributions appear more irregular compared to QI, caused by the discrete thickness changes (ply-drops) within the plates. The displacement plots reveal an increased bias of stiffness towards the plate's upper and lower bands, with larger displacements close to the centerline.

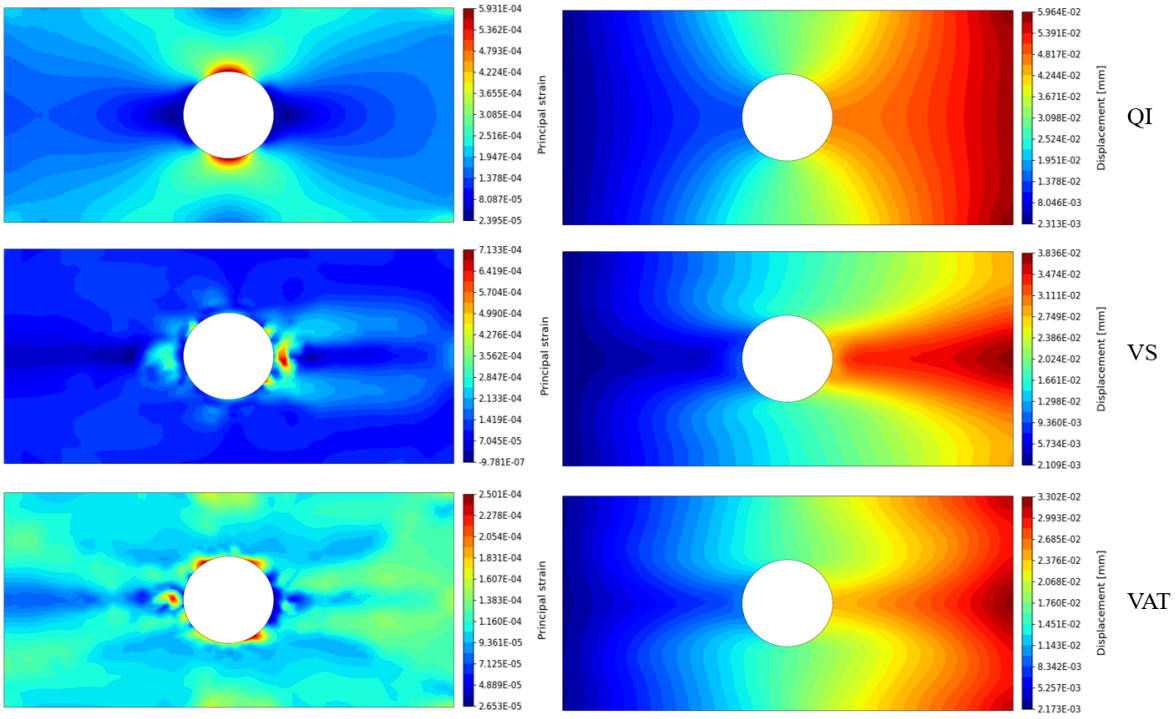

Figure 4.3.11: Elastic response of the final designs for a load of 500 N. Left: principal strain. Right: displacement.

Predicted strength is presented in Table 4.3.8. Similarly to stiffness, the predicted specific strength of the compliance-optimal VAT design is significantly higher than the QI and VS cases, this time by 249% and 26.9%, respectively. The location at which the allowable failure index is exceeded is shown in Fig. 4.3.12. All designs are predicted to fail in the same area near the cutout boundary, in the fiber layer oriented parallel to the loading direction.

Case	Failure load	Failure ply	Specific strength
	[kN]		[kN/g]
QI	8.50	0°	0.714
VS	25.3	0°	1.962
VAT	30.8	θ_0	2.491

Table 4.3.8: First-ply failure predictions using the Tsai-Hill criterion.

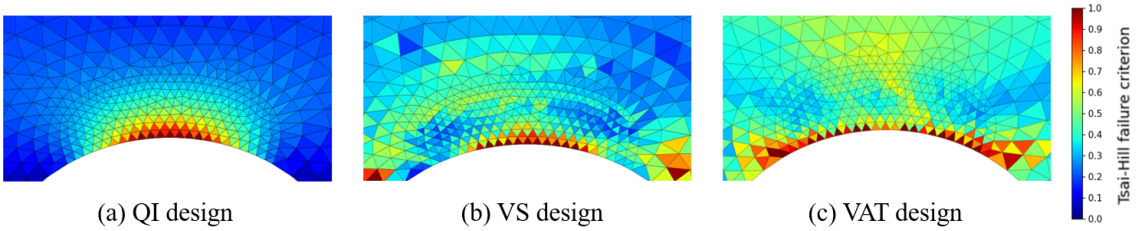

(a) QI design (b) VS design (c) VAT design

Figure 4.3.12: Tsai-Hill failure index at the maximum load of each design.

CHAPTER

FIVE

EXPERIMENTAL VALIDATION

5.1 Method

5.1.1 Test Specimen Design

The main consideration when designing the test specimens is to facilitate the introduction of axial load through shear forces along the specimen surfaces. This requires some special consideration when testing predominantly unidirectional composite materials. If the load is applied unevenly, such specimens may experience transverse or shear failure, even when these induced stresses are small relative to the applied longitudinal stress. Furthermore, excessive clamping force can cause matrix cracking, which degrades the mechanical properties of the material.

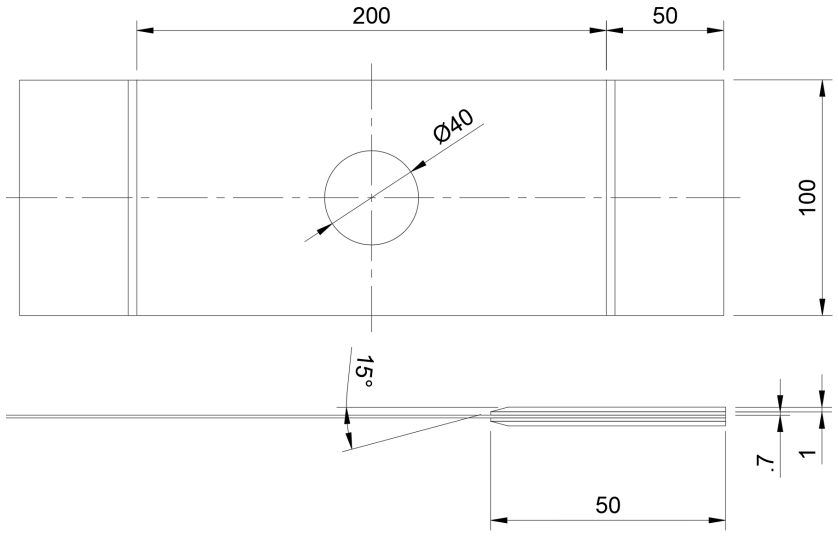

Figure 5.1.1: Schematic of test specimen.

To mitigate this, specimen tabs are used for load transfer. Tabs allow the use of serrated grip surfaces and accordingly low grip pressures, thus preventing gripping-induced damage to the specimen. This also means that the specimen ends have an increased cross-sectional area compared to the central gage section, which serves to prevent premature failure near the grips due to the additional stresses introduced in this region. However, because of this thickness variation, the tabs themselves

can result in stress concentrations, particularly at tab terminations. To prevent this, the tabs are tapered at the gage section ends.

The tabbing material must have the required strength to sustain the applied load, while being suitable for bonding to a composite surface. For these reasons, tabs are manufactured from a carbon/epoxy composite, using a 210 g woven prepreg material with the same resin system as the test specimens. Following the FAA tabbing guide for composite specimens [95], these have a length of 50 mm, with a taper angle of 15°. A 4-layer quasi-isotropic layup $[0/45]_S$ is used, resulting in a thickness of 1.0 mm. The design is illustrated in Fig. 5.1.1.

The tabs are joined by means of *secondary bonding*, referring to the adhesive bonding of two or more pre-cured composite parts. A MMA (methyl methacrylate) adhesive is selected due to its high bond strength and ease of application. In addition, this adhesive is suitable for use with a thicker bond line, which has been found to significantly reduce tab termination stress concentrations [95]. The selected bond line thickness is 0.7 mm.

5.1.2 Manufacturing

Images documenting the manufacturing process are found in Appendix C. The tooling surface for the layup is a glass plate prepared with a chemical release agent. To provide a reference for fiber placement, the part boundary is marked on the tool using flash tape. This leaves an indent on the part surface, serving as a guide for trimming operations after curing.

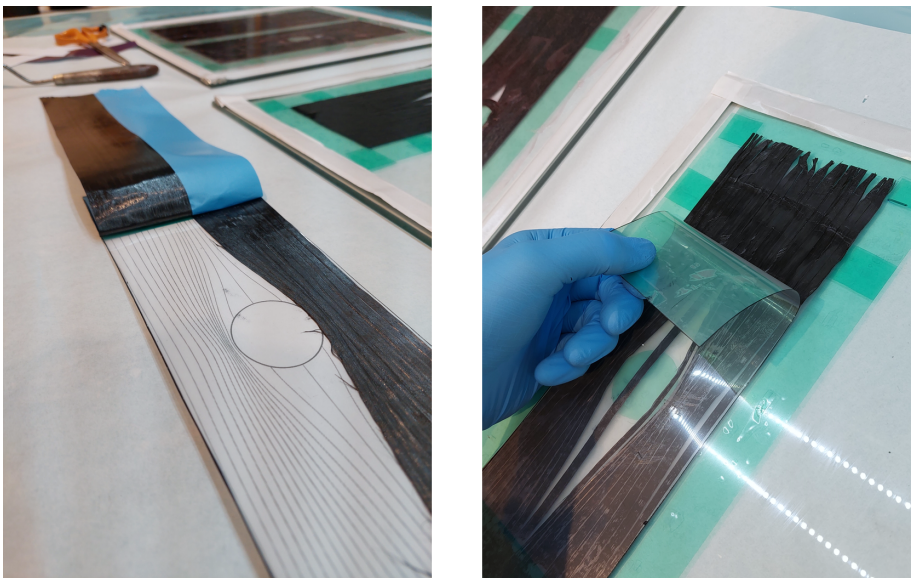

Figure 5.1.2: Manual placement of fibers using a stencil.

To ensure precision during the layup step, cutting- and placement stencils for each ply are created. Once cut to the correct shape, plies are positioned on a transparent mylar sheet and subsequently transferred to the tool surface. For the VAT design, the fiber reinforcement is divided into 5 mm strips which are manually steered to fit the tow paths defined by the optimization.

Fig. 5.1.3 shows the layers comprising the completed layup. The laminate is de-bulked for 20 minutes, which compacts the plies and removes trapped air by

pulling a vacuum over a period of time. This reduces void nucleation sites, which adversely impact the mechanical properties of the laminate. The specimens are then placed in an oven under a vacuum pressure of 0.90 bar for curing. The cure cycle consists of heating to 90° C for 8 hours, with a ramp rate of 3° C per minute.

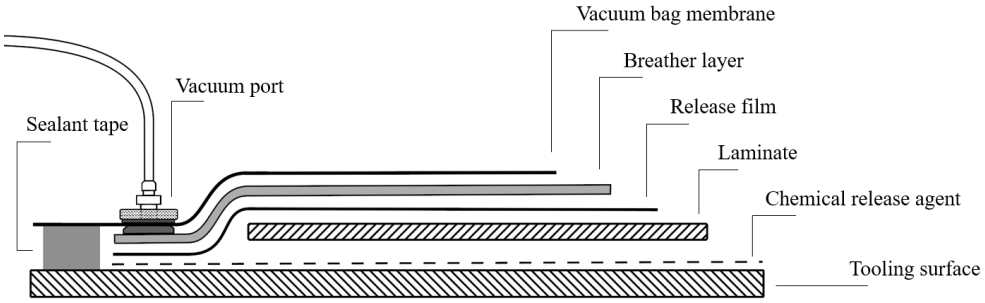

Figure 5.1.3: Layup used for test specimens.

After de-moulding the cured parts, the tabs are ground to the desired taper angle and joined to the test specimens. The surfaces are prepared through abrasion to raise the surface-free energy of the substrates, facilitating molecular cross-linking. Prior to bonding, impurities such as dust and residual release agent are removed using a solvent, and spacers are placed to control bond line thickness. Once the adhesive is cured, the specimens are trimmed to their final shape.

5.1.3 Test Setup and Data Acquisition

The static tensile tests are performed using an Instron 8854 machine. The VIC-2D-v6 system is used to analyze the results using digital image correlation (DIC) (Fig. 5.1.5).

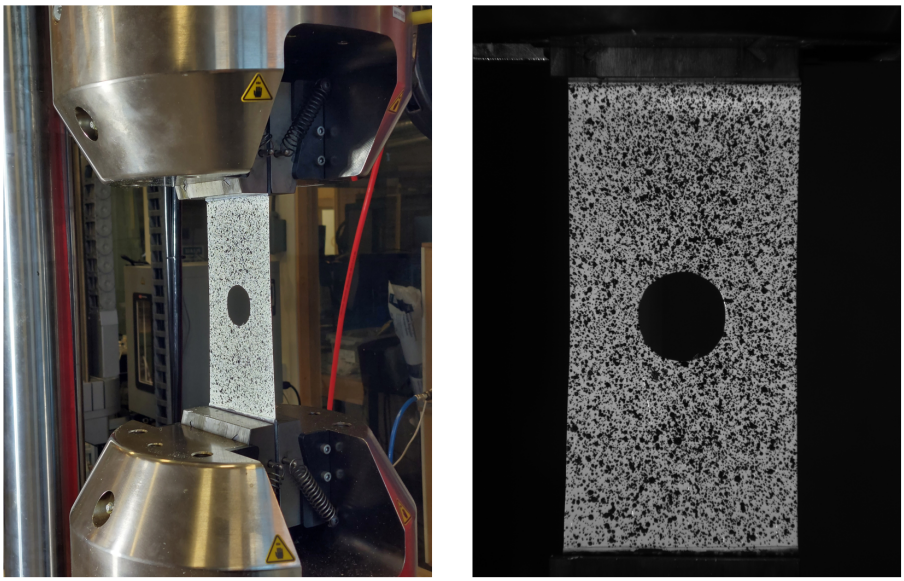

Figure 5.1.4: Test specimens prepared with a speckle pattern and positioned in the machine.

The specimens are fastened using 100 mm wide serrated wedge grips, and tested to an extension of 5mm at a rate of 2 mm/min. During this operation, the testing machine measures load and displacement at a rate of 10Hz, while the 4-megapixel DIC camera simultaneously records the test at the same frequency. The specimens are prepared with a speckle pattern (Fig. 5.1.4) which is tracked by the VIC-2D software. This analysis uses the "virtual extensometer" tool to provide a backup measurement of displacement as verification of the machine data. Additionally, it enables the characterization of the displacement and strain distribution across the plate.

the 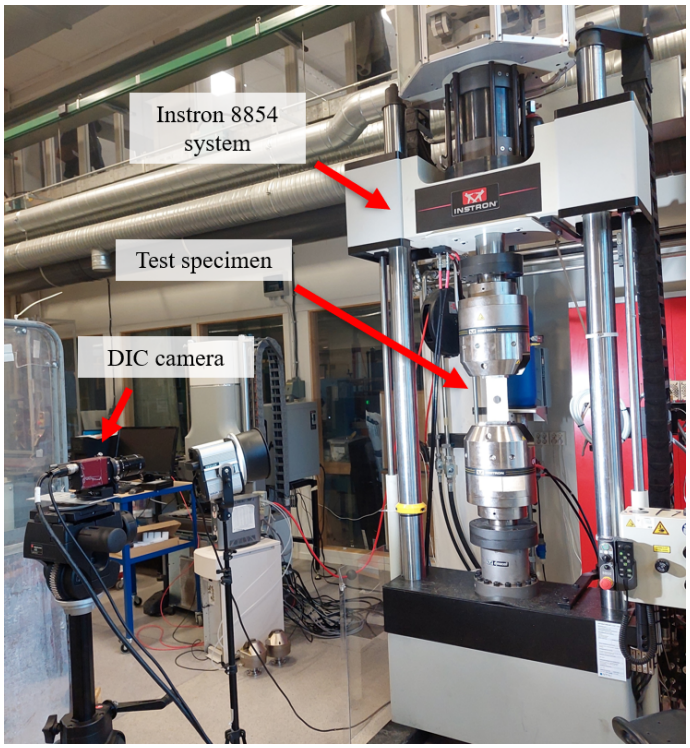

Figure 5.1.5: Equipment used for the test.

5.2 Experimental Results

The load/displacement results from the tensile test (machine measurements) are plotted together with the numerical predictions in Fig. 5.2.1. The synchronized sampling rate of the DIC and test machine allows for direct comparison of the displacement data points, visualized in Appendix D. This reveals the deviation between these to be insignificant (1.03% on average). The point of first-ply failure is discerned from the DIC footage and is indicated on each curve with a cross.

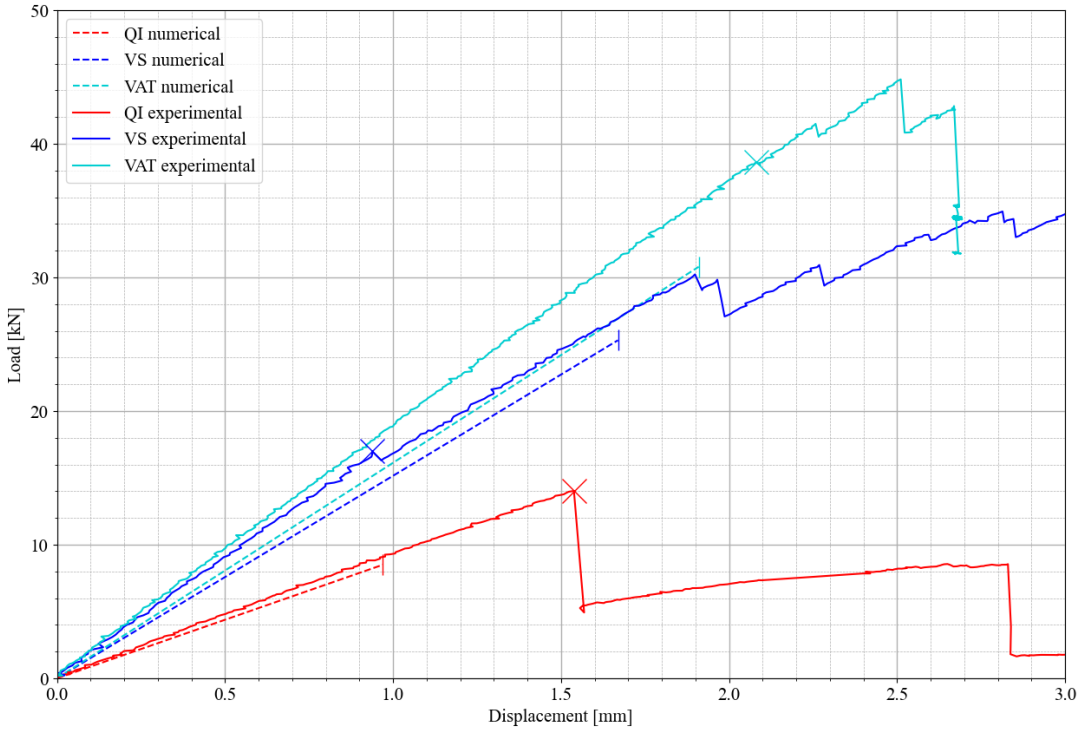

Figure 5.2.1: Comparison of experimental and numerical performance.

After testing, the specimen tabs are removed, and the test sections are weighed with an accuracy of ±0.01g. Stiffness is obtained by interpolation of the pre-failure region of the load/displacement curves. The results are summarized in Table 5.2.1, showing an improvement for VAT of 120% compared to QI and 16.9% compared to VS with regard to specific stiffness.

Case	Mass	Stiffness	Specific stiffness	Improvement[1]	Improvement[2]
	[g]	[kN/mm]	[kN/mm·g]		
QI	12.42	9.259	0.745	-	-
VS	12.97	18.15	1.399	+87.7%	-
VAT	12.01	19.65	1.636	+120%	+16.9%

Table 5.2.1: Experimental stiffness/weight performance, [1]: Compared to QI laminate, [2]: Compared to VS lamiante.

The measured principal strain and displacement fields (Fig. 5.2.2) allow for a qualitative comparison with the predicted behavior. For displacement, overall similar features can be observed, with higher displacement towards the center of the plate for VS and VAT compared to QI. Although the accuracy of the measured principal engineering strain appears to be limited, some basic characteristics can be recognized. Like the predictions, these show larger strain concentrations adjacent to the cutout for the QI design, and a more even distribution for the VS and VAT designs.

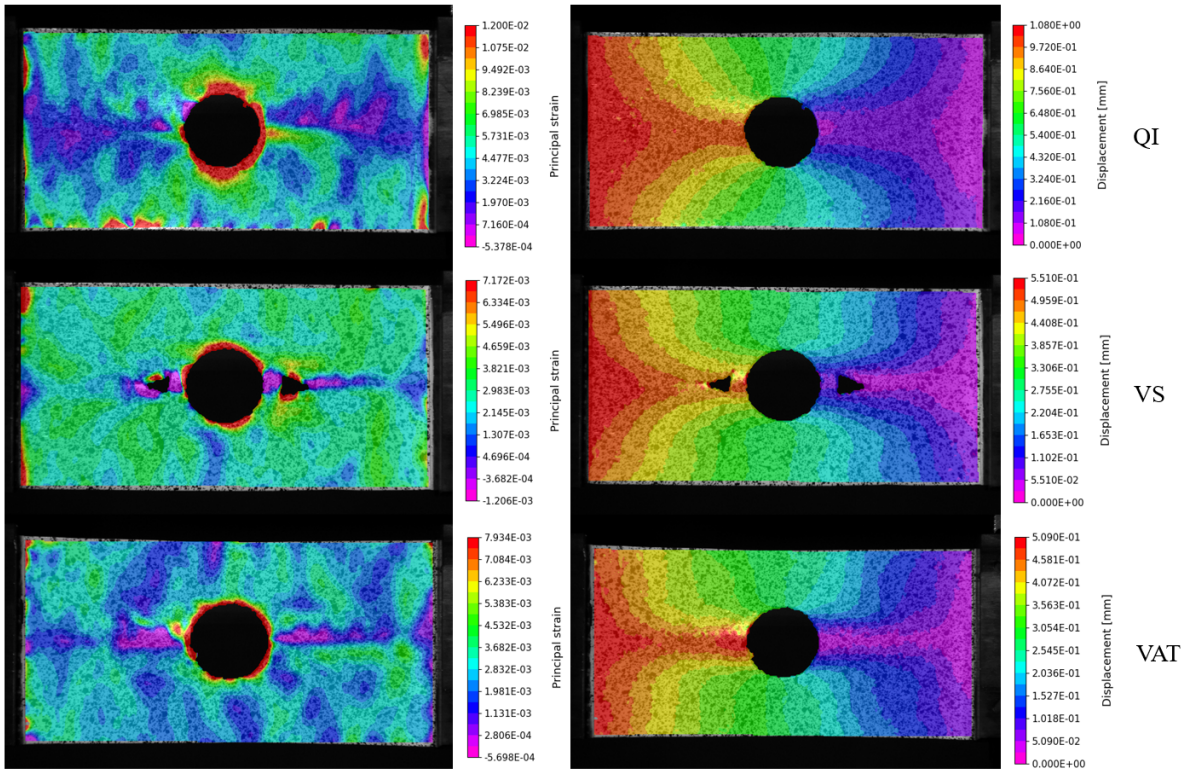

Figure 5.2.2: Measured elastic response at 10 kN. Left: principal engineering strain. Right: displacement.

The measured strength is summarized in Table 5.2.2. The modes of failure are indicated in Fig. 5.2.3, showing the specimens at the moment of first-ply failure. This shows fiber failure of the 0° ply of the QI design, with fracture occurring along an axis of 45°. Both VS and VAT specimens experience matrix fracture along the 0° fiber direction, with VS simultaneously suffering delamination adjacent to the cutout boundary. These observations provide valuable insight into the stress state within the structures, as will be discussed in the following chapter.

Case	Specific strength [kN/g]	Failure load [kN]	Failure ply
QI	1.129	14.02	0°
VS	1.271	16.49	0°
VAT	3.206	38.50	θ_0

Table 5.2.2: First-ply failure obtained from testing.

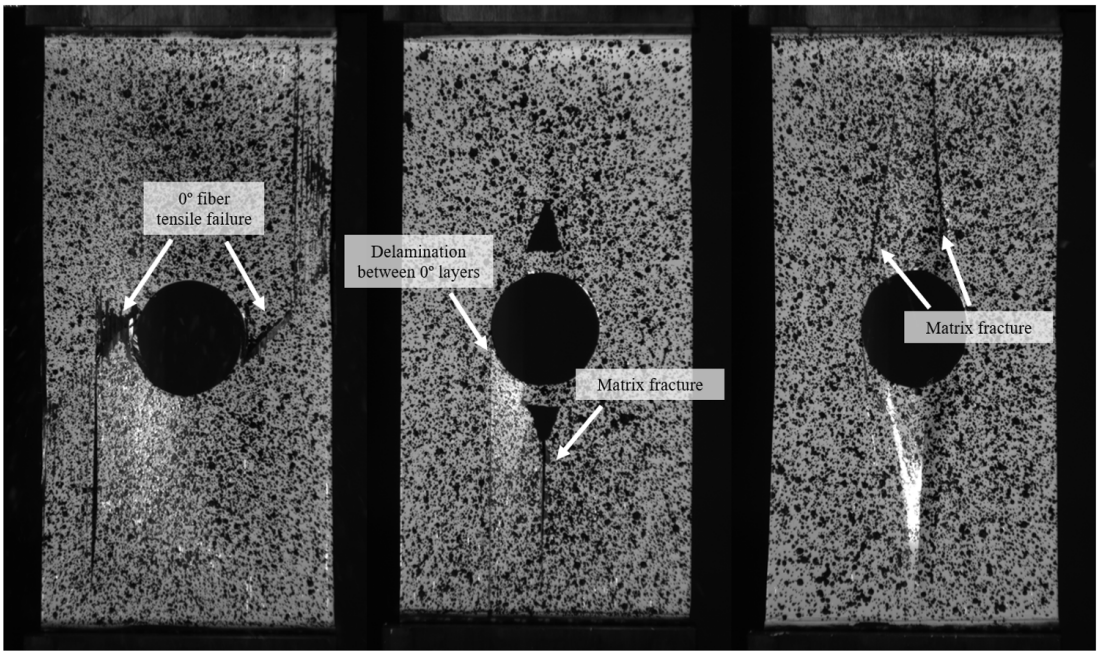

(a) QI (b) VS (c) VAT

Figure 5.2.3: First-ply failure modes of the test specimens.

5.2.1 Sources of Error

The use of these results in an assessment of the numerical predictions necessitates a reflection on the uncertainties associated with the methodology.

The manual manufacturing process used represents the first source of errors. Manual cutting and placement of fibers may introduce deviations from the design, such as fiber angles and ply boundaries. This factor is likely insignificant due to the extensive use of guides and stencils during the layup. As established in Section 2.2.2, porosity is a crucial parameter for quality assurance in composite manufacturing due to its detrimental impact on performance. Despite the de-bulking step, some porosity was observed on the specimen surfaces. The severity is assessed as being limited, with the overall number of voids being low. Furthermore, the trimming step could impact performance if defects such as notches are introduced, which could act as stress risers. On inspection, no such defects were observed.

In addition, the results are subject to measurement errors. First, the measurement accuracy depends on the alignment of the specimen with the machine axis, and the alignment of the DIC camera with the specimen. Second, some out-of-plane buckling was observed along the midplane of the plates during testing, which deteriorated measurement accuracy in these areas. Because this effect is highly localized, it did not impact the measurement of total displacement, which is based on reference points at opposite ends of the plate. It should also be considered that all measurements are subject to instrumental errors. This is evident from the signal noise in the displacement data, which however has a negligible amplitude compared to the trends being studied.

CHAPTER

SIX

DISCUSSION

6.1 Summary of Results

The results of the design study are summarized in Fig. 6.1.1. This discussion addresses the aim of this thesis, namely to utilize experimental results to evaluate the accuracy of the numerical predictions, and by extension, the validity of the design approach itself.

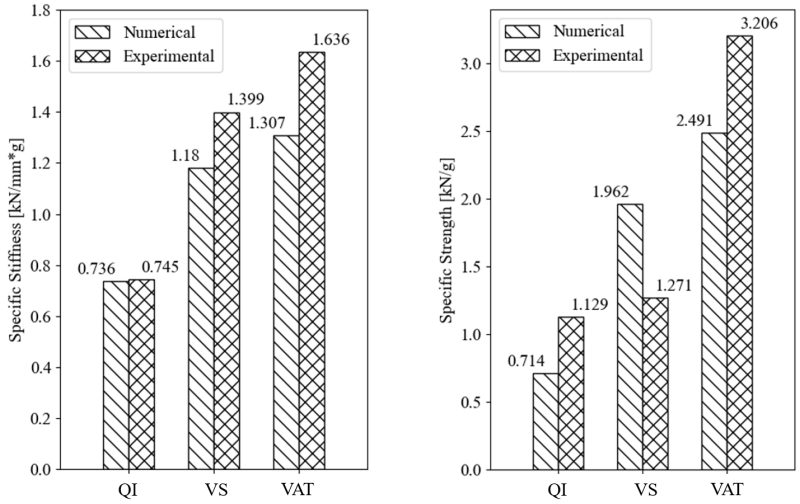

Figure 6.1.1: Summary of design study results. Left: specific stiffness. Right: specific strength.

To provide a framework for this discussion, the three main components of the numerical solution are considered separately. Accordingly, the validity of the results depends on the fulfillment of the following three assumptions:

1. The physical system is modeled accurately.
2. The optimization algorithm accurately locates the optimum design.
3. The optimization problem formulation ensures the practical feasibility of the part.

These assumptions are evaluated in sections 6.2, 6.3, and 6.4, respectively.

6.2 FE-Model Accuracy

6.2.1 Elastic Response

When comparing the relative specific stiffness of the design cases, the measured behavior shows an overall good correspondence with the numerical predictions. For the stiffness advantage of VAT compared to VS, one of the most critical predictions with regard to the objective, the numerical value (10.9%) is close to the experimental value (16.9%). This similarity between predicted and measured elastic response is confirmed by the comparison of the strain and displacement fields in Section 5.2.

The simulated results are, on average, 14.9% under-stiff compared to the measurements. Since this applies to all designs, it is likely to be caused by a systematic error which could have its origin in a number of factors. One possible cause is the use of low-order elements to discretize the domain. Another explanation is inaccuracies in the material data, such as modulus or consolidated ply thickness. These values are sensitive to processing parameters such as curing temperature, pressure, and whether a post-curing stage is performed. According to the manufacturer, the material was characterized using autoclave curing, representing a major difference from the process used in this study. Finally, manufacturing and measurement inaccuracies, as discussed in Section 5.2.1, are another plausible cause for systematic bias.

In the context of contemporary research, these findings are within expectation. The anisotropic elastic behavior of composite materials is well-understood, and thus, the tools currently used are widely accepted to provide satisfactory analytical predictions [96]. More specifically, the results confirm that the structures satisfy the conditions for modeling elastic response using ESL theories such as CLT. Moreover, they indicate that the prediction of gaps and overlaps (Section 4.2.5) was successful, as errors at this stage would have greatly impacted the stiffness of the VAT design. This is also an expected result in the context of prior studies, such as the paper by Vertonghen and Castro [4] comparing the elastic response of the smeared thickness approximation to the "exact" discrete thickness profile. This showed good agreement between the two methods, provided that the tow width is sufficiently small relative to the plate dimensions.

6.2.2 Stress Response

With regard to strength, more significant differences between prediction and measurement were found, summarized in Table 6.2.1.

Case	Difference [%]	Failure mode
QI	+58.1%	Fiber failure (In-plane)
VS	−35.2%	Delamination (Out-of-plane)
VAT	+28.7%	Matrix failure (In-plane)

Table 6.2.1: Comparison of predicted and measured specific strength.

The VS design represents an outlier, in that it fails much before the predicted load (35.2%) by an out-of-plane failure mode. Such a failure mode is necessarily caused by interlaminar (out-of-plane) stresses in the material [28], i.e. σ_z, τ_{zx} and τ_{zy}. Given that the delamination occurred at the cutout boundary, a likely explanation is the *free-edge effect*. This is a well-known phenomenon where out-of-plane stresses arise near free edges due to the mismatch of elastic properties between layers. This results in a three-dimensional stress state, even if the laminates are only subjected to in-plane loading. For plates with holes, this effect is accentuated by the stress concentrations around the edge of the cutout [97]. Another possible explanation is ply drop-offs, several of which are present near the area of delamination. These act as stress risers, introducing localized concentrations of out-of-plane stresses due to the abrupt changes in laminate thickness. Hence, they are known to become initiation points for delamination if they become too severe, i.e., if too many plies are dropped within too short of a distance [56].

These results highlight two significant shortcomings in the method for modeling stresses. Firstly, recalling Section 2.1.3, CLT assumes out-of-plane stresses to be negligible. Consequently, it is outside the scope of this laminate theory to capture the stress fields resulting from free-edge effects or ply drop-offs. Secondly, in-plane analysis using CLT applies strain uniformly to all plies within the laminate, making the stress response insensitive to stacking sequence. The drawback of this can be illustrated for the QI specimen, which fractured along an axis of 45°, which is identical to the orientation of the subsequent ply in the laminate. This demonstrates a clear relationship between stacking sequence and failure mode, even when failure occurs in-plane. This relationship has previously been demonstrated in greater detail by Daniel et al. [98], who tested boron/epoxy panels with circular holes under tension. Numerous studies have also found failure induced by ply drop-offs to be a function of stacking sequence [99].

The use of FEA-approaches which account for these effects is a development already taking place within the field of VAT composite design. The limitations of CLT and FSDT have led several researchers to adopt higher-order shear deformation theories (HSDT) [10], which are plate theories that assume non-linear stress variation through the thickness. By treating each ply as an independent plate and constraining the displacement compatibility at each interface, a so-called layer-wise (LW) model capable of capturing interlaminar effects is obtained [28]. Viglietti et al. [100] performed analysis of VAT structures using such an LW approach and reported more accurate predictions, although at a higher computational cost. Alternatively, an analysis based on three-dimensional finite elements may be employed. This has been investigated by Zhao et al. [101] and Chaudhuri [102], who performed three-dimensional finite element analyses on laminates with circular holes.

It must also be taken into account that this study considers a scaled-down analogy of a larger structure. Since the linear in-plane responses considered in the numerical investigation are either independent of- or proportionally related to scale, a comparison between them (i.e., relative strength and stiffness) can be generalized as being valid for any size scale. However, the apparent sensitivity of failure to stacking sequence design does not necessarily follow this trend. These stresses depend on the number and thickness of plies relative to the plate dimensions, which are not necessarily a linear function of scale. Thus, this aspect

represents an important limitation in generalizing the experimental findings to a full-scale structure.

6.2.3 Failure Analysis

Although the QI and VAT specimens experienced in-plane ply failure, and thus are within the scope of the laminate theory, the measured strength was significantly higher than predicted, on average 43.4%. This result mirrors the findings of several other papers on tow-steered plates with cutouts, which crucially tend to define failure on a first-ply basis, as is done in this study. For instance, Khani et al. [24] measured an average strength increase of 72.4% compared to numerical results.

An explanation for why first-ply failure criteria lead to conservative predictions of open-hole strength is offered by the literature on the testing and certification of notched composite structures [96]. Returning to the Tsai-Hill failure index plot in Fig. 4.3.12, failure is predicted to occur only in a few elements directly at the hole boundary for all three cases, indicating a highly localized stress concentration. By applying a first-ply failure criterion, this local failure of the material suffices to consider the entire laminate as failed, effectively treating the fracture behavior of the material as brittle. In reality, however, composites exhibit a quasi-brittle behavior (Fig. 6.2.1). When approaching failure, various matrix and fiber damage effects (such as ply splitting, weak fiber failures, and delaminations) occur at the maximum stress locations, reducing the stiffness in these areas. This gradual unloading after the onset of damage can enhance residual strength by effectively reducing the severity of stress concentrations [97].

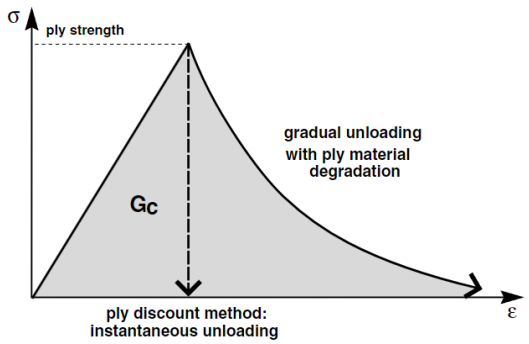

Figure 6.2.1: Idealised quasi-brittle damage behavior in composite materials [103].

Multiple improvements to the analysis have been proposed to deal with this, albeit beyond the literature on tow-steered composites. In the context of commercial aircraft structures, the strength of notched laminates is commonly determined using the point stress theory (or Whitney–Nuismer criterion) [96]. This theory proposes to evaluate stress at a distance d_0 from the edge of the hole, with failure occurring when the stress at this distance surpasses the unnotched-laminate strength. However, this analysis method is restricted to near-quasi-isotropic laminates and is therefore not applicable to VAT structures.

Alternatively, non-linear constitutive models for progressive failure analysis have been used to model the failure of plates with cutouts. In these methods, the stiffness matrix of a failed element is modified according to a material degradation

model, simulating the gradual unloading after the onset of damage. The use of such models for analyzing tow-steered structures with cutouts has been proposed by Lopes et al. [103], although this has thus far remained limited.

6.3 Solution Optimality

In solving for the compliance-optimal design, the optimizer considers only the elastic responses of the structure. Therefore, based on the preceding discussion, it can be concluded that the underlying FE model does not introduce significant inaccuracies to the optimization procedure.

In addition to this, some uncertainties with regard to optimality can be identified based on the nature of the solution. As with any structural optimization problem, the computational resources for solution are finite, meaning the dimensionality of the problem controls a crucial trade-off: between the accuracy at which functions and sensitivities can be evaluated, and the number of iterations that can be performed. This design study makes a number of simplifications that reduce this dimensionality at the cost of solution accuracy. For instance, as demonstrated by Brooks et al. [9], the optimal tow angle distribution greatly depends on the positioning and density of B-spline control points, as these are directly related to design flexibility. Similarly, the topology optimization scheme depends on manual selection of level-sets in order to define discrete ply shapes. Such simplifications can be avoided by increasing formulation complexity, which conversely makes convergence more difficult to guarantee.

Moreover, the optimization of fiber orientation using ply angles as DVs has been shown to be non-convex. This makes the solution sensitive to the initial fiber configuration when the problem is solved with gradient-based methods. Although non-convexity could be dealt with using gradient-free methods, this has been deemed infeasible due to the large number of DVs. Another possible improvement is offered by lamination parameter design, as introduced in Section 3.2.2. When using lamination parameters as DVs, the feasible region has been proven to be convex in numerous investigations [21]. The implications of this were demonstrated for compliance minimization problems by Setoodeh et al. [104], showing that this method could generate superior results to fiber angle DVs.

6.4 Design Feasibility

Finally, the results of the design study must be evaluated in the context of their compliance with the feasibility requirements introduced in Section 2.2.

First, with regard to manufacturability, the B-spline parameterization successfully generated tow courses which were smooth and continuous. Additionally, the decision to not enforce a turning radius constraint proved to be correct. Based on the streamline plots, $r_{\min}$ for the unconstrained design is estimated to be in the order of 80 mm. This is well within the limit for the AFP process, when corrected for an estimated scale of 1:20 compared to a real wing access hole, of approximately 25mm. On the other hand, a potential manufacturability concern is the high degree of overlap, exceeding 6 layers at the maximum point. However,

due to the absence of concrete guidelines for this aspect in the literature, it cannot be concluded with certainty to what extent this would inhibit manufacturing.

On the contrary, several favorable properties are observed as a consequence of course overlaps. As the Phase I optimization results show (Fig. 4.3.2 and 4.3.6), the optimal material distribution for the VAT and VS designs are close to identical. However, because the tow course overlaps largely coincided with the optimal thickness distribution, the number of discrete plies needed to capture this optimal distribution is three times lower for VAT than for VS (5 and 15 plies, respectively). Furthermore, it can be hypothesized that the overlap method contributes to increasing the delamination resistance of the VAT design. By building up thickness through converging tow courses, the steep thickness gradient of the optimal material distribution is achieved without the need for a large number of tow-drops, mitigating the interlaminar stresses that would otherwise arise through these features. This could be an explanation for why the VAT design did not fail through delamination, despite being subjected to larger loads and having a similar thickness profile to the VS design. This raises the question of whether this correspondence between course overlaps and optimal thickness is a unique case for the present design problem, or an inherent tendency of topology-optimized VAT structures.

The second concern for feasibility regards the airworthiness requirements from Section 2.2.5. The discussion on certifiability led to the use of a reference tow orientation to limit the number of laminate families in the VAT structure. Although this restriction inevitably inhibits performance, the results show that this reduced design space still allows for a significant margin of improvement over VS. On the other hand, a challenge for certifiability is that the optimized designs have the vast majority of the fibers oriented in a single direction, making their failure matrix-dominated in both cases. For certification purposes, fiber-dominated laminates are typically preferred for use on commercial transports [51]. Since the variability associated with matrix-dominated failures tends to be high compared to fiber-dominated failures, the B-basis allowables, which ultimately define the "permitted" strength of the structure, are much higher in the latter case.

This aspect highlights the importance of complying with the laminate design rules from Section 2.2.6, which, among others, serve to prevent cases where anisotropy becomes too biased in a single direction. Furthermore, since these guidelines address the delamination risk caused by tow-drops, they are often used in practice as a means of circumventing the more complicated three-dimensional or layer-wise analysis proposed in Section 6.2.2 [56]. This conclusion reflects the direction taken by more recent studies in the field of VAT design. Most notably, the integration of design rules into the optimization procedure has been undertaken in the works of Brooks [61] and Dillinger [105], who both studied the design of wing structures.

CHAPTER

SEVEN

CONCLUSIONS

7.1 Conclusions

This thesis aimed to numerically quantify the performance benefit of tow-steering for a composite wing skin section, and to validate these results through experimental testing.

To ensure the relevance of the study with regard to this objective, design constraints were defined based on the AFP manufacturing process and aviation industry standards. The second objective in ensuring relevance was to align the numerical solution with the contemporary literature, and an approach for structural analysis and optimization was established accordingly. However, because some of the identified constraints were found to be underexplored in this literature, decisions were necessitated with regard to which to enforce, both to ensure compliance with the second objective, and to confine the scope of the work.

Effectively navigating these challenges, the implemented method was successfully used to generate a solution to the design problem which satisfied most of the constraints. This confirmed the hypothesis regarding the superior performance of the VAT design, with stiffness increasing by 11% and strength by 27% compared to VS. Yet, this investigation illuminated certain limitations inherent in current design techniques, arising from the general non-convexity and high dimensionality of the design problem under investigation.

In the subsequent experimental phase, manufactured designs were tested, and their performance was characterized through DIC analysis. While acknowledging the potential limitations posed by the manufacturing process, a review of the induced errors suggested a minor impact on the overall outcomes. Drawing conclusions in alignment with the thesis aim, it becomes evident that the predicted elastic response, and therefore also the associated sensitivities used for stiffness-optimal design, align well with experimental observations. However, limitations in failure prediction were highlighted, attributed to the sensitivity of first-ply failure to factors outside the scope of the numerical model. These were identified as out-of-plane stresses arising near ply-drops and free edges, and the quasi-brittle fracture behavior of the material. To address these challenges, this thesis proposes improvements to the structural analysis and advocates for a more stringent set of design constraints.

As one of few works that examines simultaneous topology and tow path opti-

mization both numerically and experimentally, this thesis contributes a distinctive perspective to the existing body of knowledge. Among the experimental findings, several converge with those of prior studies, reinforcing their broader implications as a validation of contemporary methods. Importantly, it also confirms a significant enhancement of performance within the specific design cases under study, shedding light on the transformative potential of VAT composites in the context of wing design.

7.2 Future Work

With respect to the overarching goal of establishing the efficacy of tow-steering for commercial aviation, the results offer a strong indication of potential. However, the generalizability of these findings is constrained by the specific nature of the design study and the methods employed. To advance this goal further, several key points emerge from this study, outlining avenues for future research:

- This study has identified potential improvements to the FE model, aiming to bridge the gap between simulation and experimental results. Future studies should focus on implementing and validating these improvements through further studies on design, manufacturing, and testing.
- The literature review highlights a lack of concrete guidelines for certain design constraints and an absence of information on manufacturing costs relative to other technologies. Addressing these gaps requires dedicated manufacturing studies that quantify these design parameters, contributing to a more comprehensive understanding of tow-steering's practical feasibility.
- The issue of ensuring global optimality without prohibitive computational effort has been underscored. Future research should aim to establish a widely accepted solution that satisfies these requirements, building upon the insights gained from existing literature.
- Because studies tend to consider simple geometries, it is uncertain what additional challenges would arise in the transfer of these methods to the design of real-life structures. The culmination of the three above points in the analysis of a larger system, such as a complete wing structure, will eventually determine the true potential of tow-steering over conventional laminate design.

BIBLIOGRAPHY

[1] International Energy Agency. *Aviation*. URL: https://www.iea.org/energy-system/transport/aviation. (accessed: 20.10.2023).

[2] International Commerical Aviation Organization. *Trends in Emissions that affect Climate Change*. URL: https://www.icao.int/environmental-protection/pages/climatechange_trends.aspx#:~:text=Fuel%20Scenario%201%20value%20for,for%20the%20same%20time%20period.. (accessed: 15.10.2023).

[3] D. Lee et al. "Aviation and Global Climate Change in the 21st Century". In: *Atmospheric Environment* 43 (22 2009).

[4] L. Vertonghen and S. Castro. "Modelling of Fibre Steered Plates with Coupled Thickness Variation from Overlapping Continuous Tows". In: *Composite Structures* 268 (2021), p. 113933.

[5] Y. Xu et al. "Concurrent Optimization of Topological Configuration and Continuous Fiber Path for Composite Structures — A Unified Level Set Approach". In: *Computer Methods in Applied Mechanics and Engineering* 399 (2022), p. 115350.

[6] T. Brooks and J. Martins. "On Manufacturing Constraints for Tow-Steered Composite Design Optimization, Composite Structures". In: *Composite Structures* 204 (2018), pp. 548–559.

[7] N. Prasad and R. Wanhill. *Aerospace Materials and Material Technologies*. Springer, 2017.

[8] A. Marouene, P. Legay, and R. Boukhili. "Experimental and Numerical Investigation on the Open-Hole Compressive Strength of AFP Composites Containing Gaps and Overlaps". In: *Journal of Composite Materials* 51 (2017), pp. 3631–3646.

[9] T. Brooks, J. Martins, and G. Kennedy. "High-Fidelity Aerostructural Optimization of Tow-Steered Composite Wings". In: *Journal of Fluids and Structures* 88 (2019), pp. 122–147.

[10] B. Sobhani Aragh et al. "Manufacturable Insight into Modelling and Design Considerations in Fibre-Steered Composite Laminates: State of the Art and Perspective". In: *Computer Methods in Applied Mechanics and Engineering* 379 (2021), p. 113752.

[11] G. Lozano et al. "A Review on Design for Manufacture of Variable Stiffness Composite Laminates". In: *J Engineering Manufacture* 230 (6 2016), pp. 981–992.

[12] SCAD Office. *Unilateral Tension of a Plate with a Small Circular Hole (Kirsch Problem)*. URL: `https://scadsoft.com/tests_scad/en/index/test/40`. (accessed: 20.10.2023).

[13] M. Hyer and R. Charette. "Use of curvilinear fiber format in composite structure design". In: *AIAAJ* 29.6 (1991).

[14] M. Hyer and H. Lee. "The Use of Curvilinear Fiber Format to Improve Buckling Resistance of Composite Plates with Central Circular Holes". In: *Composite Structures* 18 (3 1991), pp. 239–261.

[15] S. Nagendra, S Kodiyalam, and J. Davis. "Use of Curvilinear Fiber Format in Composite Structure Design". In: *36th Structures, Structural Dynamics and Materials Conference* (1995).

[16] K. Wu et al. "Structural Performance of Advanced Composite Tow-Steered Shells With Cutouts". In: *AIAA/ASMe/ASCE/AHS/SC Structures* 55 (2014).

[17] M. Hyer and R. Charette. "Use of Curvilinear Fiber Format in Composite Structure Design". In: *AIAA* 30 (1989).

[18] P. Crothers et al. "Tailored Fibre Placement to Minimise Stress Concentrations". In: *Compos. Part A: Appl. Sci. Manuf.* 28 (8 1997), pp. 19–25.

[19] D. Peeters, S. Hesse, and M. Abdalla. "Stacking Sequence Optimisation of Variable Stiffness Laminates with Manufacturing Constraints". In: *Compos. Struct.* 129 (2015 2015), pp. 596–604.

[20] D. Jegley, B. Tatting, and Z. Gürdal. "Optimization of Elastically Tailored Tow-Placed Plates with Holes". In: *Am. Inst. Aeronaut. Astronaut.* (2003), p. 1420.

[21] A. Khani et al. "Design of Variable Stiffness Panels for Maximum Strength Using Lamination Parameters". In: *Composites Part B: Engineering* 42 (3 2011), pp. 546–552.

[22] Z. Gürdal and R. Olmedo. "In-Plane Response of Laminates with Spacially Varying Fiber Orientations: Variable Stiffness Concept". In: *AIAA Journal* 31 (4 1993).

[23] Dawn Jegley, Brian Tatting, and Zafer Gurdal. "Optimization of Elastically Tailored Tow-Placed Plates with Holes". In: (Feb. 2003).

[24] A. Khani et al. "Design, Manufacturing and Testing of a Fibre Steered Panel with a Large Cut-Out". In: *Composite Structures* 180 (2017), pp. 821–830.

[25] R. Matsuzaki et al. "Optimization of Curvilinear Fiber Orientation of Composite Plates and its Experimental Validation". In: *Compos. Struct.* 255 (2021).

[26] T. Brooks, J. Martins, and G. Kennedy. "Aerostructural Tradeoffs for Two-steered Composite Wings". In: *Atmospheric Environment* 57 (2020), pp. 787–799.

[27] T. Dubois. *Hexcel Prepares for More Composites in Commercial Aircraft.* URL: https://www.ainonline.com/aviation-news/aerospace/2015-09-22/hexcel-prepares-more-composites-commercial-aircraft. (accessed: 15.10.2023).

[28] M. Christian et al. "Free-Edge Effects in Composite Laminates—A Review of Recent Developments 2005–2020". In: *Applied Mechanics Reviews* 74.1 (Apr. 2022), p. 010801.

[29] C. Kassapoglou. *Design and Analysis of Composite Structures with Applications to Aerospace Structures.* John Wiley Sons, 2010.

[30] Z. Hasan. *Tooling for Composite Aerospace Structures, Manufacturing and Applications.* Elsevier, 2020.

[31] F. Campbell. *Manufacturing Processes for Advanced Composites.* Elsevier, 2004.

[32] R. Jones. *Mechanics of Composite Materials.* Taylor & Francis, 1999.

[33] Z. Gürdal, R. Haftka, and P. Hajela. *Design and Optimization of Laminated Composite Materials.* John Wiley Sons, 1999.

[34] "Review of Methodologies for Composite Material Modelling Incorporating Failure". In: *Composite Structures* 86.1 (2008). Fourteenth International Conference on Composite Structures, pp. 194–210.

[35] Angelos Filippatos, Albert Langkamp, and Maik Gude. "Influence of Gradual Damage on the Structural Dynamic Behaviour of Composite Rotors: Simulation Assessment". In: *Materials* 11 (2018).

[36] M. Goelke. *Introduction to Practical Aspects of Composites with Altair OptiStruct.* Altair, 2021.

[37] J. Huang and R. Haftka. "Optimization of Fiber Orientations Near a Hole for Increased Load-Carrying Capacity of Composite Laminates". In: *Struct. Multidisc. Optim.* 30 (2005), pp. 335–341.

[38] L. Parnas, S. Oral, and Ü. Ceyhan. "Optimum Design of Composite Structures with Curved Fiber Courses". In: *Composites Science and Technology* 63 (7 2003), pp. 1071–1082.

[39] B. Tatting, Z. Gürdal, and D. Jegley. "Design and Manufacture of Elastically Tailored Tow Placed Plates". In: (Sept. 2002).

[40] X. Ouyang, X. Yu, and Y. Wang. "Flutter analysis for wing structure using finite element modeling with equivalent stiffness". In: *Journal of Vibroengineering* 16 (2014), pp. 1483–1493.

[41] I. Koutromanos. *Fundamentals of Finite Element Analysis.* Wiley, 2018.

[42] B. Kim, K. Potter, and P. Weaver. "Continuous Tow Shearing for Manufacturing Variable Angle Tow Composites". In: *Composites: Part A* 34 (2012), pp. 1347–1356.

[43] C. Lopes, Z. Gürdal, and P. Camanho. "Variable-Stiffness Composite Panels: Buckling and First-Ply Failure Improvements over Straight-Fibre Laminates". In: *Computers and structures* 87 (2007), pp. 897–907.

[44] K. Button. *Modeling structural strength.* URL: https://aerospaceamerica.aiaa.org/departments/modeling-structural-strength/. (accessed: 20.10.2023).

[45] ViTech Composites. *Vitow.* URL: https://www.vitechcomposites.com/en/vitow-2/. (accessed: 20.10.2023).

[46] D. Gates. *At Boeing's 777X wing factory, robots get big jobs.* URL: https://www.seattletimes.com/business/boeing-aerospace/at-boeings-777x-wing-factory-robots-get-big-jobs/. (accessed: 20.10.2023).

[47] R. Wehbe et al. "Geometrical Modeling of Tow Wrinkles in Automated Fiber Placement". In: *Composite Structures* 246 (2020).

[48] G. Lozano, A. Tiwari, and C. Turner. "A Design Algorithm to Model Fibre Paths for Manufacturing of Structurally Optimised Composite Laminates". In: *Composite Structures* 204 (2018), pp. 882–895.

[49] B. Tatting and Z. Gürdal. "Design and Manufacture of Elastically Tailored Tow Placed Plates". In: *National Aeronautics and Space Administration, Langley Research Center* (2002).

[50] V. Mishra, D.M. Peeters, and M.M. Abdalla. "Stiffness and Buckling Analysis of Variable Stiffness Laminates Including the Effect of Automated Fibre Placement Defects". In: *Compos. Struct.* 226 (2019).

[51] M. Rouse et al. "Utilization of the Building-Block Approach in Structural Mechanics Research". In: *46th AIAA/ASME/ASCE/AHS/ASC Structures, Structural Dynamics, and Materials Conference* (2005).

[52] "Guidelines for Property Testing of Composites". In: *Department of Defense Handbook— Composite Materials Handbook—Polymer Matrix Composites Guidelines for Char- acterization of Structural Materials MIL-HDBK-17-1F* (2002).

[53] *Composite Materials Handbook - Volume 1. Polymer Matrix Composites Guidelines for Characterization of Structural Materials.* Department of Defense Handbook, 2002.

[54] C. Friedland. "A Methodology for Evaluating the Performance of Tow-Steered Composite Technology over a Range of Planform Configurations". In: *PhD dissertation, Georgia Institute of Technology* (2021).

[55] E. Werthen and S. Dähne. "Design Rules Consideration within Optimization of Composite Structures Using Lamination Parameters". In: *Masters Thesis, University of Applied Sciences in Landshut and Ingolstadt* (2016).

[56] J. Bailie, R. Ley, and A. Pasricha. "A Summary and Review of Composite Laminate Design Guidelines". In: *NASA Contract NAS1-19347 Final Report* (1997).

[57] A. Amini et al. "Spatial Uncertainty Sampling for End-to-End Control". In: *Neural Information Processing Systems (NIPS) Workshop on Bayesian Deep Learning* (2018).

[58] P. Christensen and A. Klarbring. *An Introduction to Structural Optimization.* Springer Science, 2009.

[59] A. Antoniou and W. Lu. *Practical Optimization - Algorithms and Engineering Applications*. Springer, 2007.

[60] K. Marmaras. "Optimal Design of Composite Structures Under Manufacturing Constraints". In: *Technical University of Denmark (PhD Thesis)* (2014).

[61] T. Brooks. "Design Optimization of Flexible Aircraft Wings Using Tow-steered Composites (Ph.D. thesis)". In: *University of Michigan, Ann Arbor, MI. Brooks* (2018).

[62] M. Goelke. *Practical Aspects of Structural Optimization with Altair OptiStruct*. Altair.

[63] G. Huang, W. Hu, and G. Li. "An Efficient Reanalysis Assisted Optimization for Variable-Stiffness Composite Design by Using Path Functions". In: *ScienceDirect* 153 (2016), pp. 409–420.

[64] H. Tanaka et al. "Multi-Objective Optimization of Weight and Strength of Laminated Composites Using Gap-less and Overlap-less Variable Thickness Fiber Placement". In: *Compos. Struct.* 276 (2021).

[65] C. Brampton and H. Kim. "Optimization of Tow Steered Fibre Orientation Using the Level Set Method". In: (2013).

[66] H. Ghiasi, D. Pasini, and L. Lessard. "Optimum Stacking Sequence Design of Composite Materials Part I: Constant Stiffness Design". In: *Compos. Struct.* 90 (1 2009), pp. 1–11.

[67] Y. Xu et al. "Robust Topology Optimization for Multiple Fiber-Reinforced Plastic (FRP) Composites under Loading Uncertainties". In: *Struct. Multidiscip. Optim.* 59 (3 2019), pp. 695–711.

[68] D. Jantos, K. Hackl, and P. Junker. "Topology Optimization with Anisotropic Materials, Including a Filter to Smooth Fiber Pathways". In: *Struct. Multidiscip. Optim.* 61 (5 2020), pp. 2135–2154.

[69] D. Peeters, D. van Baalen, and M. Abdallah. "Combining Topology and Lamination Parameter Optimisation". In: *Struct. Multidiscip. Optim.* 52 (1 2015), pp. 105–120.

[70] D. Hozi´c et al. "A New Method for Simultaneous material and Topology Optimization of Composite Laminate Structures Using Hyperbolic Function Parametrization". In: *Compos. Struct.* 276 (2021).

[71] S. Sørensen and R. Sørensen. "DMTO – A Method for Discrete Material and Thickness Optimization of Laminated Composite Structures". In: *Struct. Multidiscip. Optim.* 50 (1 2014), pp. 25–47.

[72] J. Grenestedt and P. Gudmundson. "Layup Optimization of Composite Material Structures". In: *Opt. Des. Adv. Mater.* (1993), pp. 311–336.

[73] P. Hao et al. "Design of Manufacturable Fiber Path for Variable-Stiffness Panels Based on Lamination Parameters". In: *Compos. Struct.* 219 (2019), pp. 158–169.

[74] T. Shafighfard, E. Demir, and M. Yildiz. "Design of Fiber-Reinforced Variable-Stiffness Composites for Different Open-Hole Geometries with Fiber Continuity and Curvature Constraints". In: *Composite Structures* 226 (2019), p. 111280.

[75] S. Setoodeh et al. "Generating Curvilinear Fiber Paths from Lamination Parameters Distribution". In: *47th AIAA/ASME/ASCE/AHS/ASC Structures, Structural Dynamics, and Materials Conference 14th AIAA/ASME/AHS Adaptive Structures Conference 7th* (2006), p. 1875.

[76] Z. Wu, G. Raju, and P. Weaver. "Framework for the Buckling Optimization of Variable-Angle Tow Composite Plates". In: *AIAAJ* 53 (12 2015), p. 2015.

[77] M. Montemurro and A. Catapano. "On the Effective Integration of Manufacturability Constraints within the Multi-Scale Methodology for Designing Variable Angle-Tow Laminates". In: *Composite Structures* 161 (2017), pp. 145–159.

[78] J. Van Campen, C. Kassapoglou, and Z. Gürdal. "Generating realistic laminate fiber angle distributions for optimal variable stiffness laminates". In: *Compos Part B: Eng* 43 (2012), pp. 354–360.

[79] Y. Tian, T. Shi, and Q. Xia. "A Parametric Level Set Method for the Optimization of Composite Structures with Curvilinear Fibers". In: *Computer Methods in Applied Mechanics and Engineering* 388 (2022), p. 114236.

[80] A. Blom, M. Abdalla, and Z. Gürdal. "Optimization of course locations in fiber-placed panels for general fiber angle distributions". In: *Composites Science and Technology* 70.4 (2010), pp. 564–570.

[81] B. Kim, P. Weaver, and K. Potter. "Computer Aided Modelling of Variable Angle Tow Composites Manufactured by Continuous Tow Shearing". In: *Composite Structures* 129 (2015), pp. 256–267.

[82] S. Castro, M. Donadon, and T Guimarães. "ES-PIM Applied to Buckling of Variable Angle Tow Laminates". In: *Compos Struct* 209 (2018), pp. 67–78.

[83] A. Blom, P. Stickler, and Z. gürdal. "Optimization of a Composite Cylinder under Bending by Tailoring Stiffness Properties in Circumferential Direction". In: *Compos Part B Eng* 41 (2010), pp. 157–165.

[84] M. Tooren et al. "Design of Variable Stiffness Composite Plates with Cut-Outs Using a Dual Mesh Approach". In: *16th AIAA/ISSMO Multidisciplinary Analysis and Optimization Conference* (2015).

[85] H. Ghiasi et al. "Optimum Stacking Sequence Design of Composite Materials Part II: Variable Stiffness Design". In: *Composite Structures* 93 (1 2010), pp. 1–13.

[86] G. Keeffe. "Optimization of Composite Structures - A Shape and Topology Sensitivity analysis". In: *Ecole Polytechnique (PhD Thesis)* (2014).

[87] M. Zhou, R. Fleury, and W. Dias. "Composite Design Optimization - from Concept to Ply-Book Details". In: *8th World Congress on Structural and Multidisciplinary Optimization* (2009).

[88] M. Zhou, R. Fleury, and M. Kemp. "Optimization of Composite – Recent Advances and Application". In: *13th AIAA/ISSMO Multidisciplinary Analysis Optimization Conference* (2010).

[89] M. Zhou, R. Fleury, and T. Willmet. "Multiple Phase Optimization of Composite Structures". In: *9th US National Congress of Computational Mechanics* ().

[90] T. Cipriano. "Production and Composite Optimization Studies of a Composite Laminate Structure Applied in the Industrial Sector". In: (2016).

[91] J. Martín. "Composite Optimization Techniques for Aircraft Components Structural Sizing". In: *8TH EUROPEAN CONFERENCE FOR AERONAUTICS AND SPACE SCIENCES (EUCASS)* ().

[92] E. Chong and S. Zak. *An Introduction to Optimization*. Wiley, 2013.

[93] S. Date, Y. Abe, and T. Okabe. "Effects of fiber properties on aerodynamic performance and structural sizing of composite aircraft wings". In: *Aerospace Science and Technology* 124 (2022), p. 107565.

[94] *XC130 Autoclave Cure Component Prepreg - Technical Datasheet*. XPREG. Nov. 2022.

[95] D. Adams and D. Adams. "Tabbing Guide for Composite Specimens". In: *Federal Aviation Administration* (2002).

[96] P. Feraboli. "Composite Materials Strength Determination Within the Current Certification Methodology for Aircraft Structures". In: *Journal of Aircraft - J AIRCRAFT* 46 (2009), pp. 1365–1374.

[97] I. Daniel and O. Ishai. *Engineering Mechanics of Composite Materials*. Oxford University Press, 1994.

[98] I. Daniel, R. Rowlands, and J. Whiteside. "Effects of material and stacking sequence on behavior of composite plates with holes". In: *Experimental Mechanics* 14 (1974), pp. 1–9.

[99] "Design guidelines for ply drop-off in laminated composite structures". In: *Composites Part B: Engineering* 32.2 (2001), pp. 153–164.

[100] A. Viglietti et al. "Analysis of variable angle tow composites structures using variable kinematic models". In: *Composites Part B: Engineering* 171 (2019), pp. 272–283.

[101] G. Zhao et al. "Numerical Analysis of Interlaminar Stresses of Angle-ply AS4/PEEK Laminate with a Central Hole". In: *Journal of Thermoplastic Composite Materials - J THERMOPLAST COMPOS MATER* 22 (July 2009), pp. 383–406.

[102] R. Chaudhuri. "A new three-dimensional shell theory in general (non-lines-of-curvature) coordinates for analysis of curved panels weakened by through/part-through holes". In: *Composite Structures* 89.2 (2009), pp. 321–332.

[103] "Progressive Failure Analysis of Tow-Placed, Variable-Stiffness Composite Panels". In: *International Journal of Solids and Structures* 44.25 (2007), pp. 8493–8516.

[104] E. Demir, P. Yousefi-Louyeh, and M. Yildiz. “Design of Variable Stiffness Composite Structures Using Lamination Parameters with Fiber Steering Constraint”. In: *Composites B* 165 (2019), pp. 733–746.

[105] J. Dillinger. “Static Aeroelastic Optimization of Composite Wings with Variable Stiffness Laminates”. In: *DLR Deutsches Zentrum fur Luft- und Raumfahrt e.V. - Forschungsberichte* (May 2015), pp. 1–249.

APPENDICES

APPENDIX

A

CODE FOR NUMERICAL SOLUTION

The following are excerpts from the code written for the design study, comprising the most important components of the numerical solution.

FEA solution

The input data for the FE solver is stored within the following variables.

```
import numpy as np
NODES = []               # The coordinates of each node in the model
ELEMS = []               # The connectivity between nodes
constrained_DOFs = []    # Which DOFs are constrained
load_list = []           # Which DOFs have a load and what magnitude
theta_list = []          # The orientation of each ply
thickness_list = []      # The thickness of each ply
```

Calculates the elastic material matrix $\mathbf{Q}'$ (Eq. 4.3).

```
def local_Q_matrix(E1, E2, G, v12):
    v21 = v12 * E2 / E1
    return np.array([[E1, v21 * E1, 0],
                     [v12 * E2, E2, 0],
                     [0, 0, (1 - v12 * v21) * G]]) / (1 - v12 * v21)
```

Transforms $\mathbf{Q}'$ by angle β (Eq. 4.9).

```
def transform_stiffness_matrix(Q, beta):
    cos_b, sin_b = np.cos(beta), np.sin(beta)
    T = np.array([[cos_b ** 2, sin_b ** 2, sin_b * cos_b],
                  [sin_b ** 2, cos_b ** 2, -sin_b * cos_b],
                  [-2 * sin_b * cos_b, 2 * sin_b * cos_b,
                   cos_b ** 2 - sin_b ** 2]])
    return T.T @ Q @ T
```

Calculates laminate stiffness $\mathbf{D}$ as the sum of ply contributions (Eq. 4.12)

```
def laminate_stiffness_matrix(stiffness_matrix_list, ply_thickness_list):
    D = np.sum(np.array(stiffness_matrix_list)[:, np.newaxis, np.newaxis] *
               np.array(ply_thickness_list)[:, np.newaxis, np.newaxis],
```

```
            axis=0) / laminate_thickness
    laminate_thickness = np.sum(ply_thickness_list)
    return D , laminate_thickness
```

Performs cyclic permutation (0, 1, 2).

```
def cp3(x, i):
    return (x + i) % 3
```

Uses $\mathbf{D}$ to calculate the element stiffness matrix $\mathbf{K}^{(e)}$ (Eq. 4.15 and 4.16).

```
def element_stiffness_matrix(node_list, D, laminate_thickness):
    K = np.zeros((6, 6))
    x, y = zip(*node_list)
    A = 0.5 * (x[0] * (y[1] - y[2]) + x[1]
               * (y[2] - y[0]) + x[2] * (y[0] - y[1]))

    for i in range(3):
        for j in range(3):
            bi = y[cp3(i, 1)] - y[cp3(i, 2)]
            bj = y[cp3(j, 1)] - y[cp3(j, 2)]
            ci = x[cp3(i, 2)] - x[cp3(i, 1)]
            cj = x[cp3(j, 2)] - x[cp3(j, 1)]

            Bi = np.array([[bi, 0, ci], [0, ci, bi]])
            Bj = np.array([[bj, 0], [0, cj], [cj, bj]])

            Kij = np.matmul(np.matmul(Bi, D), Bj) \
                  * laminate_thickness / (4 * A)

            K[i * 2:i * 2 + 2, j * 2:j * 2 + 2] = Kij

    return K
```

Assembles element matrices into the global stiffness matrix $\mathbf{K}$ and applies Dirichlet boundary conditions.

```
def global_stiffness_matrix(theta_list, thickness_list):
    DOFs = len(NODES) * 2
    K = np.zeros((DOFs, DOFs))

    #Iterate through all elements
    for element_index, element in enumerate(ELEMS):
        # Calculate laminate stiffness D
        ply_stiffness_list = [transform_stiffness_matrix(
            local_Q_matrix(130, 10, 5, 0.3), theta) for
            theta in theta_list[:, element_index]]
        ply_thickness_list = thickness_list[:, element_index]
        laminate_stiffness = laminate_stiffness_matrix(ply_stiffness_list,
                                                       ply_thickness_list)

        # Create local stiffness matrix K for element
        element_stiffness = element_stiffness_matrix(
            elementNodeCoords(element), laminate_stiffness[0],
            laminate_stiffness[1])
```

```
        # Map the element stiffness to the global DOFs
        for i, j in zip(*np.meshgrid(element, element)):
            K[np.ix_(range(i * 2, (i + 1) * 2), range(j * 2, (j + 1) * 2))] += \
                element_stiffness

    # Apply Dirichlet boundary conditions
    K = np.delete(K, constrained_DOFs, axis=0)
    K = np.delete(K, constrained_DOFs, axis=1)

    return K
```

Creates the load vector $\mathbf{q}$.

```
def global_load_vector(load_list, constrained_DOFs):
    q = np.zeros(len(NODES) * 2)

    # Map loads to global DOFs
    for load_data in load_list:
        element_index, *load_values = load_data
        for DOF, load_value in enumerate(load_values):
            q[element_index * 2 + DOF] = load_value

    # Remove constrained DOFs
    q = np.delete(q, constrained_DOFs)
    return q
```

Solves the global matrix equilibrium equation (Eq. 4.19) for the nodal displacement vector $\mathbf{a}$ and compliance f_c (Eq. 4.1)

```
def solve_FEA(theta_list, thickness_list, load_list, constrained_DOFs):
    # Create stiffness matrix K and load vector q
    K = global_stiffness_matrix(theta_list, thickness_list)
    q = global_load_vector(load_list, constrained_DOFs)

    # Solve linear system
    matrix_solution = np.linalg.solve(K, q)
    f_c = matrix_solution @ K @ matrix_solution / 2

    # Put the removed DOFs back into solution
    a = np.zeros(len(NODES) * 2)
    DOF_list = np.arange(len(NODES) * 2)
    DOF_list = np.delete(DOF_list, constrained_DOFs)
    for i in range(len(DOFlist)):
        a[DOF_list] = matrix_solution[i]

    return a, f_c
```

Failure analysis

Calculates the strain tensor ε for each element using the displacement vector $\mathbf{a}$ (Eq. 4.21).

```
def element_strain_list(a):
    strain_list = []
```

```
    for element_nodes in ELEMS:
        # Get node coordinates and displacement vectors
        xy = np.array([NODES[node_index][:2]
                       for node_index in element_nodes])
        a_e = np.array([a[node_index * 2:node_index * 2 + 2]
                        for node_index in element_nodes]).flatten()
        A = 0.5 * np.linalg.det(np.concatenate(
            (xy, np.ones((3, 1))), axis=1))

        # Compute element strain
        B = np.array([
            [(xy[cp3(i, 1), 1] - xy[cp3(i, 2), 1]) / (2 * A), 0, 0],
            [0, (xy[cp3(i, 2), 0] - xy[cp3(i, 1), 0]) /
             (2 * A), (xy[cp3(i, 2), 1] - xy[cp3(i, 1), 1]) / (2 * A)]
        ])
        strain_list.append(B @ a_e)
    return strain_list
```

Uses the strain tensor to evaluate the Tsai-Hill failure index at each ply within the element (Eq. 4.20, 4.22 and 4.23).

```
def Tsai_Hill(strain_list, thetaList, stress_multiplier):
    failure_index_list = []
    X_11 = 645
    X_22 = 60
    S_12 = 69

    for element_index in range(len(ELEMS)):
        ply_failure = []
        strain_vector = strain_list[element_index]
        for ply_index in range(4):
            # Determine stress state in ply
            theta = thetaList[ply_index][element_index]
            ply_stiffness = DmatrixTransform(Dmatrix(
                matE1, matE2, matG, matv), theta)
            stress_vector = np.matmul(ply_stiffness, strain_vector)

            # Applies stress multiplier, used to vary the load
            sigma_xx = stress_vector[0] * stress_multiplier
            sigma_yy = stress_vector[1] * stress_multiplier
            tau_xy = stress_vector[2] * stress_multiplier

            # Transform stress to principal material axes
            sigma_11 = ((sigma_xx + sigma_yy) / 2 + np.cos(2 * theta)
                        * (sigma_xx - sigma_yy) / 2 + tau_xy * np.sin(2 * theta))
            sigma_22 = ((sigma_xx + sigma_yy) / 2 - np.cos(2 * theta)
                        * (sigma_xx - sigma_yy) / 2 - tau_xy * np.sin(2 * theta))
            tau_12 = (-np.sin(2 * theta) * (sigma_xx - sigma_yy)
                      / 2 + tau_xy * np.cos(2 * theta))

            # Calculate failure index
            Tsai_Hill_index = ((sigma_11 / X_11) ** 2 + (sigma_22 / X_22) ** 2
                               + (tau_12 / S_12) ** 2 - (sigma_11 * sigma_22)
                               / X_11 ** 2)
            ply_failure.append(Tsai_Hill_index)
        failure_index_list.append(ply_failure)
    return failure_index_list
```

Optimization algorithm

Calculates ply orientations at each element based on B-spline control point values (Eq. 4.26).

```
from geomdl import BSpline
control_point_values = []
control_point_coords = []

def B_spline_interpolation(control_point_values):
    control_points = control_point_coords.copy()
    for i in len(control_point_values):
        control_points[i].append(control_point_values)
    knot_vector = [0] * len(control_point_values) + [1]
                    * len(control_point_values)

    # Define B-spline surface from control points
    B_spline = Bspline.Curve()
    B_spline.degree = 3
    B_spline.ctrlpts = control_points
    B_spline.knotvector = knot_vector

    # Evaluate function values at each element centroid
    theta_list = []
    for ply_index in range(plyCount):
        orientation_offset = ply_index * np.pi / 4
        element_theta = [
            B_spline(element_centers[element_index])[0]
                                + orientation_offset
            for element_index in range(element_count)
        ]
        theta_list.append(element_theta)
    return theta_list
```

Computes the sensitivity for ply orientation variables using finite-differencing (Eq. 4.35).

```
def theta_0_sensitivity(control_point_values, thickness_list):
    theta_list = B_spline_interpolation(control_point_values)
    _, initial_compliance = solve_FEM(theta_list, thickness_list)
    delta = 0.001
    sensitivity_vector = []

    # Compute sensitivities through finite differencing
    for control_point_index in range(len(control_point_values)):
        modified_control_points = control_point_values.copu()
        modified_control_points[control_point_index] += delta
        modified_theta = B_spline_interpolation(modified_control_points)

        _, modified_compliance = solveFEM(modified_theta, thickness_list)
        compliance_sensitivity = (modified_compliance
                    - initial_compliance)/delta
        sensitivity_vector.append(compliance_sensitivity)
    return sensitivity_vector
```

Computes the sensitivity for ply thickness using the adjoint method (Eq. 4.40).

```
def ply_thickness_sensitivity(control_point_values, thickness_list):
    theta_list = B_spline_interpolation(control_point_values)
    sensitivity_vector = []
    DOFs = len(NODES) * 2
    delta = 0.001

    # Compute sensitivities using adjoint method
    a, _ = solve_FEA(theta_list, thickness_list)
    for element_index, element in enumerate(ELEMS):
        element_K_matrices = []
        element_sensitivities = []
        for ply_index in range(5)
            K = np.zeros((DOFs, DOFs))
            ply_stiffness_list = [transform_stiffness_matrix(
                local_Q_matrix(130, 10, 5, 0.3), theta) for
                theta in theta_list[:, element_index]]
            ply_thickness_list = thickness_list[:, element_index]
            if not ply_thickness_list == 0:
                ply_thickness_list[ply_index-1] += delta
            laminate_stiffness = laminate_stiffness_matrix(ply_stiffness_list,
                                                           ply_thickness_list)
            element_stiffness = element_stiffness_matrix(
                elementNodeCoords(element), laminate_stiffness[0],
                laminate_stiffness[1])
            for i, j in zip(*np.meshgrid(element, element)):
                K[np.ix_(range(i * 2, (i + 1) * 2), range(j * 2, (j + 1) * 2))] += \
                element_stiffness
            element_K_matrices.append(K)
        for i in range(4)
            K_sensitivity = (element_K_matrices[i+1] - element_K_matrices[0])/delta
            element_sensitivities.append(a.T @ K_sensitivity @ a)
        sensitivity_vector.append(element_sensitivities)
    return sensitivity_vector
```

Solves the optimization problem using steepest descent (Eq. 4.30), while enforcing constraints using the projection method (Eq. 4.33). At each iteration, γ is determined numerically using the bisection method.

```
def steepest_descent(initial_thickness, initial_control_points):
    objective_tolerance = 0.005
    mass_constraint = 11.90
    constraint_vector = mass_sensitivity(element_areas)
    convergence = 1

    # Define initial state
    thickness_list = initial_thickness
    control_point_values = initial_control_points
    theta_list = B_spline_interpolation(control_point_values)
    _, initial_compliance = solve_FEA(theta_list, thickness_list)
    previous_iteration_compliance = initial_compliance

    # Repeat until converged
    while convergence > objective_tolerance:

        # Perform sensitivity analysis
        thickness_sensitivity = ply_thickness_sensitivity(control_point_values,
                                                          thickness_list)
```

```
    theta_sensitivity = theta_0_sensitivity(control_point_values, thickness_list)

    # Apply constraints & determine vector length
    x = 2
    for bisection_iteration in range(20):
        compliance_list = []
        for i in range(2):
            iterated_thickness = (np.array(thickness_list)
                        + (x + i*10**(-6)) * 2000 * thickness_sensitivity)
            for j in range(5):
                mass_difference = total_mass(iterated_thickness) \
                                    - mass_constraint
                iterated_thickness -= mass_difference * constraint_vector
                iterated_thickness = np.clip(iterated_thickness,
                                        0.001, 1000)
            iterated_control_points = (control_point_valuesalues
                            - 2 * (x + i*10**(-6)) * theta_sensitivity)
            iterated_theta = B_spline_interpolation(iterated_control_points)
            a, iterated_compliance = solve_FEA(iterated_theta,
                                                iterated_thickness)
            compliance_list.append(iterated_compliance)
        vector_length_sensitivity = compliance_list[1] - compliance_list[0]
        x_change = 1/(2 ** bisection_iteration)
        x -= x_change if vector_length_sensitivity > 0 else -x_change

    # Reevaluate objective function
    control_point_values = iterated_control_points
    thickness_list = iterated_thickness
    theta_list = B_spline_interpolation(control_point_values)
    a, new_compliance = solveFEA(theta_list, thickness_list)

    # Compute convergence
    convergence = (abs(new_compliance-previous_iteration_compliance)
                   / new_compliance)
    previous_iteration_compliance = new_compliance

return control_point_values, thickness_list
```

APPENDIX

B

STIFFNESS MATRIX OF THE LINEAR TRIANGULAR ELEMENT

Shape Functions

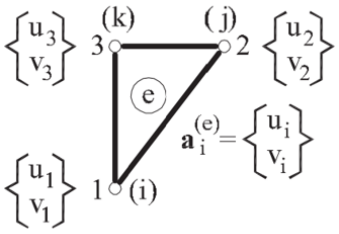

For the triangle element above, the displacements of an arbitrary point within the element are expressed in terms of the nodal displacements u_i and v_i as:

$$u = N_1 u_1 + N_2 u_2 + N_3 u_3 \tag{B.1}$$

$$v = N_1 v_1 + N_2 v_2 + N_3 v_3 \tag{B.2}$$

Where N_i is the shape function of node i. This is written in matrix form as:

$$\mathbf{u} = \begin{bmatrix} u \\ v \end{bmatrix} = \begin{bmatrix} N_1 & 0 & N_2 & 0 & N_3 & 0 \\ 0 & N_1 & 0 & N_2 & 0 & N_3 \end{bmatrix} \begin{bmatrix} u_1 \\ v_1 \\ u_2 \\ v_2 \\ u_3 \\ v_3 \end{bmatrix} \tag{B.3}$$

The linear displacement field defined by the three nodes is written as:

$$u = \alpha_1 + \alpha_2 x + \alpha_3 y \tag{B.4}$$

$$v = \alpha_4 + \alpha_5 x + \alpha_6 y \tag{B.5}$$

Since the interpolation is the same for u and v, it suffices to derive the shape functions for one of the displacements. The horizontal nodal displacements are obtained from Eq. B.4 as:

$$u_1 = \alpha_1 + \alpha_2 x_1 + \alpha_3 y_1 \tag{B.6}$$

$$u_2 = \alpha_1 + \alpha_2 x_2 + \alpha_3 y_2 \tag{B.7}$$

$$u_3 = \alpha_1 + \alpha_2 x_3 + \alpha_3 y_3 \tag{B.8}$$

Solving for α_1, α_2 and α_3 and substituting into Eq. B.4 yields:

$$u = \frac{1}{2A^{(e)}} \left[(a_1 + b_1 x + c_1 y)\, u_1 + (a_2 + b_2 x + c_2 y)\, u_2 + (a_3 + b_3 x + c_3 y) u_3 \right] \tag{B.9}$$

Where $A^{(e)}$ is the element area, and

$$a_i = x_j y_k - x_k y_j \quad , \quad b_i = y_j - y_k \quad , \quad c_i = x_k - x_j \quad ; \quad i, j, k = 1, 2, 3 \tag{B.10}$$

The parameters a_i, b_i and c_i are obtained by cyclic permutation of the indexes i, j, k. From the previous equations, the expression for the shape functions is found as:

$$\boxed{N_i = \frac{1}{2A^{(e)}} (a_i + b_i x + c_i y) \quad , \quad i = 1,\ 2,\ 3} \tag{B.11}$$

Stress and Strain Field Discretization

The three characteristic strains can be written in matrix form as:

$$\boldsymbol{\varepsilon} = \mathbf{B}\mathbf{a}^{(e)} \tag{B.12}$$

Where $\mathbf{B}$ is the element strain matrix:

$$\mathbf{B} = \begin{bmatrix} \mathbf{B}_1 & \mathbf{B}_2 & \mathbf{B}_3 \end{bmatrix} \tag{B.13}$$

And $\mathbf{B}_i$ is the strain matrix of node i:

$$\mathbf{B}_i = \begin{bmatrix} \frac{\partial N_i}{\partial x} & 0 \\ 0 & \frac{\partial N_i}{\partial y} \\ \frac{\partial N_i}{\partial y} & \frac{\partial N_i}{\partial x} \end{bmatrix} \tag{B.14}$$

Particularizing for the 3-noded element (using previously derived shape functions) this is written as:

$$\mathbf{B}_i = \frac{1}{2A^{(e)}} \begin{bmatrix} b_i & 0 \\ 0 & c_i \\ c_i & b_i \end{bmatrix} \tag{B.15}$$

The discretized expression for the stress field within the element is obtained using Hooke's law, substituting in Eq. B.12:

$$\boldsymbol{\sigma} = \mathbf{D}\boldsymbol{\varepsilon} = \mathbf{D}\mathbf{B}\mathbf{a}^{(e)} \tag{B.16}$$

Discretized Equilibrium Equations

As usual in FEM, the equilibrium of the forces acting on the element is enforced point-wise at the nodes only. The nodal point loads F_x and F_y are introduced, which balance the external forces and the internal forces due to the element deformation along the horizontal and vertical directions, respectively. These "equilibrating nodal forces" are obtained by applying the principle of virtual work to an individual element as:

$$\iint\limits_{A^{(e)}} \delta\boldsymbol{\varepsilon}^T \boldsymbol{\sigma} t dA = \sum_{i=1}^{3} \delta u_i F_{x_i} + \sum_{i=1}^{3} \delta v_i F_{y_i} \tag{B.17}$$

Where δu_i and δv_i are the nodal virtual displacements. These are grouped into the vectors:

$$\left[\delta\mathbf{a}^{(e)}\right]^T = \begin{bmatrix}\delta\mathbf{a}_1^T & \delta\mathbf{a}_2^T & \delta\mathbf{a}_3^T\end{bmatrix}^{(e)} = \begin{bmatrix}\delta u_1 & \delta v_1 & \delta u_2 & \delta v_2 & \delta u_3 & \delta v_3\end{bmatrix} \tag{B.18}$$

$$\left[\mathbf{q}^{(e)}\right]^T = \begin{bmatrix}\mathbf{q}_1^T & \mathbf{q}_2^T & \mathbf{q}_3^T\end{bmatrix}^{(e)} = \begin{bmatrix}F_{x_1} & F_{y_1} & F_{x_2} & F_{y_2} & F_{x_3} & F_{y_3}\end{bmatrix} \tag{B.19}$$

The virtual work performed by these forces is thereby obtained as:

$$\iint\limits_{A^{(e)}} \delta\boldsymbol{\varepsilon}^T \boldsymbol{\sigma} t dA = \left[\delta\mathbf{a}^{(e)}\right]^T \mathbf{q}^{(e)} \tag{B.20}$$

Next, the virtual displacements are interpolated in terms of the nodal values. By substituting the relations

$$\delta\mathbf{u} = \mathbf{N}\delta\mathbf{a}^{(e)} \qquad \delta\varepsilon = \mathbf{B}\delta\mathbf{a}^{(e)} \tag{B.21}$$

The following expression is obtained:

$$\iint\limits_{A^{(e)}} \mathbf{B}^T \boldsymbol{\sigma} t dA = \mathbf{q}^{(e)} \tag{B.22}$$

This represents the equilibrating nodal forces $\mathbf{q}^{(e)}$ in terms of the nodal forces due to element deformation. Substituting the formula for the stresses in terms of nodal displacements (Eq. B.16) gives:

$$\iint\limits_{A^{(e)}} \mathbf{B}^T \mathbf{D}\mathbf{B}\mathbf{a}^{(e)} t dA = \mathbf{q}^{(e)} \tag{B.23}$$

Which is finally written as:

$$\mathbf{K}^{(e)}\mathbf{a}^{(e)} = \mathbf{q}^{(e)} \tag{B.24}$$

Where the element stiffness matrix $\mathbf{K}^{(e)}$ equals:

$$\boxed{\mathbf{K}^{(e)} = \iint\limits_{A^{(e)}} \mathbf{B}^T \mathbf{D}\ \mathbf{B} t dA} \tag{B.25}$$

APPENDIX

C

TEST SPECIMEN MANUFACTURING

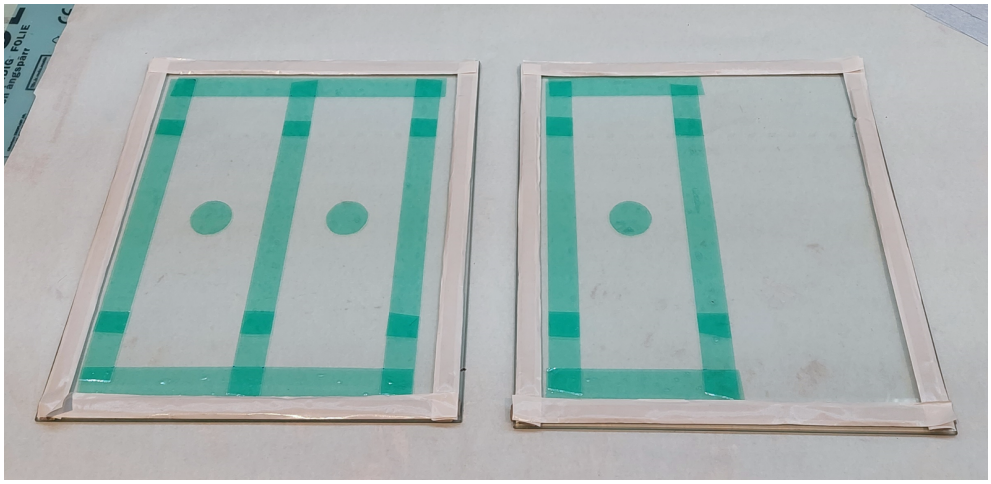

Figure C.1: Glass tooling surfaces marked with flash tape, providing a reference for fiber placement.

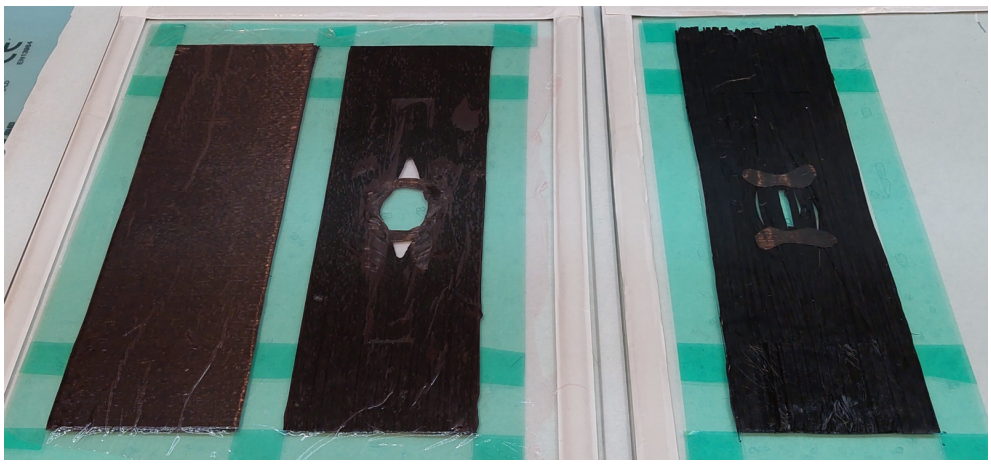

Figure C.2: Completed fiber lay-up of the test specimens.

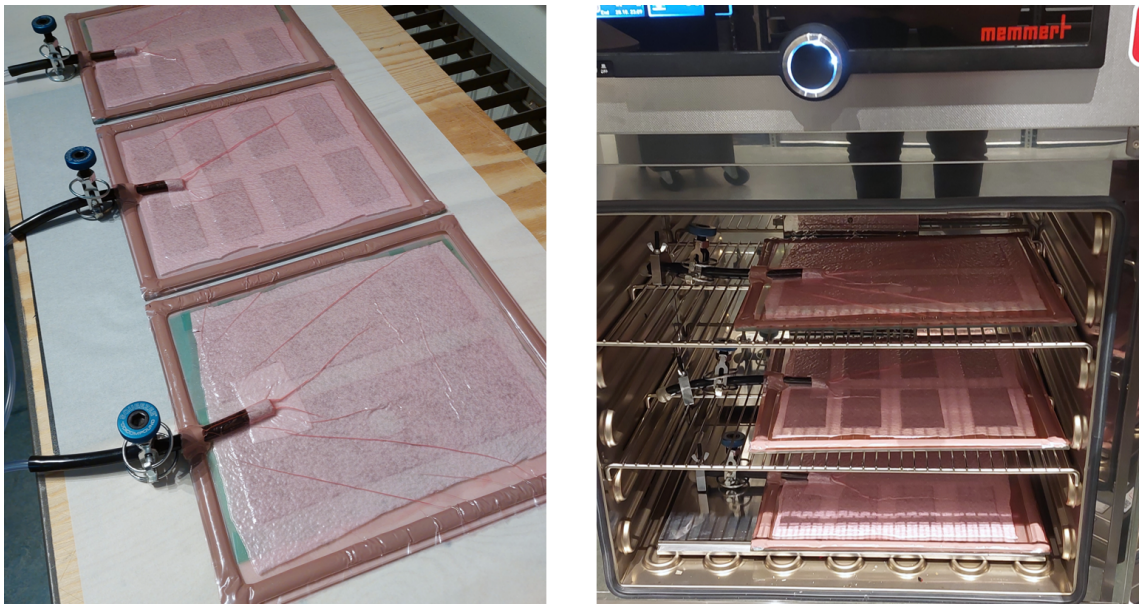

Figure C.3: Application of vacuum and placement in oven for curing.

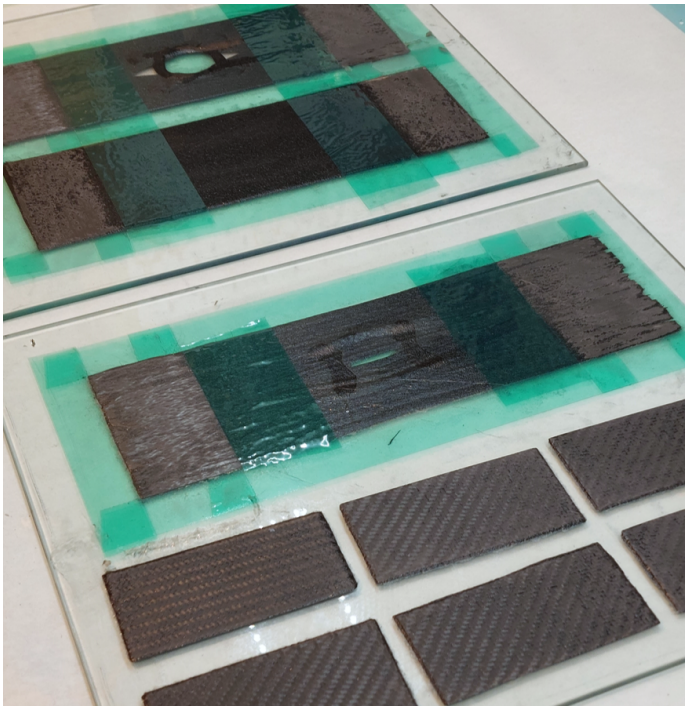

Figure C.4: Components after de-moulding, abraded to ensure good bond quality.

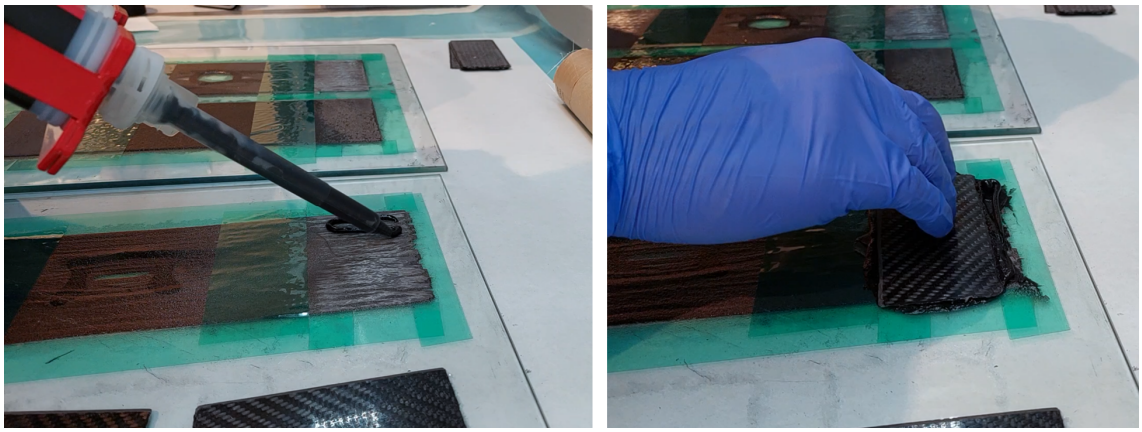

Figure C.5: Application of adhesive and joining of specimen tabs.

Figure C.6: Trimming the bonded structure.

APPENDIX

D

DISPLACEMENT DATA

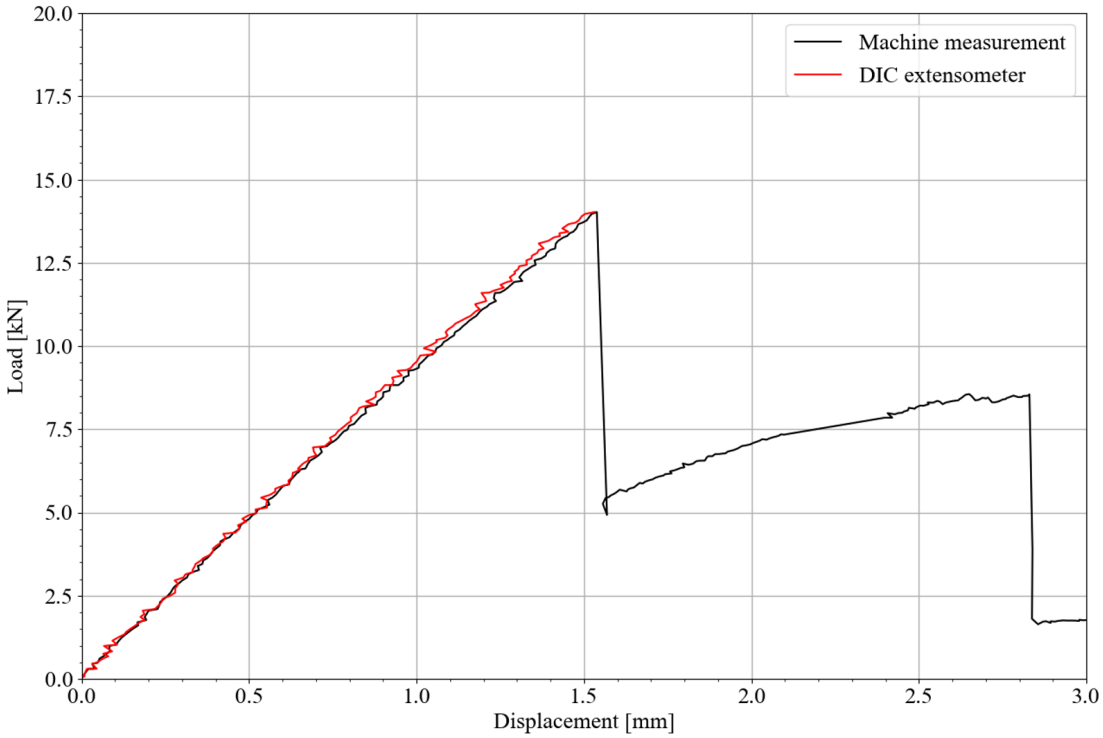

Figure D.1: QI test specimen.

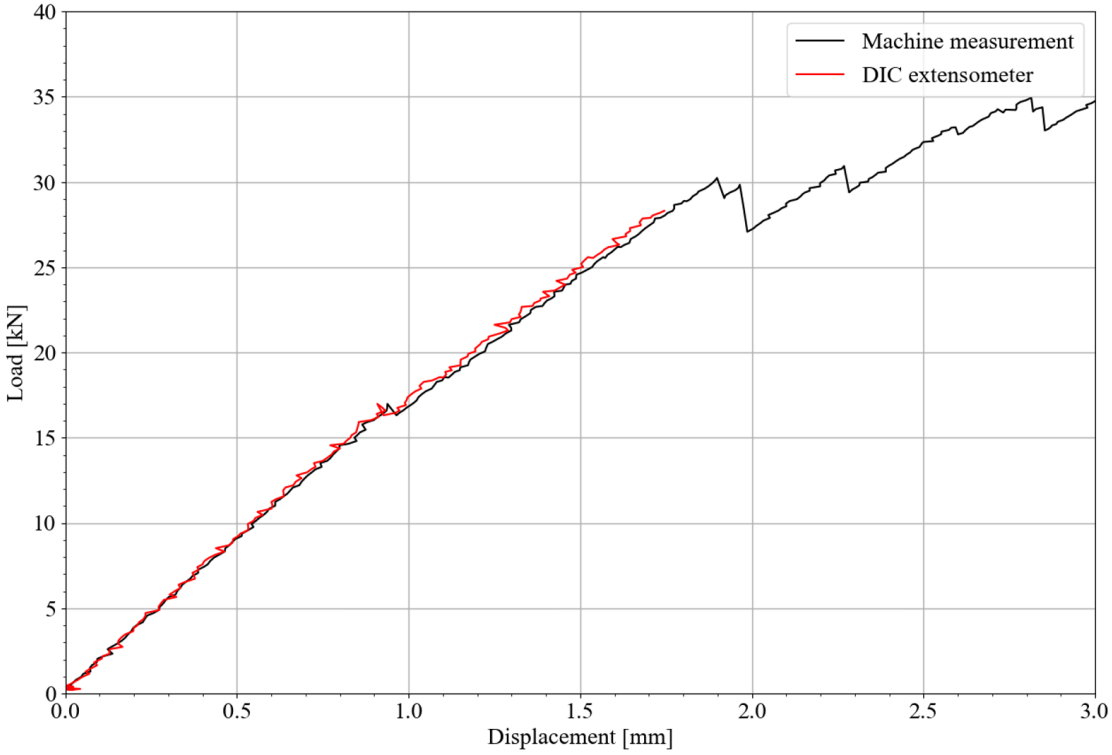

Figure D.2: VS test specimen.

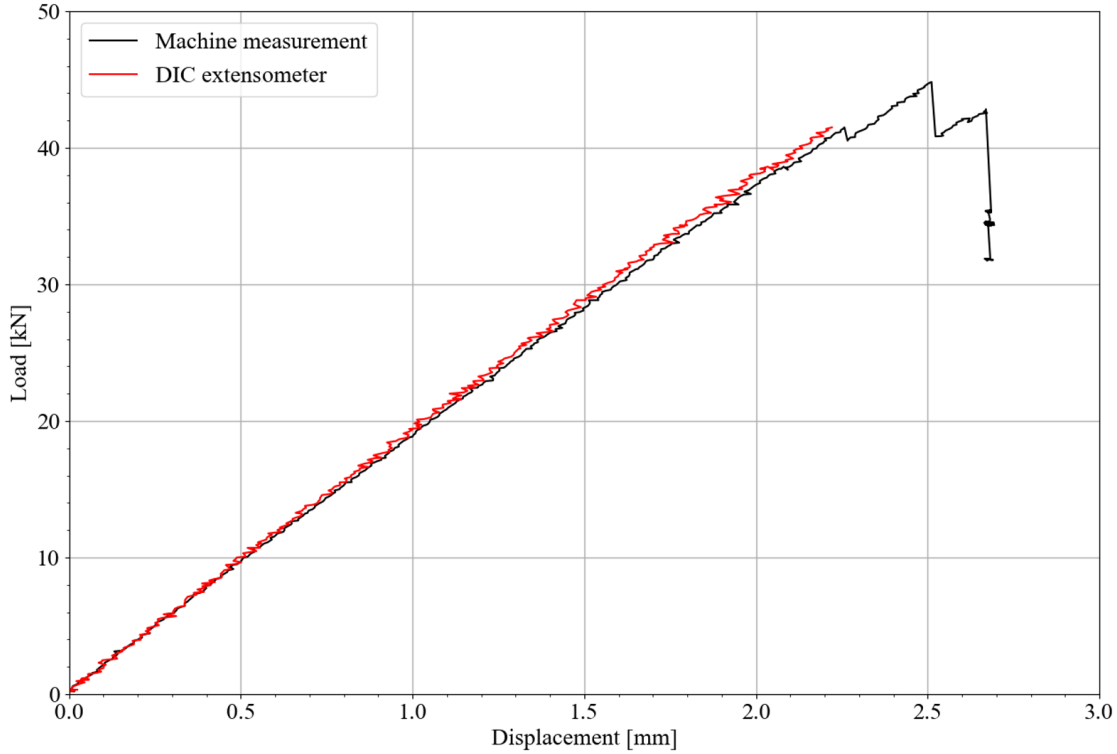

Figure D.3: VAT test specimen.

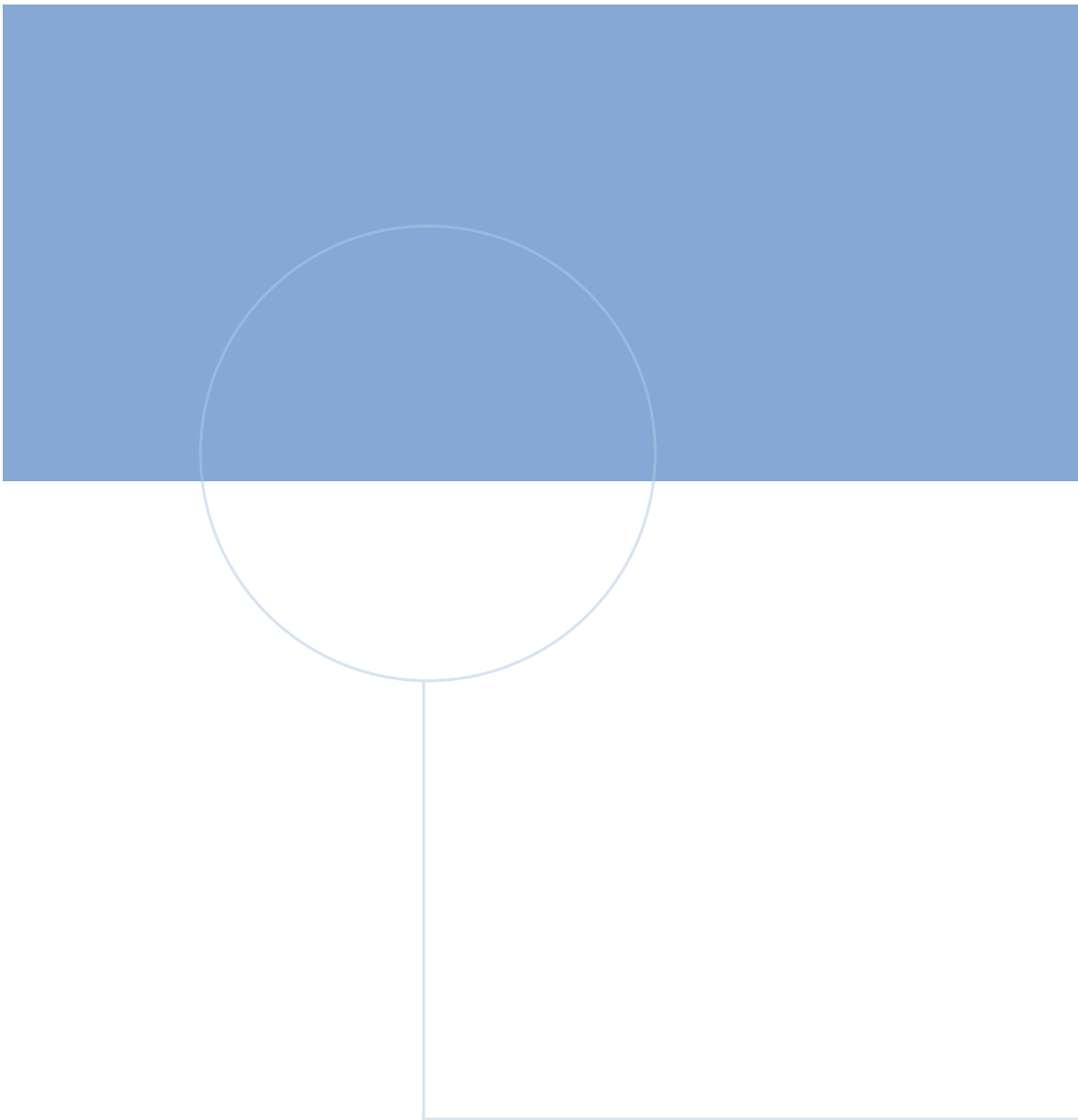

NTNU
Norwegian University of
Science and Technology